3-D seismic imaging of the plumbing system of the Kora Volcano, Taranaki Basin, New Zealand: The influence of syn-rift structure on shallow igneous intrusion architecture

C.K. Morley

Petroleum Geophysics MSc. Program, Department of Geological Sciences, Chiang Mai University, Chiang Mai, Thailand

ABSTRACT

Descriptions of the interactions between volcano plumbing systems and early-stage rift systems dominated by large half grabens and tilted fault blocks are scarce and lack detail. 3-D seismic reflection data across the Early Miocene-age subduction-related Kora Volcano plumbing system in the Taranaki Basin, offshore New Zealand, provides an opportunity to investigate in detail how this system has interacted with a Late Cretaceous–Early Paleogene rift system. The shallow (<8-km-depth) architecture of intrusions are dominated by stacked saucer-shaped, and transgressive sills, and laccolith complexes distributed in an oval shape around the volcano. The thickest sill complexes occur in the thickest (fault-controlled) syn-rift depocenters. There is also local elongation of sill complexes in a N-S direction following structural trends. Numerous sills locally follow segments of large normal faults, or terminate at the faults. Laterally extensive sill complexes tend to lie close to the base of the syn-rift/top of pre-rift contact for distances up to 15 km away from the Kora Volcano. A general pattern is that the lowest-level sills are the most laterally extensive, and the shallower sills lie closer to the volcano. Shallow sills form a complex of concentric sills that dip away from the volcano center (ring sills). Sills are interpreted to have been fed by intrusions following faults that intersect a broad upper crustal magma chamber with a calculated area of ~345 km². Strong preference for sill/laccolith stacking in the thick syn-rift section appears to have had four effects. (1) In the upper 6 km there probably was not a simple single pipe feeding the volcano, instead the volcano is inferred to have been fed by a network of sills linked by short dikes and pipes. (2) The extensive intrusions resulted in folding/doming of the Paleogene section in several places, but most significantly under the central part of the volcano. (3) Much of the magma was stored in intrusive complexes within the syn-rift section and the underlying magma chamber (volume ~124 km³), not extruded (volume ~40 km³). (4) Edifice construction and broad doming related to subsurface intrusions may have caused the crest of the volcano to become subaerial. The consequent absence of phreatomagmatic eruptions and the extensive accumulation of magma in relatively thin sill complexes (that could cool relatively rapidly and solidify) avoided a destructive end to the volcanic edifice.

1. INTRODUCTION

The plumbing systems of volcanoes are known to be highly varied and complex for highly varied reasons, which for upper crustal plumbing systems includes the influence of stratigraphic configuration and faults, and both local and regional changes in the stress field (see reviews in Tibaldi, 2015; Tibaldi and Bonali, 2017). Most studies conducted on the relationships between structure, and volcanism in rifts, are focused on the advanced stages of extension in continental rifts (e.g., Ethiopian Rift, central Kenya Rift, e.g., Mohr, 1987; Rubin and Pollard, 1988; Morley, 1994; Delaney et al., 1998; Dugda et al., 2005; Ebinger et al., 2010; Beutel et al., 2010; Muirhead et al., 2016; Dumont et al., 2017 and references therein), or oceanic rifts such as Afar (Ethiopia) and Iceland where magmatic processes dominate (e.g., Hjartardóttir et al., 2012; Mazzarini et al., 2013; Belachew et al., 2013; Medynski et al., 2016 and references therein).

Volcanoes commonly occur in rifts, yet only a few studies have investigated the ways in which early-stage syn-rift basin architecture and faults influence volcanic plumbing architecture. Ellis and King (1991) describe how flank volcanism in rifts could be explained by a flexing plate model where dilational strain is developed in the footwall at the base of the crust, which caused cracking and activation of preexisting melt. Interaction of faults with four different trends (including intersections with preexisting E-W trends) in the main Ethiopian Rift has been shown to set up tail cracks, extensional relays, and fault intersections that have localized the eruption sites of monogenetic Plio-Quaternary volcanoes (Acocella et al., 2003; Korme et al., 2003). While shallow intrusion arrays within a few hundred meters of the paleosurface, show sills were preferentially extended into the hangingwall blocks of normal faults that hosted dikes, particularly at interfaces between relatively strong Paleozoic carbonates and weak Cenozoic tuffs (Valentine and Krogh, 2006). Although outcrop studies and geodetic studies provide some indications as to how volcanic plumbing systems develop within a syn-rift system (see review in Tibaldi, 2015) they do not provide the full 3-D perspective of these systems.

This study is focused on the Miocene Kora Volcano, which is a volcanic edifice, well-imaged by seismic reflection data that is buried in the Taranaki
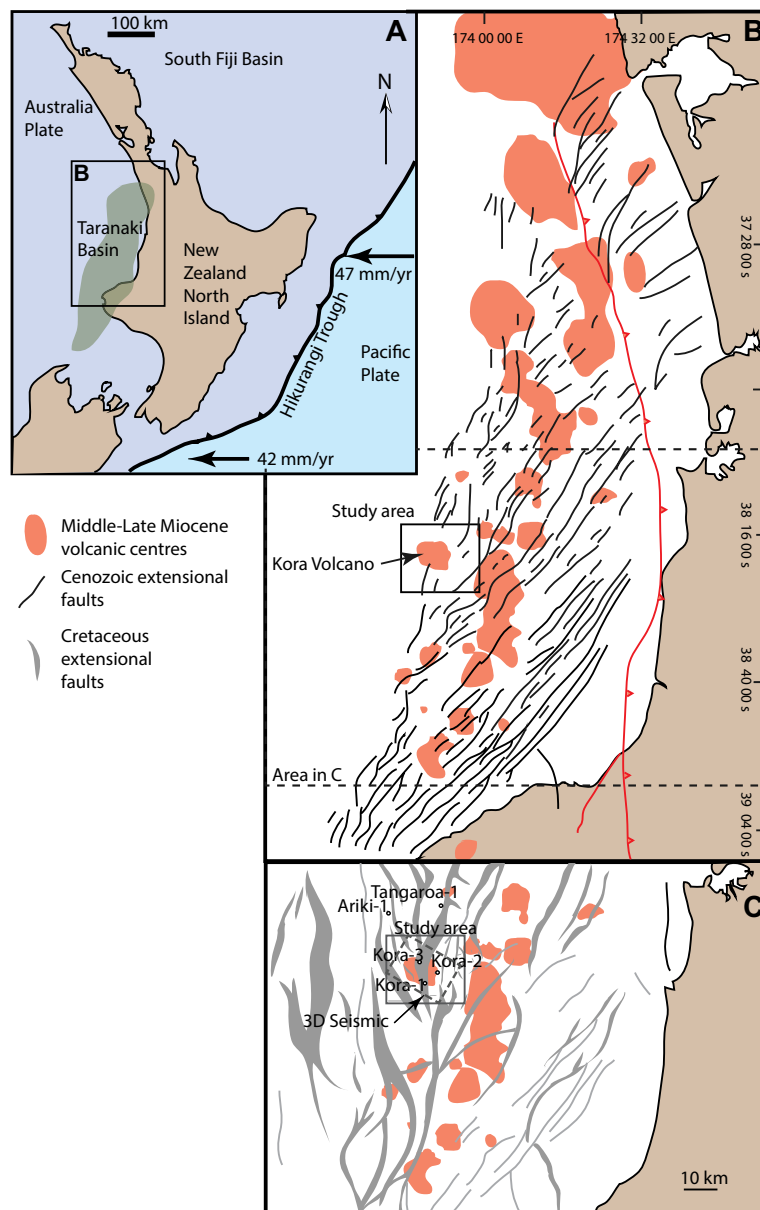
Figure 1. Location map for the Kora area in the Taranaki Basin, offshore New Zealand. (A) Regional map. (B) Major Cenozoic faults and distribution of Miocene volcanic centers in the Taranaki Basin. (C) Major Late Cretaceous syn-rift fault trends in the central Taranaki Basin (see B for location). Modified and redrawn from Kroeger et al. (2013).

Basin, offshore New Zealand (Fig. 1). Two recent studies have focused on the geomorphology of the Kora Volcano and the impact of the edifice on successive deposits (Infante-Paez and Marfurt, 2017; Bischoff et al., 2017). These studies have also described the presence of sills and forced folds at depth, but have not investigated in detail the relationship between the volcano plumbing system and the Late Cretaceous–Paleocene syn-rift section. This investigation focuses on how the Kora Volcano plumbing system interacted with the syn-rift section, which tends to be dominated by half graben formation, large-displacement normal faults, and thick sequences of syn-tectonic sedimentation (Figs. 2 and 3). The Kora 3-D seismic data provides very good images of the volcanic edifice, and away from the Kora Volcano the Cretaceous syn-rift structure is well-imaged (Figs. 2 and 3). However, passing toward the volcano imaging of the syn-rift structure decreases due to degradation of the seismic data related to the high density of igneous intrusions, energy absorbtion by the volcanic edifice, and the presence of steeply dipping beds (Figs. 3 and 4). Consequently, in about a 5-km-diameter region beneath the Kora Volcano there is little coherent seismic reflection data. Hence information on intrusion geometry, and syn-rift structure, must be projected from the well-imaged parts of the seismic data into that area in order to develop a model for the volcano plumbing system. Natural examples, and those from analogue and numerical models, are used to support the interpretation.

In other regions of New Zealand, shallow and deep seated controls on Quaternary volcanism in the Auckland volcanic field have been identified (Cassidy and Locke, 2010). The location of volcanism coincides with regional magnetic and gravity anomalies that mark a deep, major crustal suture. In the upper crust NNW-SSE–trending serpentinized shear zones are thought to influence the trend and extent of the Auckland volcanic field (Cassidy and Locke, 2010). While there may well be a deep influence on volcanism in the Taranaki Basin too, this is beyond the scope of this study which focuses on the shallower influence of syn-rift structures on intrusion architecture in the upper 6 km of continental crust.

■ 2. GEOLOGICAL BACKGROUND TO THE TARANAKI BASIN

The Taranaki Basin lies mostly offshore western New Zealand (Fig. 1). The geological history given below is summarized from Petroleum Report Series (1984) and King and Thrasher (1996). Rifting was initiated in Albian times. There is a major unconformity that separates the early rifts from later Late Cretaceous–Paleocene rifts (Suggate et al., 1978). In the Taranaki Basin it is mostly the later rift fill that has been penetrated by wells. The Late Cretaceous section is referred to as the Pakawau Group (Fig. 5). This group is typically non-marine in outcrop but in offshore wells, deposits tend to be more marine and paralic, often with well-developed coal measures. In the Ariki-1 Well (Fig. 1C) the sequence comprises finely interbedded siltstones and sandstones overlying a more shale prone interval, all of which is interpreted as having been deposited in a coastal environment (Petroleum Report Series, 1984).
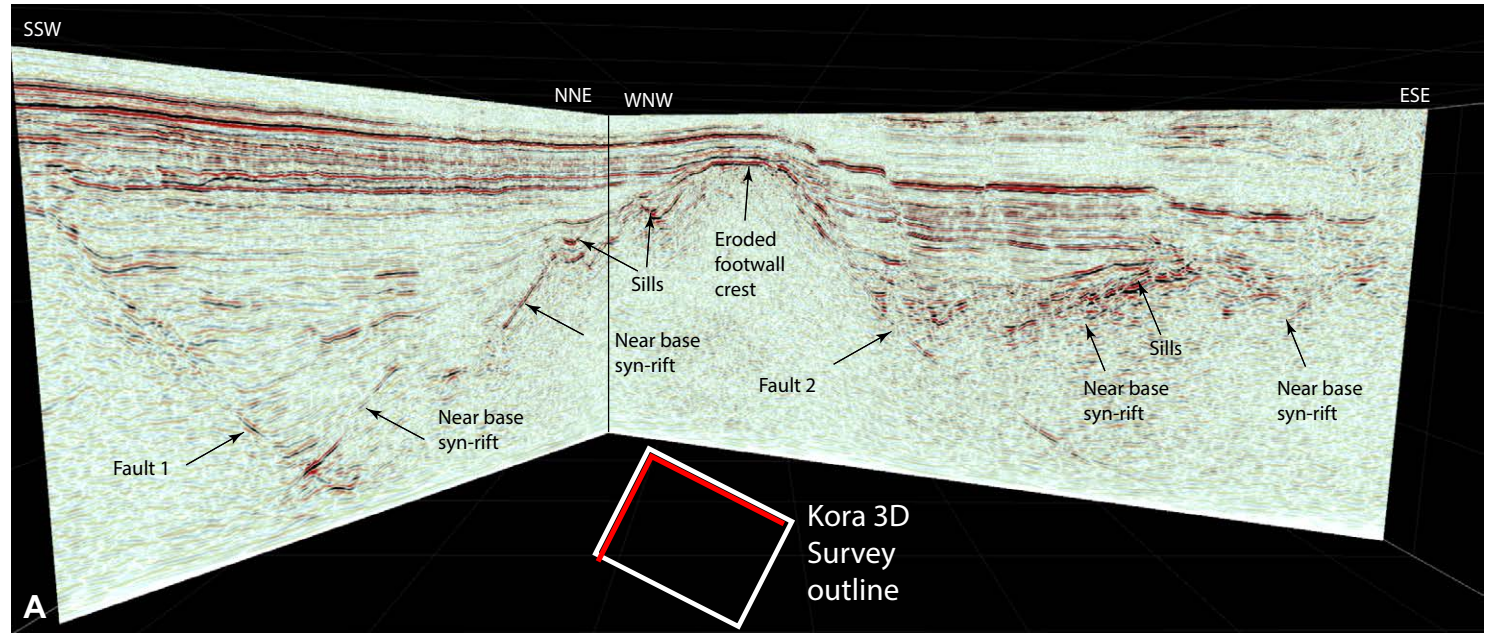
Figure 2. Perspective views of 3-D seismic lines illustrating the well-imaged regions of the syn-rift section of the Kora area in the Taranaki Basin, offshore New Zealand. (A) Seismic data at the WNW and NNE margins of the survey. (B) Seismic data at the WNW and SSW margins of the survey. NNE-SSW line length is 20 km. WNW-ESE line length is 27 km.
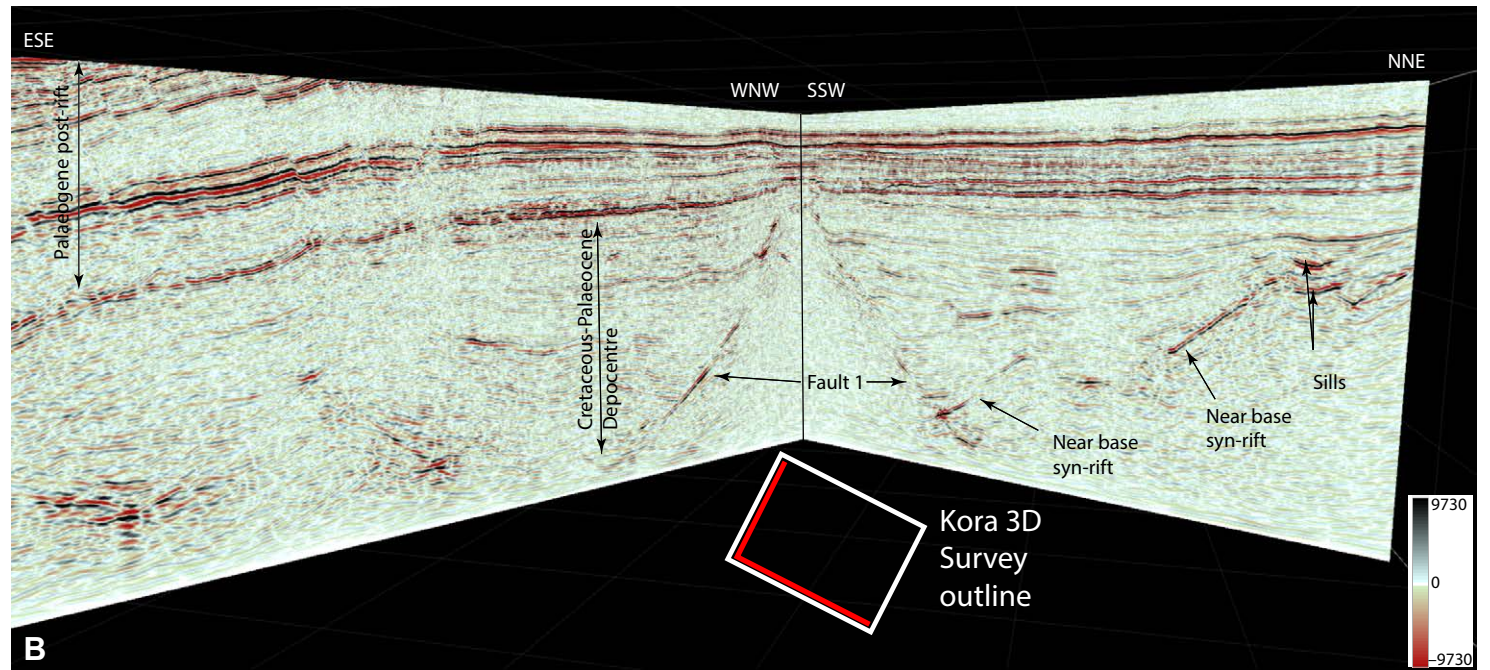
Figure 3. Perspective views of 3-D seismic lines illustrating the well-imaged regions of the syn-rift section of the Kora area in the Taranaki Basin, offshore New Zealand. WNW margin of the survey rapidly passes into data strongly affected by igneous intrusions on WNW-ESE–trending seismic lines (in contrast to Fig. 2). WNW-ESE line length is 27 km. (A) WNW-ESE line south of the main Kora Volcano center. (B) WNW-ESE line north of the main Kora Volcano center.
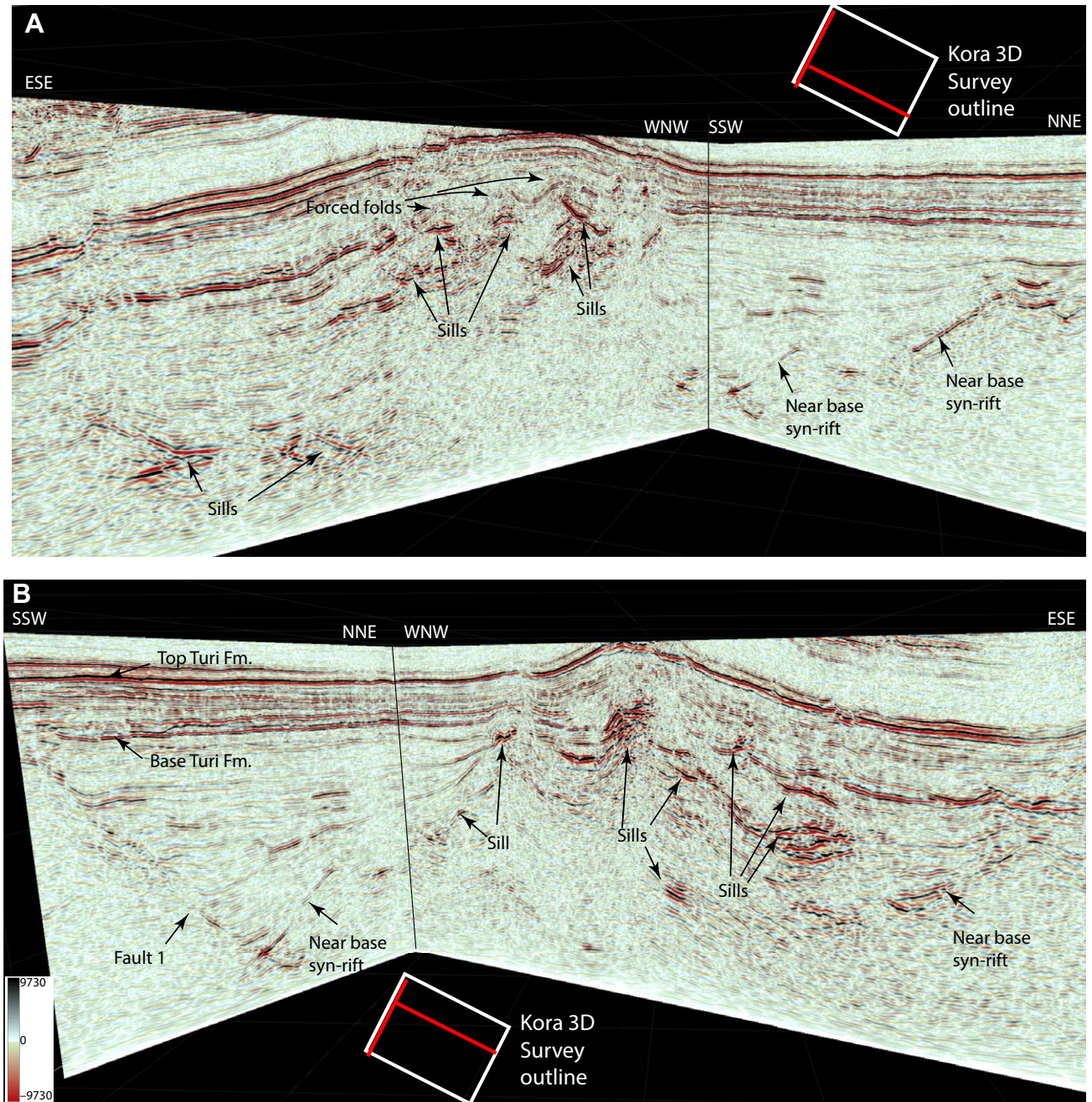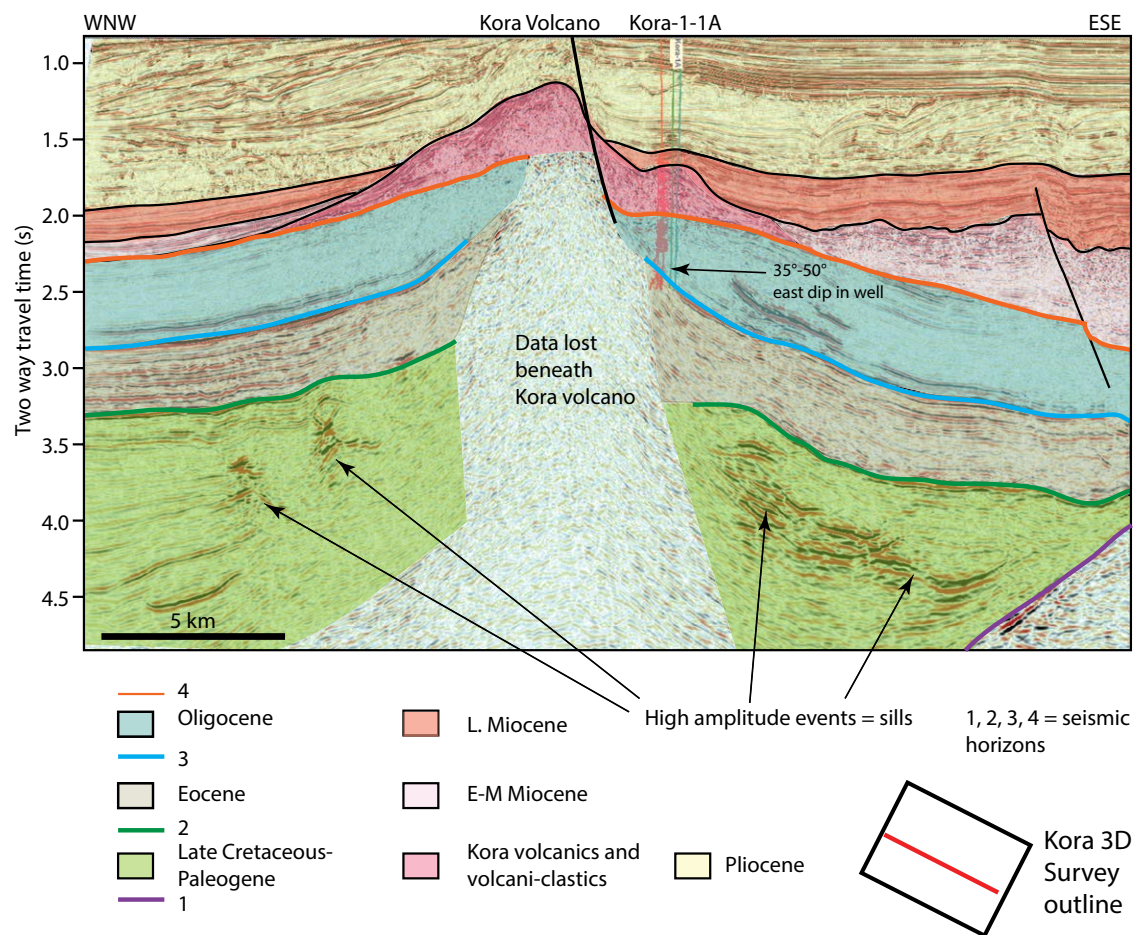
Figure 4. 3-D seismic line, illustrating the main seismic features, seismic horizons, and stratigraphic units discussed in this study of the Kora area in the Taranaki Basin, offshore New Zealand. L.—late; E-M—early to middle.

The rift basins exhibit predominantly NW-SE, N-S, and NE-SW fault trends (Fig. 1), and can contain up to 5 km of section. The NW-SE trends appear to be associated with older rifting (Zealandia rift phase) from ca. 105–83 Ma, and pre-date a Latest Cretaceous–Paleocene rifting phase (80–55 Ma) where newly formed faults trend N-S to NE-SW (Strogen et al., 2017). In the study area the NW-SE trend appears to have been active, or reactivated at the same time as the N-S to NE-SW–trending faults, during the late stage of rifting. During the Paleocene the rift topography became eroded and covered, and Lower Paleocene transgressive sandstones (Fig. 5) are found overlying the Pakawau Group. Deposition passes upwards into hemipelagic and pelagic shales (Turi Formation). Deepwater conditions continued through the Eocene and the maximum transgression occurred in the Lower Oligocene. Pelagic lime-

stones (Ngatoro Group) and carbonate platforms of Oligocene age replaced the clastic-dominated Kapuni Group (Fig. 5). Around the Oligocene–Miocene boundary clastic sedimentation resumed and continued to the present. The Early and Middle Miocene was a period of hemi-pelagic clastic sedimentation (Manganui Formation) that was succeeded by turbidites (Mokai Formation). Intense volcanism, including the Kora Volcano, is a characteristic of the Miocene, which is due to renewed subduction along the NE margin of New Zealand's North Island (Giba et al., 2010, 2013). This was accompanied by transform activity on the Alpine fault and mountain building. Consequently, the deepwater basin became rapidly filled with sediment during the Pliocene-Recent (Giant Foresets) and a large continental shelf was constructed in the basin (Fig. 5).
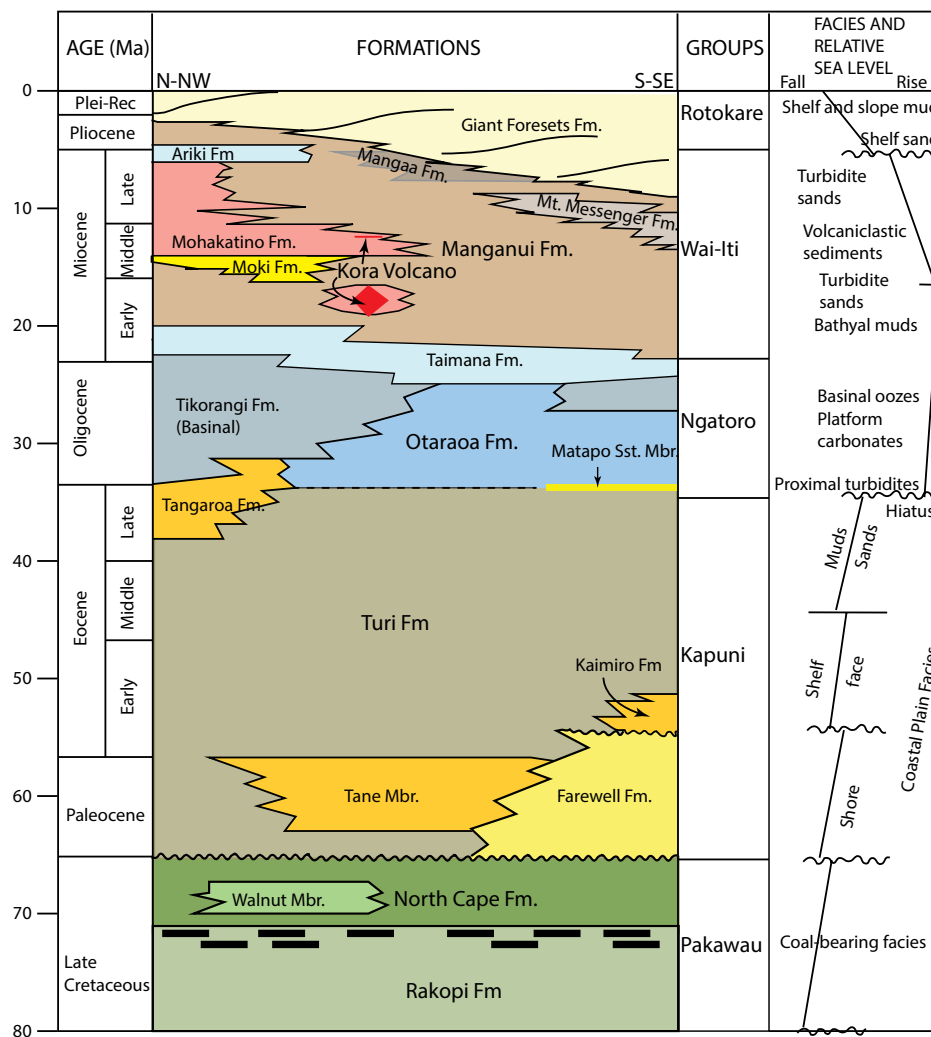
Figure 5. Stratigraphy of the northern and central Taranaki Basin, offshore New Zealand. Based on data in King and Thrasher (1996). Plei-Rec—Pleistocene–Recent; Sst. Mbr.—sandstone member.

The Kora Volcano is part of a NNE-SSW–trending zone of buried Miocene stratovolcanoes in the Northern Graben of the Taranaki Basin (Fig. 1; Bergman et al., 1992; King and Thrasher, 1996; Giba et al., 2010; Seebeck et al., 2014). The volcanic edifices are commonly complex stacks of multiple volcanic events whose internal structure is difficult to unravel (Giba et al., 2010). The Kora Volcano represents a relatively short-lived event associated with a discrete single volcano. Semi-radial normal faults suggest some degree of collapse of the volcano, but they affect the Middle and Late Miocene section overlying the volcano (Bischoff et al., 2017; Infante-Paez and Marfurt, 2017) suggesting either they formed largely after volcanic activity ceased, or they formed during caldera collapse and were reactivated later. Compared with other volcanoes, covered by seismic both within the Taranaki Basin and seen by the author in different basins worldwide, the volcanic edifice and the underlying plumbing system are atypically well-imaged on 3-D seismic reflection data (Bischoff et al., 2017; Infante-Paez and Marfurt, 2017).

Four wells (Kora 1-1A, 2, 3, 4) have been drilled into the Kora Volcano (Infante-Paez and Marfurt, 2017) (Fig. 6). Kora-2 and Kora-3 reached their total depths (TD) in the Miocene volcanics. The other two wells intersected the boundary between the Oligocene (Ngatoro Group) and Eocene section (Turi Formation) (3123 m below rotary kelly bushing (RKB) in Kora-4; 3421 m RKB in Kora-1) and reached TD within the Eocene section (Fig. 4). The wells do not provide information on the Late Cretaceous syn-rift section. However, NNW of the seismic survey, and 24 km from Kora 1-1A, the Ariki-1 Well has penetrated the syn-rift section to pre-rift basement (Fig. 6), and through 2-D data the horizons can be tied into the Kora 3-D survey.

Bischoff et al. (2017) place the age of activity for the Kora Volcano as starting around 17 Ma and continuing until 8 Ma. However, this is based on the syn-magmatic section being entirely related to activity from the Kora Volcano. Yet the tapering wedge of igneous and volcani-clastic sediment that thins away from the volcano only occupies the lower part of the syn-magmatic sequence (Fig. 4). It is onlapped by sediments that are derived from other volcanic centers to the east. The seismic stratal relationships considered here suggest that the Kora Volcano was probably relatively short lived and may have only been active for a few million years at the start of the igneous activity in the basin. Five andesitic samples from Kora 1-1A were K-Ar dated in 1988 using hornblendes from tuff breccias and lapillistone (Petroleum Report Series, 1988). The following dates were obtained: 19.5 ± 4.2 Ma (1909.93 m RKB), 17.5 ± 1.9 Ma (1901 m RKB), 18.2 ± 2.0 (1827.59 m RKB), 17.6 ± 1.9 Ma (1795 m RKB), and 12.1 ± 2.6 Ma (1787 m RKB). The top of the volcanics was encountered at 1781.2 m RKB and the base was at 2581.5 m RKB. From the dates obtained and the depth of samples, it is apparent that the volcanism was short lived and predominantly of Early Miocene age (19.5–17.5 Ma, near the top of ~786 m of volcano-related section), with a short minor burst of activity around 12 Ma (~14 m of section).

The Ariki-1 Well was drilled by Shell in 1983–1984 to a TD of 4822 m (below drill floor) and was the first well in the Taranaki Basin to test the Cretaceous section. Basement in the Ariki-1 Well and the nearby Tangoroa-1 Well is composed of Permian metabasalts and rhyolites (Brook Street Volcanics), that were whole-rock K-Ar radiometrically dated at 128 ± 4 Ma (Petroleum Report Series, 1984). In the report the radiometric age is interpreted to be a recrystallization age related to the Lower Cretaceous Rangitata Orogeny.

■ 3. MODELS FOR VOLCANO PLUMBING SYSTEMS

As reviewed by Tibaldi (2015) the shallow plumbing systems of active volcanoes have been reconstructed by combining available geophysical data with field information derived from outcropping sheets, morphometric analysis of pyroclastic cones, and the orientation and location of eruptive fissures. Active volcanic processes leading to eruptions create a variety of phenomena that can be monitored including: increased earthquake activity, surface uplift due to magma accumulation, heat variations, and gas emission (see review in Tibaldi, 2015). Often in rifts emphasis is placed on: the role played by vertical intrusions (dikes, pipes) in emplacement of magma, the replacement of faulting by mode 1 fractures, or the occurrence of fault swarms above regions of intense dike intrusions (Figs. 7A–7D; e.g., Mohr, 1987; Rubin and Pollard, 1988; Morley 1994; Rubin, 1995; Delaney et al., 1998; Ebinger et al., 2010; Hjartardóttir et al., 2012; Belachew et al., 2013; Tibaldi et al., 2017). Globally there are abundant descriptions of feeder pipes and dikes associated with many intrusions, indicating the importance of vertical feeder systems to volcanoes (e.g., Ryan, 1988; Chiarabba et al., 2004; Tibaldi, 2015; Koulakov et al., 2016). However, there is also recognition of the existence of significant departures from vertically dominated intrusive systems. A variety of styles of eruption, ranging from flood basalts to supervolcanoes (like Toba in present-day Lake Toba, Sumatra, Indonesia) involve storage of magma in thick, extensive networks of sills at different levels within the crust (Fig. 7E; Marsh et al., 1997; Marsh, 2004; Ishizuka et al.,
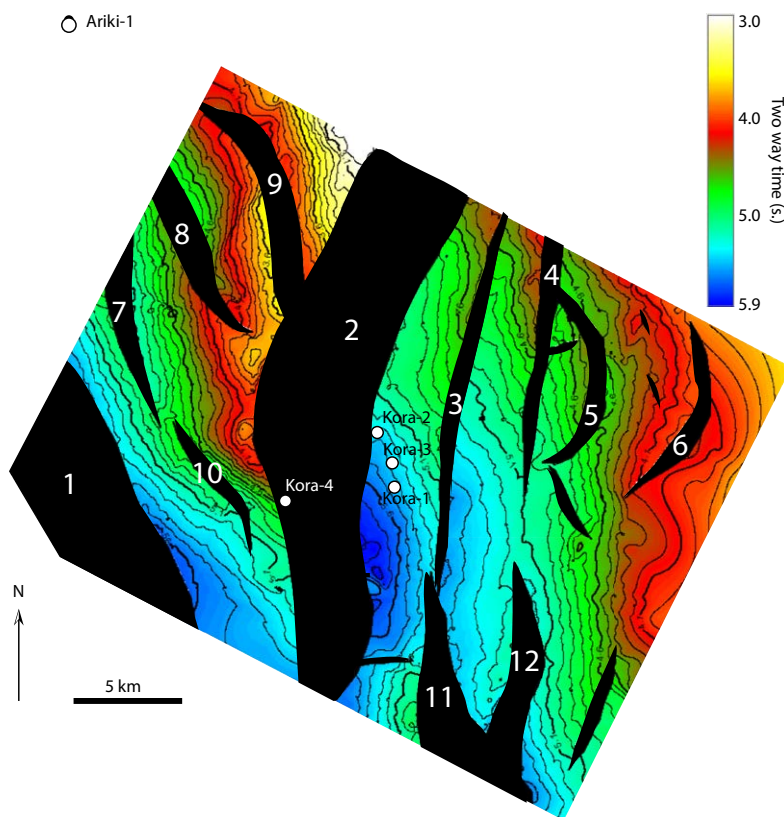

Figure 6. Time-structure map of the base Cretaceous syn-rift section, Kora area in the Taranaki Basin, offshore New Zealand, based on 3-D seismic reflection data, showing location of Kora wells. Fault polygons are in black, reference numbers for the different faults are given in white.
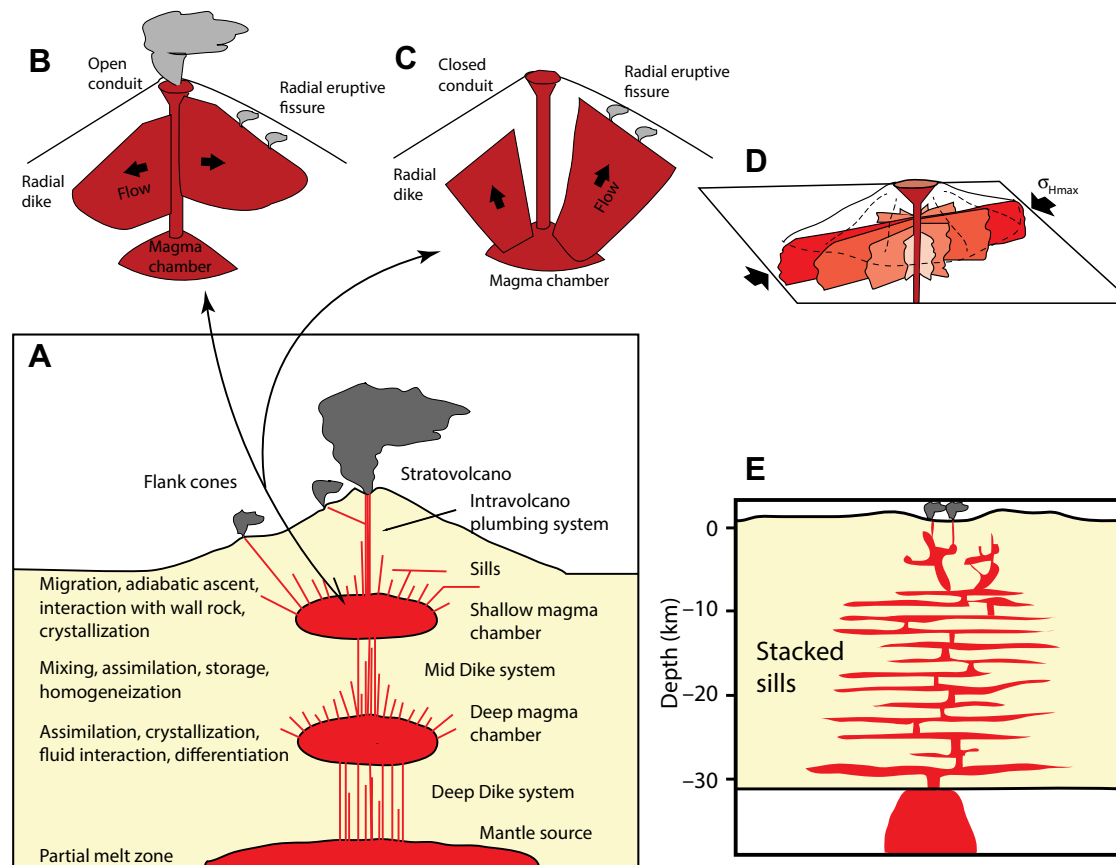
Figure 7. Models for volcano plumbing systems. (A) Schematic illustration of a magma plumbing system dominated by a network of vertical, inclined, and horizontal intrusions that channel magma toward the surface and link magma storage chambers. Section not to scale. Description on left side derived from subdivision of granitic plumbing system (Atherton, 1993). (B) Radial dikes propagating from feeder pipe. (C) Radial dikes propagating from magma chamber. (D) Preferred dike orientation due to maximum horizontal stress (σ_{Hmax}) orientation. (E) Volcano fed by sill complexes within the crust. Based on figures in Tibaldi (2015).

2008; Muirhead et al., 2012; Jaxybulatov et al., 2014; Cashman and Giordano, 2014; Koulakov et al., 2016). It is also possible that feeder systems between the magma chamber and the volcano have oblique dips (Aizawa et al., 2014). In a review of volcanic plumbing systems Tibaldi (2015) notes that "plumbing systems can go from very simple dike complexes made of tens to thousands (of) parallel vertical dikes that link the magma chamber to the uppermost volcano conduit, to a very complex intrusive plexus made of dikes, sills and inclined sheets, which interconnect multiple shallow magma chambers."

At the regional scale volcanic field alignment, associated with propagation of magma is a consequence of the interplay between deep factors related to the nature of the magma source area and shallow level influences such as stress field and preexisting structures within the crust (see review by Le Corvec et al., 2013). In rifts dike swarms are commonly regionally aligned in a preferred orientation parallel or sub-parallel to the regional tectonic maximum horizontal stress direction (e.g., Anderson, 1939, 1951; Odé, 1957; Muller and Pollard, 1977; Smith, 1987). More locally, however, dike sets can lose the regional trend and exhibit a variety of orientations including: well-organized radial patterns, less ordered fishing net patterns, and concentric, inclined cone sheets and ring dikes (e.g., Bailey et al., 1924; Anderson, 1939, 1951; Phillips, 1974; Tibaldi et al., 2011). Radial patterns are commonly developed around volcanic pipes and can be related to complex interactions between regional stresses, magma pressure, and dike-induced stresses (e.g., Mériaux and Lister, 2002; Kühn and Dahm, 2008). Shallow magma chambers at depths between ~1 and 6 km are known from a number of volcanoes (e.g., Walker, 1958; Hald et al., 1971; Ryan, 1988; Fialko and Rubin, 1998; Cervelli and Miklius, 2003; Amelung and Day, 2002; Tibaldi et al., 2011; Baker and Amelung, 2012; González et al., 2013). Above shallow magma chambers, particularly mafic ones, arrays of cone sheets and ring dikes that converge on a central area focused on the

magma chamber are commonly present (e.g., Bailey et al., 1924; Anderson, 1939; see review in Tibaldi, 2015). These authors consider over-pressured magma chambers to be the primary cause of the intrusions. Cone sheets range between 5 km and 20 km in diameter (average 12.3 km), and intrusion widths are typically 0.2–1.8 m, with the thickest up to 10–12 m, and an average width of 0.93 m (Tibaldi, 2015).

As described above many intrusions associated with volcano plumbing systems are steeply inclined, with sills being of secondary importance. However, there is a range of evidence that sills are significant features of some plumbing systems. For the 2010 Eyjafjallajökull explosive eruption, in Iceland, GPS and interferometry data indicated that before the eruption a 0.05 km³ magmatic intrusion grew over three months and exhibited both temporal and spatial complexity. The sills were focused at depths between ~5000 and 7000 m below the surface (Sigmundsson et al., 2010). The study indicates that geodetically sill-shaped sources of deflation are present and that magma can be drained from sills. Progressive inflow from depth caused pressure build-up that led to eruption. The presence of multiple storage areas and pathways to a volcano can result in eruption of different types of magma from the same volcano, for example with the Karymsky Volcano, in Russia, andesite was erupted from the main vent, while basalt was erupted from its flank (Eichelberger et al., 2006).

The Paiute Ridge complex, USA, shows igneous intrusive geometries emplaced beneath a small alkali basaltic volcanic center (Valentine and Krogh, 2006). Dikes tended to run perpendicular to the extension direction ($\sigma3$). While sills that locally lie along the dikes consistently occur in the hangingwall block of the dike-injected faults, with the dips of the fault blocks determining the direction of magma flow, which is up-dip. The three largest sills developed lopolith geometries. The localized control by preexisting structure is suggested by the authors to be a feature of the upper few hundred meters of an existing extensional system with heterogeneous lithologies.

The Toba supervolcano as described by Koulakov et al. (2016) illustrates some of the complexities that can arise within a plumbing system. The 38-km-thick continental crust is an obstacle to basic magmas, which are not sufficiently buoyant to rise to the surface. Consequently, melts and fluids from the subducting slab have been stored in a large magma reservoir near the base of the crust. This storage is a strong heat source, and also a source of overheated volatiles, which migrate upwards. In turn the volatiles cause heating of silicic rocks in the middle and upper crust. These shallow magma reservoirs formed predominantly in stacked sills and laccoliths at ~10–20 km depth, and the shallow magmas are viscous and explosive.

In large complexes of sills, the transgressive parts of sills result in interconnection of underlying and overlying sills. Hence magma does not necessarily have to move along vertical feeder pipes or dikes but can step up by moving along a series of horizontal and inclined pathways in interconnected sill-feeding-sill networks (Fig. 7E; Marsh, 2004; Cartwright and Hansen, 2006; Muirhead et al., 2012; Magee et al., 2016; Schofield et al., 2016). Marsh (2004) described a vertically extensive, well-exposed system in the McMurdo Dry Valleys region of Antarctica, where lavas were connected to ultrabasic layered rocks by a se-

ries of sills and feeders. The system described by Marsh (2004) is important both for the geometry of the intrusive complex, and for understanding the complex chemistry of the magmatic system. The study concluded that the local size and shape of the intrusive system, nature of wall rock involvement, and how the flux of magma and flushing frequency occur all affect magma composition. Magma diversity results from quite random juxtaposition of crystals and melt that then attempt to reach physical and chemical equilibrium, and that for such systems there is no primary magma (Marsh, 2004).

■ 4. METHODOLOGY

This study is based on interpretation of the Kora 3-D seismic survey from the 2017 open-file data pack provided by New Zealand Petroleum and Minerals. The marine seismic survey acquired by the operator ARCO Petroleum New Zealand Inc. covers an area of 750 km², it is 66 fold, has a bin size of 12.25 × 25 m, the source was a dual airgun, the streamer comprised four cables, 4950 m long, towed at 8 m depth, with 396 channels per streamer. Inlines were acquired in a WNW-ESE direction. The 3-D data is generally high-quality, with a pre-stack time migration processing sequence. European polarity was maintained throughout the processing. A positive acoustic impedance increase with depth for zero phase data is marked by a positive (black) peak, while troughs are red.

Wells Kora 1-1A, 2, 3, and 4 were available in the data pack, and were useful for tying the stratigraphy to the seismic data (see also Bischoff et al., 2017; Infante-Paez and Marfurt, 2017). Based on the Ariki-1 sonic log, the average velocity through the Paleogene interval is around 3300 m/s, while for the Cretaceous it is around 3800 m/s.

Horizons 1, 2, 3, and 4 (Figs. 4, 6, and 8) were mapped to help understand the way stratigraphic and structural variations have influenced intrusive distribution. The most important of these horizons is Horizon 1, which marks the base of the syn-rift section (base Cretaceous syn-rift; Fig. 6). The horizons were picked every twenty lines and crosslines. Horizon 1 was picked manually because the reflections marking the base of the syn-rift section were highly discontinuous, and often affected by igneous intrusions lying close to the basement-syn-rift interface. Syn-rift faults were also interpreted. The Kora Volcano lies in the central part of the seismic survey and has wiped out the seismic data in a circular region with a radius of ~2.5 km. The trends of faults, and the base syn-rift horizon were projected through this region to match up with better imaged regions near the borders of the 3-D seismic data. However, the loss of the basement reflection due to stacks of sills in the depocenters, and the effects of the Kora Volcano mean that the base syn-rift is a highly subjective interpretation. I am confident that the overall fault trends, basement contours, and deepening of the basement to the south is correct. But having made multiple interpretations of the base syn-rift horizon it is apparent that there is sufficient latitude in decision making that even a single interpreter will map the horizon somewhat differently with each attempt. The fault patterns, and base syn-rift
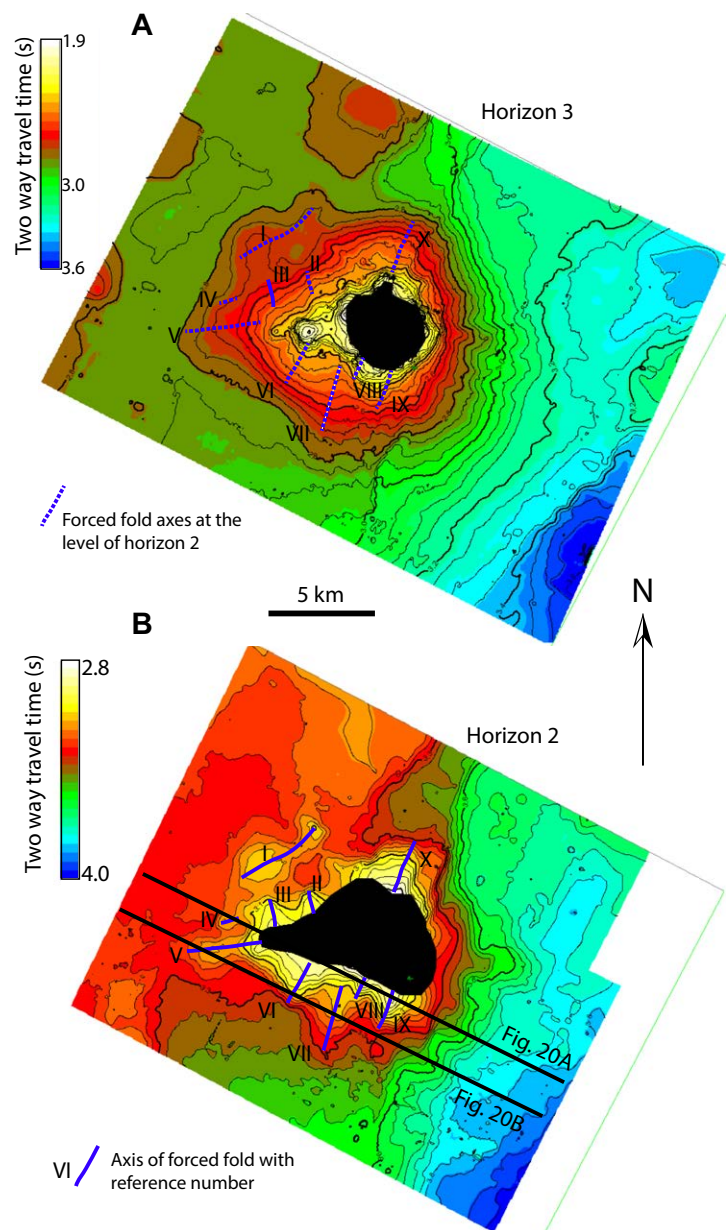
Figure 8. 3-D seismic-based time-structure maps of (A) Horizon 3 (top Eocene) and (B) Horizon 2 (top Paleocene syn-rift), of the Kora area in the Taranaki Basin, offshore New Zealand. See Figure 4 for location of horizons on seismic line.

horizon in the NNE and WNW side, tend to be quite consistent, although the presence of sills causes some problems and interpretation variations. The presence of a deep basin is quite apparent in the southern area. But the fault patterns and location of the base syn-rift horizon in the central and southern area are where the key variations in the interpretation lie. However, despite the uncertainty the interpretation is sufficiently reliable to allow the interaction between sills and the syn-rift structure to be investigated.

There are many high-amplitude intrusives in the pre-Miocene section some are easy to identify from attributes (e.g., amplitudes, root mean square amplitudes, coherency; Smallwood and Maresh, 2002; Thomson, 2005). Consequently, attribute extraction can reveal the general morphology of the sills (see examples for the Kora Volcano in Bischoff et al., 2017). However, there are a number of horizons that also have high amplitudes that tend to be at least partially extracted along with the intrusions, and also energy absorption within a stack of sills can result in dimming of amplitudes from deeper sills, which subsequently may not be extracted. Consequently, while amplitude extraction, or a combination of attributes, provide good first pass tools to image intrusions, there are some problems. For a more detailed understanding of the intrusion morphology over one hundred individual sills were mapped as horizons. From the mapped sills it is easy to define basic parameters such as shape, elongation direction, dip and strike orientations, area, and maximum dip values in order to assess how sills have interacted with the syn-rift stratigraphy and structure. Some sills were isolated and their boundaries could be mapped with confidence. In stacks of sills it becomes more difficult in places to define where one sill ends and another begins, so some definition of sill boundaries is subjective. There is also the practical aspect that seismic interpretation software in general, and Seismic Micro-Technology, Inc. Kingdom Suite used in this study, does not permit horizons to overlap themselves so that in any vertical plane the horizon can only be present in one locality. Hence even if an intrusion had a tortuous path spiraling up vertically, it could not be mapped as a single horizon. It would have to be mapped as a series of separate, stacked intrusives. Hence intrusions in this project were mapped quite commonly as relatively simple saucer-shaped sills, the transgressive parts of the sills could either cut across, or stop at higher level sills, but not join them as the same sill.

High-amplitude reflections may commonly correspond with the top contact between the host rock and an intrusion (Smallwood and Maresh, 2002; Thomson, 2005). When the intrusions are sufficiently thick, sometimes both the upper and lower contacts are imaged (Jackson et al., 2013). However, more typically minor intrusions such as sills and small laccoliths are insufficiently thick to be fully resolved and instead are imaged as tuned reflectors (Smallwood and Maresh, 2002; Magee et al., 2015). While the broad characteristics of the intrusions can be determined from tuned reflection packages, thickness can only be estimated. Although many intrusions can be imaged and mapped out for a variety of reasons (e.g., energy absorption, thickness, steep dips) not all intrusions will be imaged, and low-angle intrusions will be much more likely to be imaged than steeply dipping ones. Consequently, it is anticipated that high-angle transgressive segments of sills and dikes will be poorly repre-

sented or absent in this study. Also, sills may well continue beyond the areas where they have been mapped in this study, but due to issues of thickness, interference with other sills, the loss of data around the Kora Volcano, and energy absorption they cannot be reliably mapped.

There are clearly limitations to the reliability of the data for both defining sills and the syn-rift morphology. Nevertheless, the data is sufficiently good that it can provide important insights into the interaction between volcano-related intrusives and the syn-rift architecture.

■ 5. RESULTS

5.1. Syn-Rift Structure

The maximum relief from the base of the syn-rift section to the base of the Kora Volcano is 3.3 s two way travel time (TWT) or ~5.7 km. Hence this study is focused on intrusive complexes in approximately the upper 6 km of crust. The syn-rift section is best imaged on NNE-SSW–trending lines in the western part of the survey area, and on WNW-ESE lines in the northern and southern parts of the survey (Figs. 2 and 3). A series of representative crosslines (NNE-SSW) and inlines (WNW-ESE) are shown in Appendix 1 (Figs. A1.1–A1.15). The crosslines best image the NW-SE–trending faults on the west side of the area (Figs. A1.1, A1.2). Passing eastwards, the data quality becomes reduced around the Kora Volcano (Figs. A1.3, A1.4) and farther east the lines trend highly oblique to N-S to NNE-SSW–trending faults (Figs. A1.5–A1.7).

The northern area exhibits a relatively shallow depth to the base syn-rift horizon and overall is dominated by a N-S–trending half graben geometry with a major ESE-dipping bounding Fault 2 that strikes NNE-SSW and runs through the middle of the survey (Figs. 6 and A1.8–A1.10). The footwall of Fault 2 is a high, eroded area in the north, but passing south the basin deepens, fault displacement becomes less, and the eroded high is lost (Fig. 6 and the series of sections in Figs. A1.8–A1.15). The half graben is affected by up to five secondary ENE-dipping normal faults (Figs. 6 and A1.8–A1.11). The half graben becomes thicker passing toward the south. The geometry is complicated by the presence of several NW-SE–trending faults. The largest of these faults (Fault 1) is seen in the SW part of the survey where it dips to the NE and controls a thick half graben basin fill (Figs. 6, A1.1, A1.2, and A1.15).

On the WNW, SSW, and ESE margins of the basin intrusions are sparse (Figs. A1.1, A1.7, and A1.15). They tend to lie near the base of the syn-rift sequence, or as sills within the basin fill that are conformable with reflections from bedding. On the NNE margin the important fault, and fault-controlled depocenter influence on sill distribution, can be seen (Figs. A1.8, A1.9). The sills tend to be planar (conformable with stratigraphy) or saucer-shaped and confined by the fault blocks. The known timing of igneous activity is related with the onset of subduction in the Miocene (Giba et al., 2010, 2013), hence it is assumed that the sills were emplaced during the Miocene, while fault activity was during the Late Cretaceous–Paleocene. Consequently, although it

may look as if the faults are offsetting sills, this cannot be the case. Commonly approaching the faults, the sills become inclined in the same direction as the faults. In some cases the sills follow the fault planes (e.g., Fault 2, Fig. A1.9), but in other examples it is the dip direction that is followed, but the dip is gentler than the fault. Such dips may arise due to local stress deflection, or because bedding has been rotated near the fault (as discussed in the context of Fig. 9 below).

In Figure 9 examples of variations in boundary fault geometry are shown from 3-D data crossing a Cenozoic rift in the Gulf of Thailand. The data is shown to illustrate how bedding geometries can vary adjacent to a large extensional fault. In Figure 9C there is little folding of the hangingwall, while in Figures 9A and 9B a fault propagation fold is well developed. The sketches (A1, B1, and C1) in Figure 9 show how sills that partially follow bedding and faults can exhibit different relationships with the fault depending upon the configuration of bedding in the hangingwall. There are four basic relationships in the Figure 9 sketches A1, B1, and C1: sill type 1 is a saucer-shaped sill independent of the structural geometry, type 2 are sills conformable to bedding that meet and follow faults, type 3 are sills that steepen by following a steep fold limb and intersect the fault and may or may not follow it, while type 4 sills follow the steep fold limb but remain in the hangingwall. These variations in geometry are probably appropriate for the Kora area, but are not always easy to demonstrate due to degradation of stratigraphic reflections in areas of igneous intrusions.

Approaching the Kora Volcano sills in the depocenter become stacked increasingly higher as the depocenter become thicker. Figure A1.10 shows the start of the transition where the Paleogene section becomes folded by the intrusions (horizons 2 and 3). Fault 3 is the focus of intrusive activity. This zone contains a mixture of cross-cutting intrusions, some dip to the west following the stratigraphy, while others dip more steeply to the east. Although vertical dikes may be present, the seismic data indicates that transgressive sill segments are present and were capable of transporting magma to higher stratigraphic levels in this structurally heterogeneous system. Figure A1.11 is similar to Figure A1.10, but shows the loss of information about the hangingwall section of faults 2 and 3. In Figures A1.12 and A1.13 the loss of information below the Kora Volcano is most extensive. The sections illustrate an increasing thickness of the hangingwall depocenter of Fault 3, which enables a stack of sills across an interval ~3 km thick to develop. This contrasts with the footwall area of Fault 2, which is comparatively thin with respect to the Fault 3 hangingwall area, and exhibits relatively few intrusions. The combination of sills following stratigraphic dip in the footwall of Fault 2, and sills following the dip direction of Fault 3 results in the majority of sills being inclined away from the Kora Volcano.

South of the Kora Volcano where faults 1, 2, 11, and 12 control the depocenter, there are stacks of sills which are imaged on Figures A1.5, A1.6, and A1.14 that occupy the thick depocenter. The upper parts of the sill stacks are well imaged but the deeper section exhibits generally weak reflectivity probably due to energy absorption by the higher sills. Farther south from the sills Figure A1.15 provides a better image of the syn-rift section, where only a few sills are present near the base of the syn-rift section.
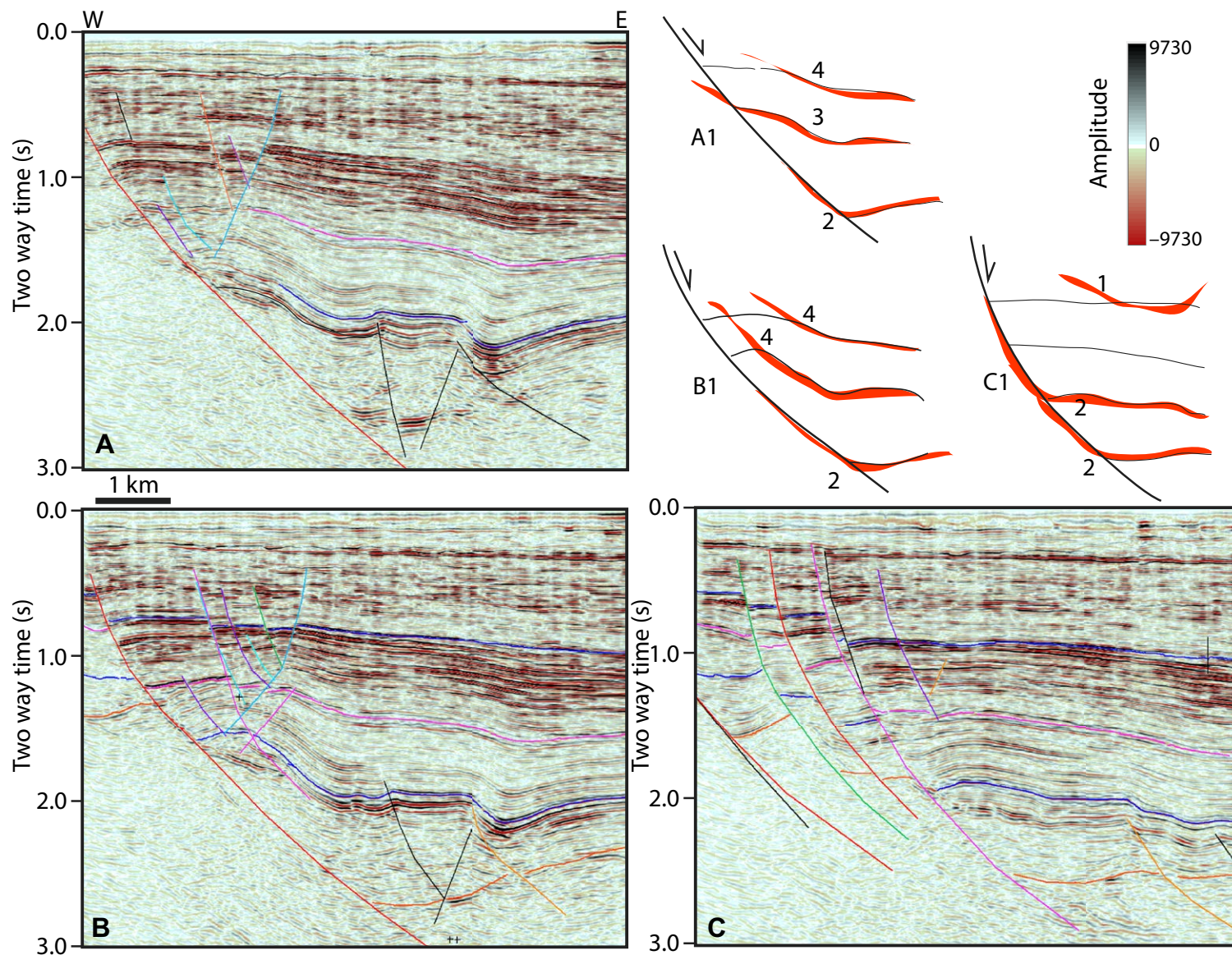
Figure 9. 3-D seismic lines across a boundary fault in the Songkhla Basin, Gulf of Thailand, illustrating varying dip patterns in the hangingwall of a major bounding fault zone (red, purple faults). (A) Moderate dips and fault propagation fold in hangingwall. (B) Well-developed fault propagation fold. (C) No fault propagation fold. A1, B1, and C1 are sketches of the faults similar to those in A, B, and C, respectively, illustrating variations in sill morphology as a consequence of the fault and hangingwall bedding geometry. (1) Saucer-shaped sill developed independent of fault and bedding morphology. (2) Sill follows bedding and exhibits transgressive segment following the fault trajectory. (3) Sill follows folded bedding and exhibits apparent transgressive segment on fold limb, and cuts across fault. (4) Sill confined to hangingwall follows folded bedding and exhibits apparent transgressive segment on fold limb, which evolves into transgressive segment that cross-cuts bedding where bedding flattens into the fold crest.
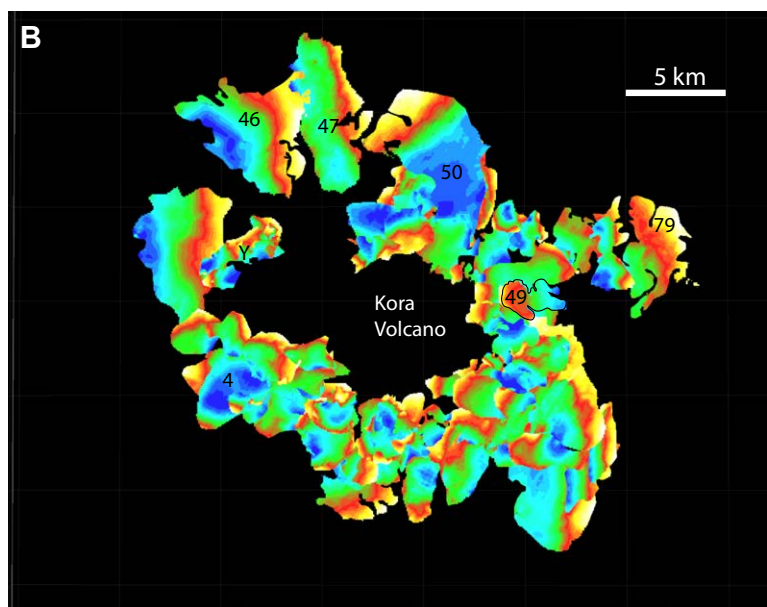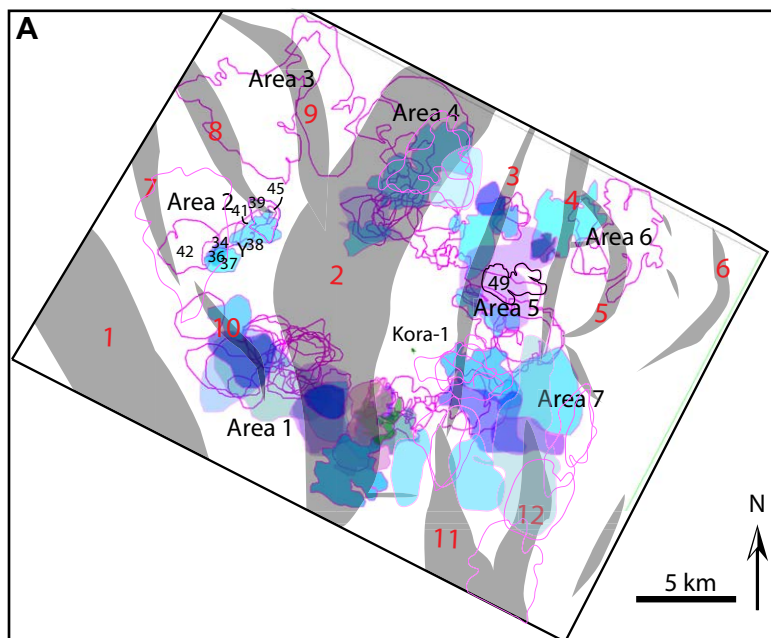
Visualization of the sill geometries in 3-D is difficult due to the number of sills present and their closely spaced, overlapping nature. Figure 10A shows the polygon outlines of the 108 sills that have been mapped in this project, superimposed on the fault polygon map of the base Late Cretaceous syn-rift section (Fig. 6). The overlapping sills are shown in map view in Figure 10B, the color bar values are different for each sill, hence no values can be shown, but the relative depths (blue deep, yellow shallowest) can be used to see the dip directions of the sills. In the map view many sills are partially or completely obscured by overlying sills. Two 3-D perspective views of the sills are provided in Figure 11. Some sills have been numbered in both Figures 10B and 11 to better help understand the viewing direction, these numbers correspond to the sill numbers given in Appendix 2 (Figs. A2.1–A2.5).

Horizons following the top and base of the section affected by sills have been mapped, and an isochron map (time-depth thickness map in two way travel time) has been made by subtracting the top map from the base (Fig. 12). The isochron map shows the intrusion-affected interval thickens toward the Kora Volcano with an approximately circular to oval distribution of contours concentric to the volcano (Fig. 12). In Figure 12 six different areas have been defined, which are discussed below in the context of the impact of the syn-rift morphology on sill distribution.

Area 1 contains a complex of sills that is elongate in a WNW-ESE direction. It traverses the thickest syn-rift section in the Kora 3-D survey, and two depocenters, controlled by faults 1 and 2, which cause the elongation. There are two areas where the sill interval thickness contours are elongated in a southwesterly direction, the western one is in the depocenter of Fault 1, while the eastern on is along the trend of Fault 2, following the hangingwall depocenter.

Area 2 is a region where the lower part of the seismic section contains little mappable reflectivity, hence the isochron map (Fig. 12) has no data. The top of the intrusives is a high area that follows a narrow NE-SW–trending ridge (location Y in Fig. 10). The trend lies orthogonal to the strike of the base syn-rift horizon contours and runs between the tips of two NW-SE–trending faults. This may be an indication of structural control or a coincidence. However, areas 2 and 3 are regions where the base syn-rift horizon becomes increasingly shallow passing NNE-wards as a tilted fault block, high in the footwall of Fault 2 (Figs. A1.1, A1.2, A1.8 and A1.9). Consequently, the relatively restricted interval of intrusions in Figure 12 is a result of this structural geometry.

Figure 10. Distribution of mapped sills in the study area, in the Kora area of the Taranaki Basin, offshore New Zealand. (A) Outlines of all the mapped sills in the study area. Fault polygons at the base syn-rift section (Fig. 6) are shown with fault numbers in red. The sill polygons shown in various shades of blue and purple highlights the sills at the lowest parts of the section. (B) Map of all the mapped sills in this study. The sills occur at different levels in the basin, hence the colors are only relative values where blue is the deepest part of the sill and yellow is the highest part. All the mapped sills are shown in Appendix 2. Selectively numbered sills (4, 46, 47, 50, 79) have the same numbers in Appendix 2. There are 108 mapped sills, hence in these figures it is not possible to see all the sills because in many places the sills are stacked. However, the figures do show the general distribution of the sills. Y—location reference.
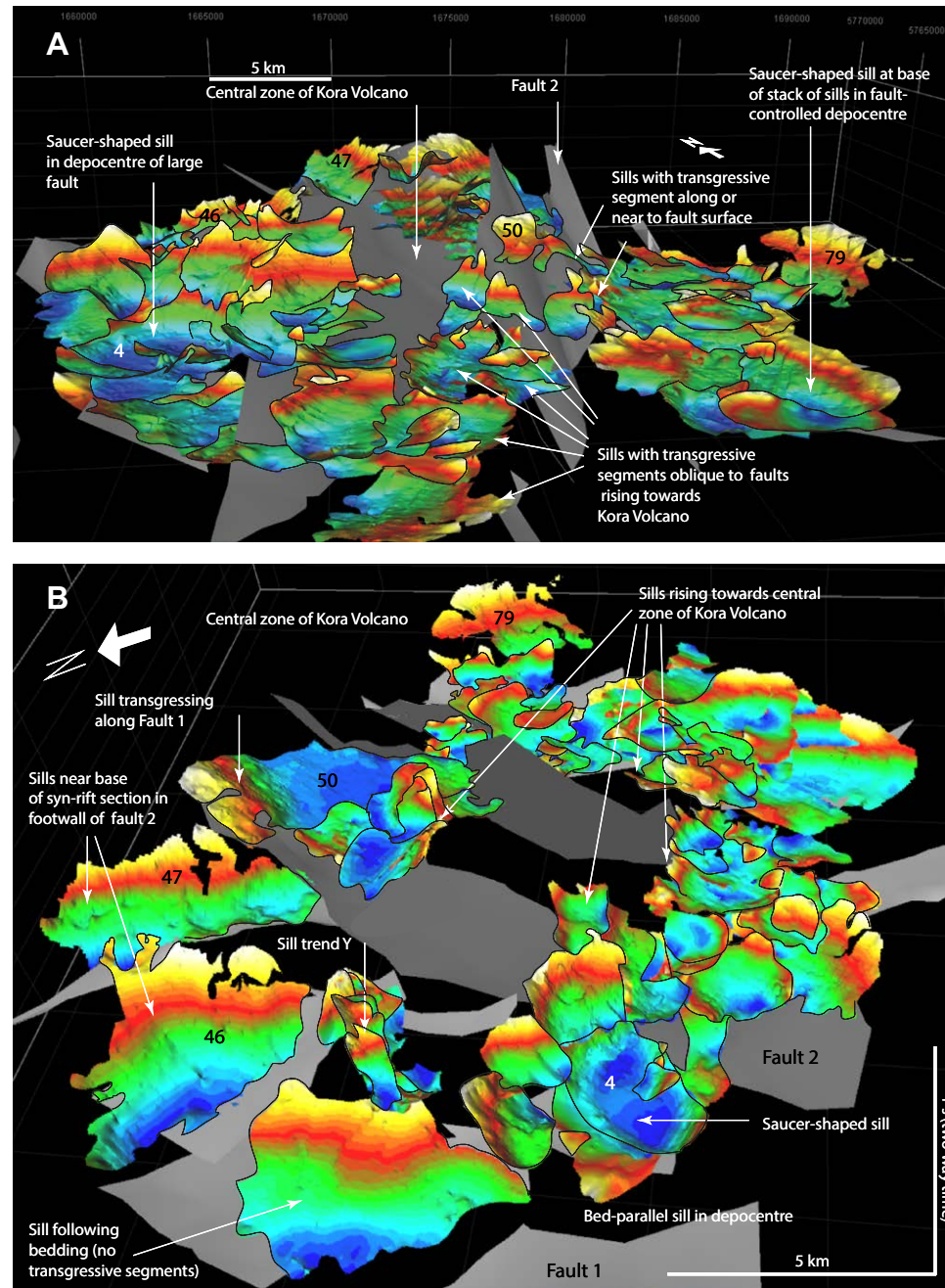
Figure 11. Oblique perspective views of sills shown in Figure 10B, in the Kora area of the Taranaki Basin, offshore New Zealand. (A) View to the NE. (B) View to the ESE. The sills occur at different levels in the basin, hence the colors are only relative values where blue is the deepest part of the sill and yellow is the highest part. All the mapped sills are shown in Appendix 2. Selectively numbered sills (4, 46, 47, 50, 79) have the same numbers in Appendix 2 and in Figure 10B.
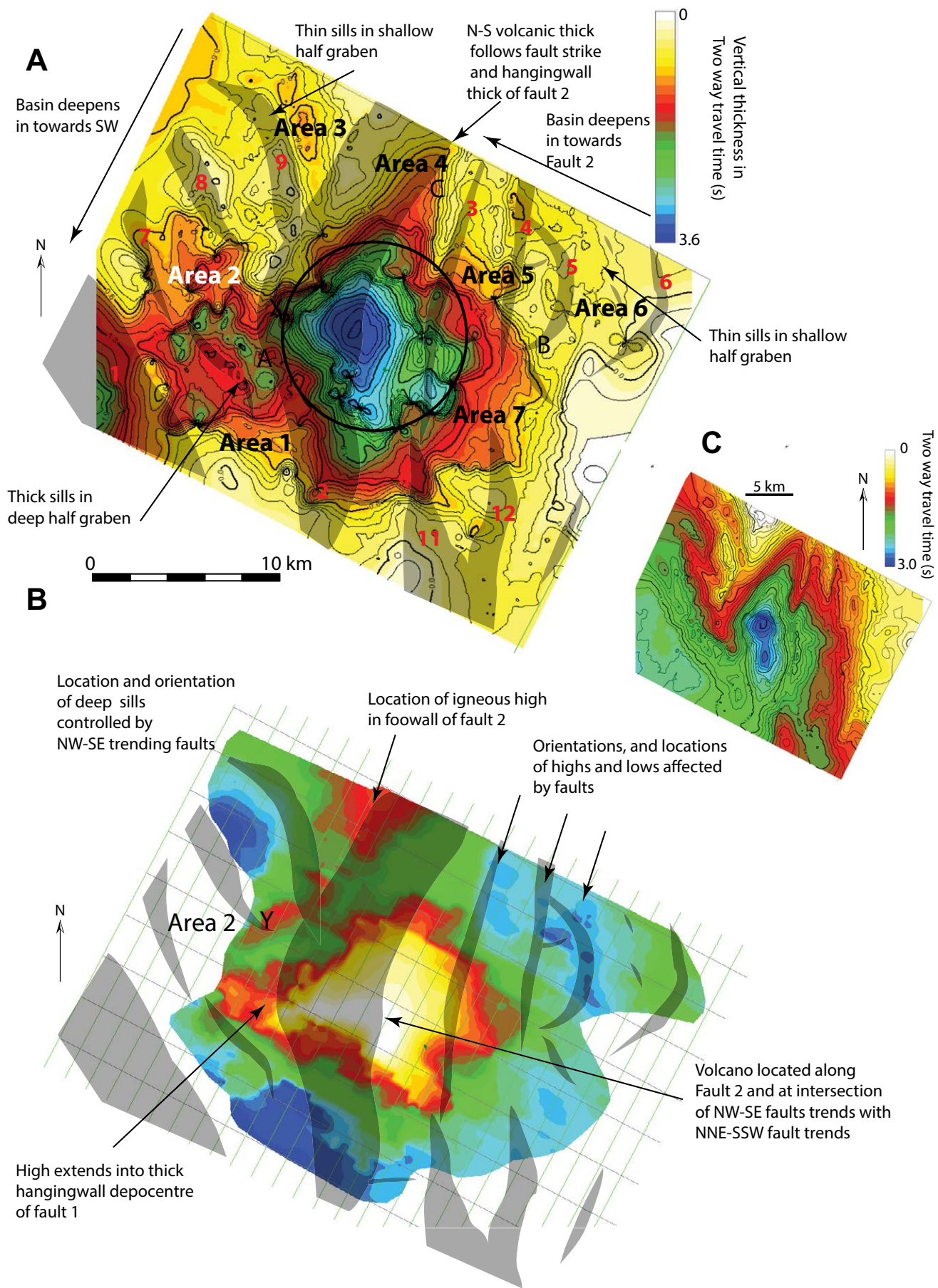
Figure 12. (A) Isochron map of thickness, in two way travel time, of sill-affected interval within the Cretaceous–Paleogene section, in the Kora area of the Taranaki Basin, offshore New Zealand. This map was generated by subtracting the time structure map at the top of the section affected by sills (Fig. 12B) from the base of the syn-rift section map (Fig. 6) made without the presence of fault polygons. (B) Time-structure map of the top of the section affected by sills. (C) Isochron map of thickness, in two way travel time, of the section from the base syn-rift (Horizon 1) to the base of the Kora Volcano section (Horizon 4).

The morphology of the intrusions is different in the two areas. In Area 3 the sills form a narrow NE-SW–trending ridge, while in Area 2 the sills form extensive sheets that lie within the Cretaceous syn-rift section near, and sub-parallel to, the contact with the underlying Permian volcanic basement.

Area 4 is the depocenter in the hangingwall of Fault 2. Passing to the NNE the thinning of the intruded interval loses the contour trend that is concentric to the volcano (i.e., E-W to WNW-ESE) and instead becomes elongated to the NNE to lie parallel to the fault, indicating that the presence of the fault-controlled depocenter influenced the NNE elongation of the sill trend.

Area 5 is a region with a thick stack of sills in a depocenter somewhat similar to areas 1 and 4. While Area 6 is the tapering margin of a half graben depocenter. Similar to Area 3 it has a thin zone of sills that are areally widespread and extend farther from the Kora Volcano than the sills in deep depocenters (Area 1 for example).

5.2. Intrusion Morphology

The general relationships of sills to the syn-rift structure is described in the previous section. This section describes in more detail the geometries of individual sills, and how those geometries may relate or do not relate to the syn-rift basin morphology and structure. An overview of the range of sill shapes in map view, size, and their general contour patterns is provided in Appendix 2, which shows 108 of the mapped sills as thumbnail maps (Figs. A2.1–A2.5). Figure 13 shows in more detail a few examples of common sill geometries. The color values in Appendix 2 are relative (i.e., blue is deep, red to yellow is shallow), with the range of time-depths for each map given below each map.

The intrusions vary considerably in orientation, dip amount, area, and map view shape. There are three common kinds of sill morphology in the Kora 3-D survey: saucer shaped (Appendix 2, Figs. A2.1–A2.5, numbers 1–11, 34–37, 50–58, 66–69, 83–90), bed-parallel and mixed bed-parallel, and transgressive segments (i.e., cross-cutting bedding in a dominant direction, Fig. 13; Appendix 2, Figs. A2.1–A2.5, numbers 12–33, 38–43, 45–49, 59–65, 70–82, 91–108). A few sills have a domed morphology (Appendix 2, Figs. A2.1, A2.2, and A2.4, numbers 22, 41, 44, 73). Some sills between two faults dipping in the same direction can exhibit two transgressive segments dipping in the same direction, with a bed-parallel middle section. X-shapes can locally arise from cross-cutting sills.

An example of a typical sill is shown in Figure 14. Overall the sill dips to the east, following the dip of bedding, but is transgressive to bedding reflections in some places (particularly the western side, also in strike-sections E–E' and F–F'). Although the sill is a continuous feature on lines D–D' and C–C' at the southern, northern, and eastern margins it becomes lobate in map view and discontinuous. In section B–B' (Fig. 14) the amplitudes related to the sill dim in the middle and a break is shown in the horizon map. The sill may be physically present in the subsurface in the region of the break but the intrusion is thin and below tuning thickness on the seismic data. In G–G' the two lobes on the eastern side of the sill are shown, with a clear stepping down from the lobe cut by line D–D' to the lobe cut by line C–C'. The high amplitude reflections show a small overlap in section G–G', however, as mentioned in the methodology section the same horizon cannot be mapped twice where it is repeated vertically, so the detailed morphology cannot be exactly mapped. A narrow break is shown in map view to indicate the area where the horizon jumps down to the north. In the example in Figure 14 the sill is narrow in the strike direction and elongate in the dip direction, but many other examples are either equi-dimensional (Figs. A2.1–A2.5, e.g., numbers 2, 6, 12, 16, 18, 25, 27, 37, 39, 40, 42, 44, 48, 64, 73, 97) or elongate in the strike direction (Figs. A2.1–A2.5, e.g., numbers 11, 15, 46, 47, 62, 79, 98, 101, 108). The example is provided to show how sills in this study commonly show strong continuity in some areas, but break into lobes separated by gaps, steps, bridges, and broken bridges in other areas. These features are well known from other sill complexes (e.g., Pollard et al., 1975; Planke et al., 2005; Schofield et al., 2012a, 2012b; Magee et al., 2015).

The range of complex sill geometries is shown in Figure 15C, where sill dimensions as an ideal rectangular shape (length × width of sill) is compared with the actual area of the sill as a ratio. The higher the ratio, the smaller the area of the sill compared with the ideal rectangular shape, this is usually due to either a highly irregular lobate, or a triangular map view geometry (e.g., Figs. A2.2–A2.4, numbers 46, 55, 61, 79). The clustering of results with ratios around 1.2–1.4 are typical of moderately irregular rounded sill geometries (e.g., Fig. A2.1, numbers 1, 4, 24, 25).

There is considerable variety to the shape of sills in Appendix 2, with some being highly lobate, while others have straight or curved edges, and a simple oval, rectangular, or curved-polygonal outline. There are several reasons for the irregular shapes including: local seismic degradation (e.g., energy absorption from overlying sills), intersection of a sill with another intrusion, the intrusion splitting into different lobes either within the same horizon or at different stratigraphic levels, and variations in sill thickness (and hence amplitude).

5.3. Sill Shape

In Appendix 2, Figures A2.1–A2.5, 36 of the sills have well-developed synformal geometries, while the other 72 are more predominantly inclined or transgressive in one direction or have geometries inconsistent with a synformal shape. Of the 36 synformal sills, 32 occur in areas of thick depocenters (areas 1, 4, and 5), while only four occur in areas 2, 3, and 6 (Fig. 12). The sills can be restricted by the fault bound blocks and by competition with surrounding intrusions. Of the 11 synformal sills that exceed an area of 10 km^2, seven come from the lower part of the stack (average area 11.3 km^2) while three come from the upper part of the stack (average area 18 km^2), and only one (15.5 km^2) is from the middle part. Hence the largest sills seem to be preferentially developed in the lower part of the sill stack.
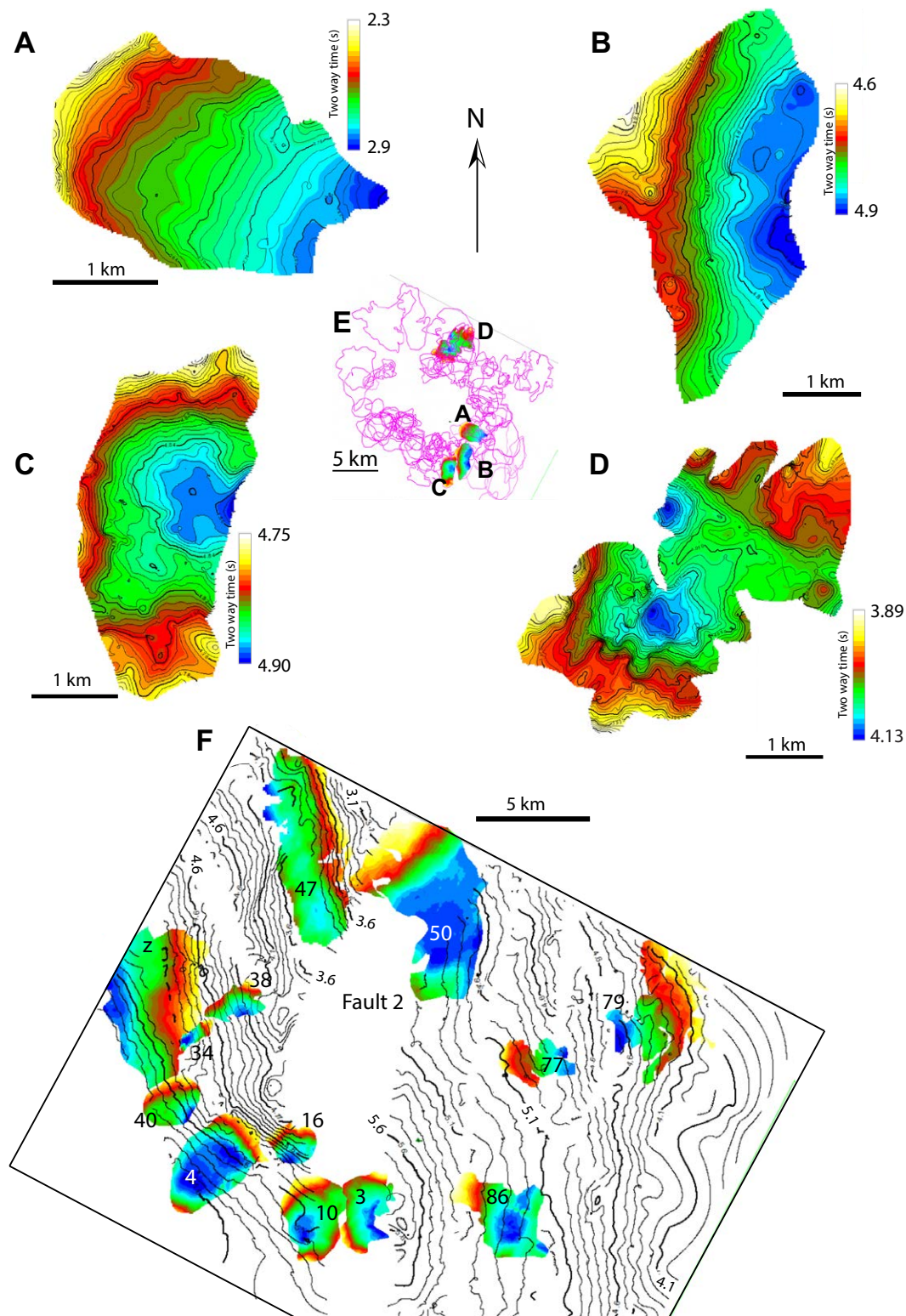
Figure 13. Examples of some common sill morphologies in the Kora 3-D seismic data, of the Kora area in the Taranaki Basin, offshore New Zealand. (A) Transgressive sill elongate in the dip direction (Appendix 2, number 93). (B) Transgressive sill elongate in the strike direction (Appendix 2, number 96). (C) Saucer-shaped sill, rounded map view outline (Appendix 2, number 98). (D) Saucer-shaped sill highly irregular map view outline (Appendix 2, number 16). (E) Map of polygonal outlines of sills mapped in the Kora area, showing location of sills in A–D. (F) Time-structure contour map of base syn-rift section (same as Fig. 6), showing selected sills that demonstrate the interaction or absence of interaction between sill morphology and structure. With the exception of sill Z, the sills are numbered according to Appendix 2. Sill Z is an example of a sill parallel to bedding, the sill therefore follows the dip and strike of syn-rift bedding, which closely corresponds with that of the base-syn rift. Sill 3, elongate parallel to structure, dips are partially parallel to structure contours and Fault 2 (both N-S). Sill 4, elongate perpendicular to structure, with structure contours predominantly parallel to the base syn-rift contours. Unlike sill 3, saucer-shaped sill 10 shows little correspondence with structure (sub-perpendicular to contours). Sill 16, partial correspondence between structure contours, does not show preferred shape trend. Sill 40, elongate perpendicular to contours, structure contours are perpendicular to base syn-rift contours. Sills 34 and 38 are part of the NE-SW intrusive trend, both are elongate perpendicular to base-syn rift structure contours, sill 34 time-structure contours are parallel to base syn-rift contours, sill 38 structure contours are sub-perpendicular to base syn-rift contours. Sill 47, sill near interface between syn-rift and pre-rift section, very closely follows time-structure contours at base syn-rift and shape is elongate parallel to base syn-rift contours. Sill 50, shape constrained by faults on eastern side and NW part follows Fault 2 (white gap in contours), time-structure contours of sill is parallel to and in the direction of Fault 2. Sill 79, similar to Sill 47, lies near the interface between the syn-rift and pre-rift section, very closely follows time-structure contours at base syn-rift, and shape is elongate parallel to base syn-rift contours. Sill 77, elongate perpendicular to base syn-rift time-structure contours, time-structure contours are parallel to base-syn rift contours. Sill 86 is a saucer-shaped sill with a long transgressive segment opposite to base syn-rift dip that shows a partial correspondence between sill time-structure contour direction and base-syn-rift contours.
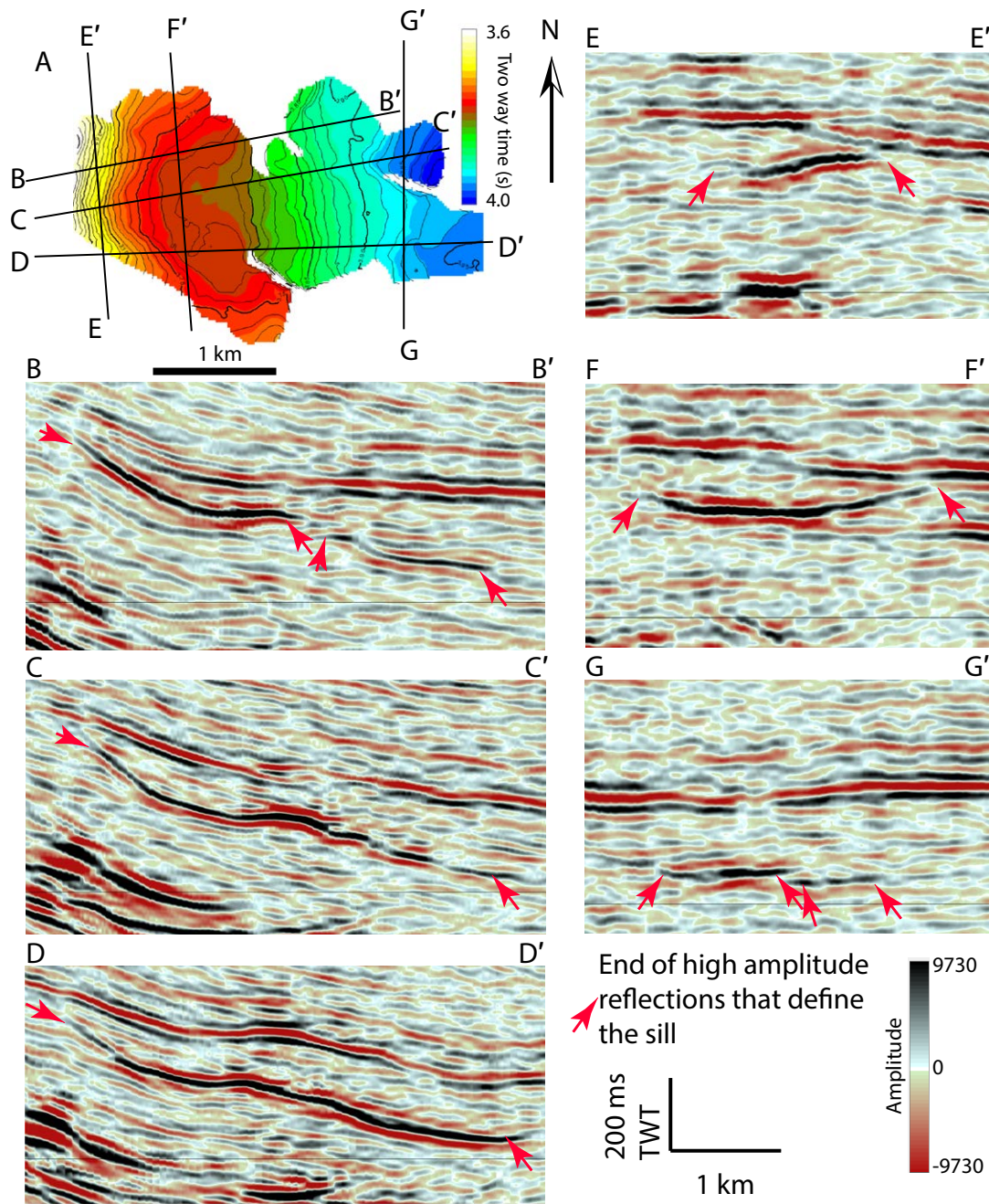
Figure 14. Example of a sill (Appendix 2, number 49) with common variations in morphology. See Figure 10 for location. TWT—two way travel time.
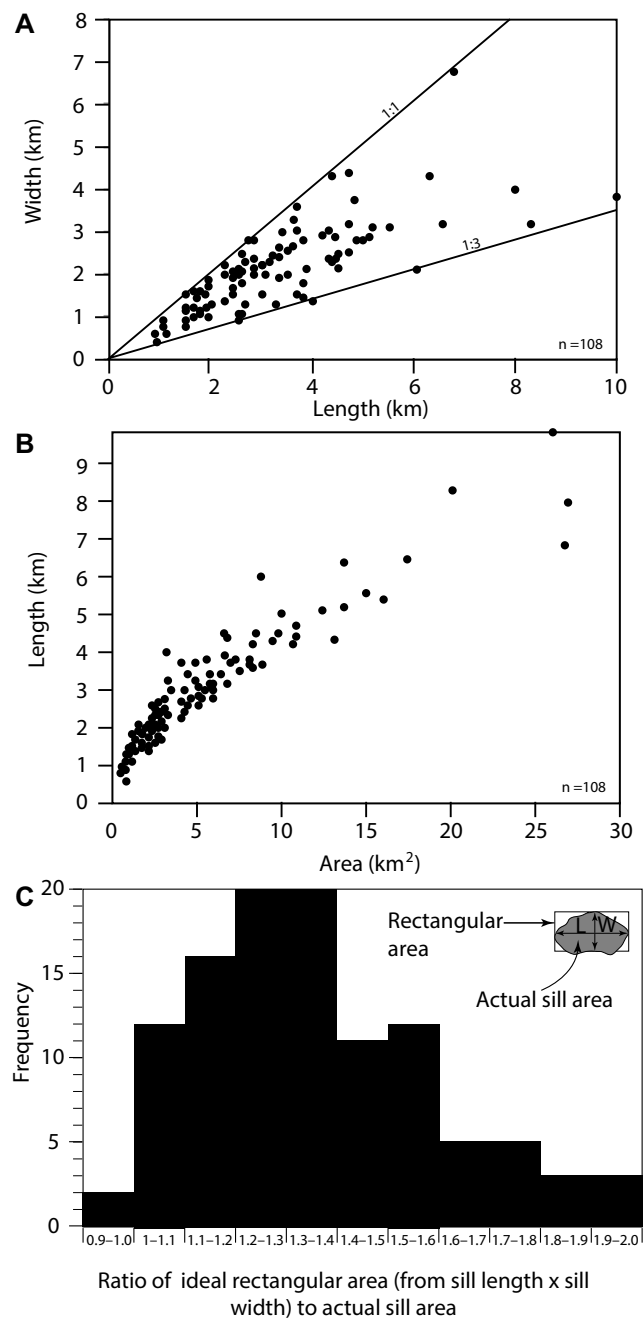
Figure 15. (A) Plot of sill length versus width for sills in Appendix 2, of the Kora area in the Taranaki Basin, offshore New Zealand. (B) Plot of sill length versus area for sills in Appendix 2. (C) Measure of sill shape irregularity by considering a rectangular area as an ideal shape. The ideal rectangular area of a sill is calculated based on length and width of each sill, and compared with the actual sill area as a ratio. The higher the ratio the more irregular the sill and the smaller the area compared with the ideal rectangular shape. Most sills have moderate ratios indicating they are irregular in shape (ratios between 1 and 1.4), often curved, but are not highly irregular.

In the areas of thinner syn-rift section the basal sills, close to the interface with Permian basement, lack a synformal geometry and in Area 3 (20 km^2 and 21 km^2) are more extensive, while in Area 6 (8.8 km^2 and 13.8 km^2) they are of similar extent. However, smaller sills overlying the basal sills do display synformal geometries. One isolated sill with an area of 24 km^2, that is almost entirely bedding parallel, lies west of the main concentration of sills, within the middle of the thick syn-rift sequence.

Sill Orientation with Respect to Basement Structure

Figure 13F shows 13 examples, large to small area sills, and how sill shape, dip, and strike can be related to syn-rift bedding orientation and faults. Some sills very closely follow the syn-rift structure (Fig. 13F, examples Z, 47, 79), while others are elongate perpendicular to structure (Fig. 13F, examples 4, 34, 77) and match the time-structure contour orientations, while other sills only have varying degrees of partial correspondence (Fig. 13F, examples 3, 10, 16, 38, 40, 50, 86). Of the mapped intrusion population 37% had the same strike direction (±10°) as the underlying base of the syn-rift section, while 24% exhibited two or more important strike directions, one of which coincided with the strike of the base syn-rift section, and 39% exhibited no correlation between intrusion strike orientation and the strike of the base of the syn-rift section. Intrusions often exhibited a preferred shape orientation, although 13% had no clear orientation. Width to length ratios range between 1:1 and 1:3 (Fig. 15A), this limited variation is reflected in a tight trend of length versus area values (Fig. 15B). Of the sills with a preferred orientation, 29% were oriented parallel to the strike of the base syn-rift section and 17% were oriented perpendicular, while 41% exhibited no correlation. The same strike and dip trends and shape orientation as the base syn-rift section occurred in 17% of the intrusions, 7% showed the same dip, with a shape orientation perpendicular to the base syn-rift strike. For partially coinciding dips, 9% had the same orientation and 5% had a perpendicular orientation to the base of the syn-rift section. There was 29% of the intrusion population that exhibited no coincidence of dip or orientation with the base of the syn-rift section.

The orientation of sill shape for some trends appears to be related to the orientation of faults (e.g., Fig. 13F, example 50), in Figure 16 a comparison of sill orientations and fault trends indicates that the preferred orientation of sills ranging between NW-SE and NNE-SSW can be explained by the influence of faults. The correlation between N-S oriented sills and N-S fault trends seems

A Sill shape orientation

13 sills had no preferreed orientation

n = 108

B Fault orientations

Per 1 km segment

n = 136 km

1 = E-W, 2 = WNW-ESE, 3 = NW-SE, 4 = NNW-SSE,
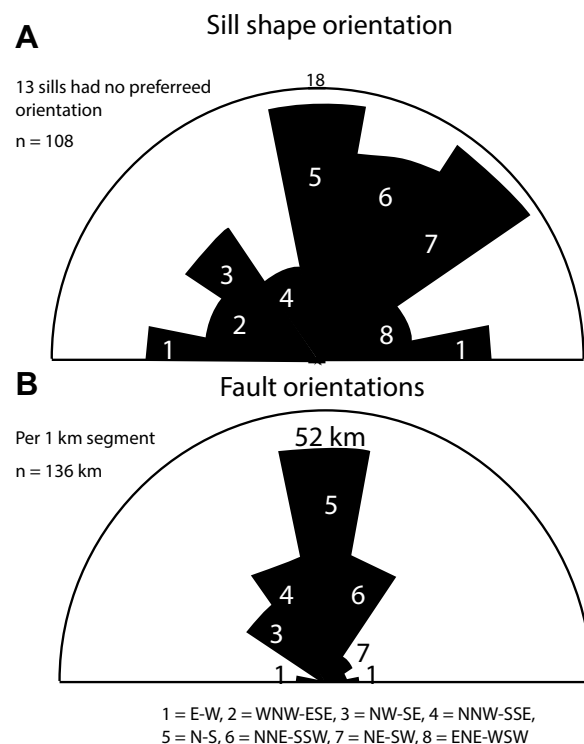5 = N-S, 6 = NNE-SSW, 7 = NE-SW, 8 = ENE-WSW

Figure 16. Sill shape orientation (A) for sills in Appendix 2, of the Kora area in the Taranaki Basin, offshore New Zealand, compared with fault orientation (B) at base syn-rift level (Fig. 6).

strong. The E-W trend may also be in part related to an orientation orthogonal to N-S–trending faults. However, the correlation between the NNW-SSE trend of faults (relatively high) and sills (relatively low) does not seem so compelling, and the pronounced NE-SW trend in sill orientation has no strong correlation with structure (either fault orientations or dip and strike of the base syn-rift section). This suggests there might be some influence by an underlying igneous trend (perhaps the orientation of a dike swarm). In particular, the NE-SW–trending intrusion related high in around location Y (Fig. 10), associated with the elongation of the Kora Volcano high to the west, might be related to some underlying igneous trend.

The main intrusions forming the NE-SW trend at location Y (Fig. 10) are shown in 3-D view in Figure 17. The complex contains relatively few intrusions that can be mapped, hence it is easier to visualize intrusion geometries in this trend than in other areas. There are three main types of intrusions present: (1) transgressive sills that link deeper areas to shallow areas that lie parallel to the NE-SW–trending forced fold that overlies the intrusive com-

plex, (2) shallow level saucer-shaped sills, and (3) shallow level sills that are transgressive in a single direction (Fig. 17). Since at least parts of sills are conformable to bedding, there is some correspondence between sill orientation and structure. However, it is also clear from Figure 17 that transgressive sills can exhibit a variety of orientations and that many sills at best will only partially exhibit shape or strike orientations that can be related to structure (Fig. 13F, example 38).

The stacks of sills in the depocenters tend to exhibit relatively short transgressive segments that dip toward the volcano, and long transgressive segments that lie closest to, and dip away from, the volcano. It is these long transgressive segments, with a height range up to 1.2 km, that are prone to linking sills at different levels. These sills provide pathways for upwards migration of magmas without the need for systems of dikes, although dikes may also occur. Figure 18 is a plot of height of sills versus area. It is noticeable that many relatively small sills display large heights (up to 1.2 km). These sills tend to correspond with long, narrow transgressive sills, or transgressive segments of saucer-shaped sills that climb toward the Kora Volcano. Maximum dips of individual sills (calculated as an average over 500 m horizontal distance crossing the tightest structure contour gradients) is shown to predominantly range up to ~30° with a few examples ranging as high as 45°. This is based on the mapped sills, there are some steeper intrusions imaged that were not mapped, but measured from individual seismic lines that dip up to 58°. These values are not thought to represent the full range of intrusion dip values since high dips tend not to be well imaged on seismic data. The values in Figure 18 are, however, indicative of the common ranges of dips exhibited by sills.

■ 6. DISCUSSION

6.1. Relationship of Intrusions to Syn-Rift Structure

Giba et al. (2009) state "the interdependence of activity between individual volcanoes and faults is weak. Volcanic activity does not influence the location and the activity of tectonic normal faults which, in turn, do not exert a strong control on the locus and timing of volcanic activity in the basin." The statement can be justified by considering that the structural influence at the base of the crust, which will influence the location of a pipe, will be different from the shallower level faulting (e.g., Cassidy and Locke, 2010). In addition, Giba et al. (2009, 2013) are focused on the link between Middle Miocene extension that was active at the same time as the volcanism. In this paper the focus is on the effect of Late Cretaceous extensional structures and basin geometries on the volcanic plumbing system. The major Late Cretaceous system normal faults exhibit larger displacements than the Miocene faults, and have given rise to classic half graben and large tilted fault block geometries filled by syn-rift sediments. These sediments are up to ~4 km thick in the depocenter of Fault 1, and ~3 km thick in the depocenter of Fault 2 in the vicinity of the Kora Volcano (Fig. A1.4).
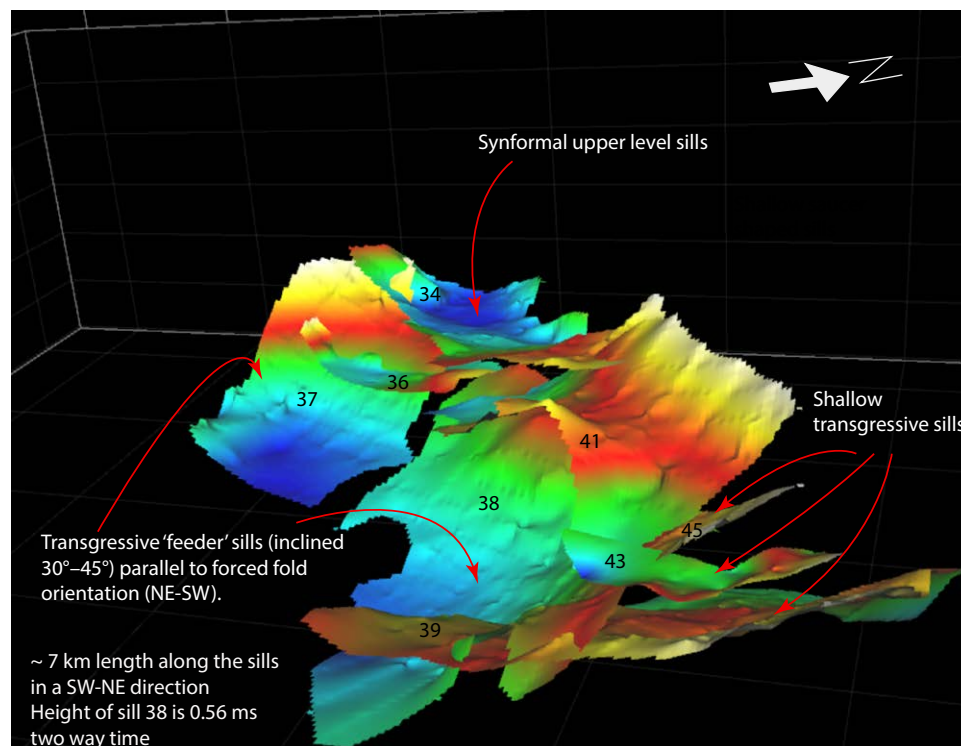
Figure 17. 3-D oblique view to the west of the complex of intrusives in Area 2 at location Y (Fig. 10), in the Kora area, Taranaki Basin, offshore New Zealand. View is along ~7 km length of sills in a NE-SW direction. Numbers correspond with sill numbers in Appendix 2.

The Kora Volcano is focused along the trace of a large normal fault (Fault 2), where it is intersected by NW-SE–trending faults. This is probably no coincidence and represents a rift-related zone of weakness that was exploited by the feeder system, as has been described from the East African Rift (Acocella et al., 2003; Korme et al., 2003).

Once the intrusions reach the syn-rift section they become influenced by several factors: (1) the mechanical contrast between the Cretaceous syn-rift sedimentary rocks and the Permian meta-volcanic basement, (2) the location of depocenters where sills can stack up vertically, (3) the dip of normal faults, and the dip of bedding. These influences can be seen on seismic reflection data. It can also be speculated that source rock layers within the syn-rift section may be preferential sites for intrusion due to their mechanical behavior (Rateau et al., 2014), which is influenced by the presence of organic material (see Morley et al., 2018, for a review of the mechanical properties of shale).

The presence of syn-rift section overlying Permian meta-volcanics represents a clear, sharp boundary where a weak layer overlies a strong layer. Modeling of sill development has shown that such interfaces are favored sites for sill emplacement (e.g., Kavanagh et al., 2006; Barnett and Gudmunsson,
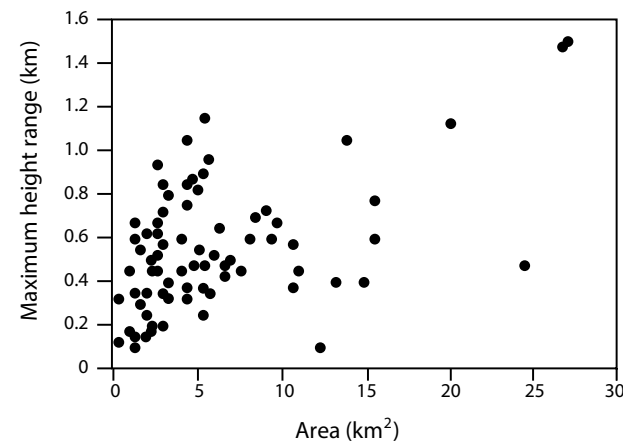

Figure 18. Height versus area plot for sills in Appendix 2, in the Kora area in the Taranaki Basin, offshore New Zealand.

2014). A natural example comes from Norway where there is the extensive occurrence of Upper Carboniferous microsyenite (Mænaite) sills near the base of the Middle Cambrian Alum Shale Formation close to the interface with Precambrian gneisses, in the pre-rift section of the Oslo Graben (e.g., Andersen et al., 2008). This type of intrusion is seen on seismic reflection data in the areas of relatively thin syn-rift stratigraphy associated with tilted fault blocks in areas 3 and 6. They are probably also present at the base of the deep depo-centers, but are not well observed due to energy absorption by the stack of overlying sills, and uncertainty as to whether deep high-amplitude events represent sills, or the high-impedance contrast at the syn-rift/pre-rift contact.

Hansen (2015) modeled sill inclination and determined that in isotropic material transgressive sills climbing 500 m can reach inclinations up to ~34°. It is striking that, except for two higher values (~45°), and a few higher values seen locally on seismic reflection data from unmapped sills, the maximum average inclination for the intrusions (averaged over a distance of at least 500 m) in this study are 35° (Fig. 19), which matches observations from provinces (e.g., Bell and Butcher, 2002; Smallwood and Maresh, 2002; Thomson and Hutton, 2004; Schofield et al., 2012a), and supports the theoretical findings of Hansen (2015). Dips higher than the 35° average value are in part related to sills following faults, and sills following the steeply dipping bedding underneath the volcanic edifice. Note that due to averaging of the dips over a long distance short segments of sills that are steeper than the average dip are not identified. These segments are commonly where sills follow faults over a relatively small area of the sill. While there are clear anisotropies in the section due to bedding and faulting the bedding has not been rotated to very high angles. Faults tend to be relatively low angle dipping between ~35° and 50°. Some sills partially follow the faults, and so locally have dips in the range of 35°–50°. While there
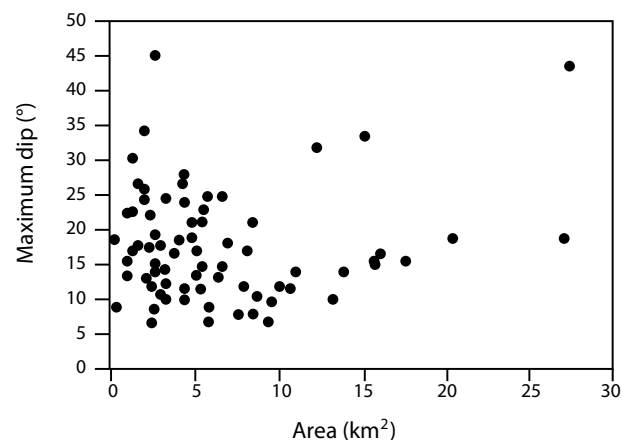

Figure 19. Maximum dip (averaged over 500 m) versus area plot for sills in Appendix 2, in the Kora area in the Taranaki Basin, offshore New Zealand.

probably are dikes present that dip around 90° these are not typically observed on seismic reflection data.

Sills that partially follow the trace of a fault have been described from seismic data (e.g., Magee et al., 2013a, 2013b; Rateau et al., 2014). There are certainly similar effects seen in the data set, however, the circular nature of the intrusive complex means that the steepening of sills observed passing toward the Kora Volcano is a feature of the intrusion and occurs at orientations oblique or even orthogonal to faults as well as parallel to faults. However, some sills have been preferentially aligned to faults (Fig. 16), for example sill 50 (Figs. 11B and A2.3). Some sills crossing narrow fault blocks are transgressive along two faults.

While there is evidence of structural control to some degree on the distribution of intrusions, it is recognized that there are also effects independent of structural control. In the ring of sills that dip away from the volcano there is a mixture of sill trends that follow fault trends or are independent of fault orientations. Other controls on intrusion orientation in intra-arc and back-arc settings can be related to changes in response to variations in stress over long time periods or rapid stress changes related to stress unclamping from large earthquakes (Tibaldi and Bonali, 2017). These authors also note that following dike or sill intrusion, a local stress field perturbation is created that will influence successive intrusions to follow a perpendicular orientation.

6.2. Forced Folds and Intrusions

Igneous intrusions, primarily sills, and laccoliths are known to cause forced folding of the overlying strata (Le Bas, 1971; Pollard and Johnson, 1973; Acocella et al., 2001; Brown and Bell, 2006; Galland, 2012; Galland and Scheibert, 2013; Jackson et al., 2013; Magee et al., 2013b, 2017; van Wyk de Vries et al., 2014). Uplift and subsidence associated with sills has been measured in regions of active volcanism. For example, in the Laguna del Maule volcanic field (Chile), geodetic measurements have detected inflation of sills of similar size and depth (5.2 ± 0.3 km depth, 9.0 ± 0.3 km length, and 5.3 ± 0.4 km width) to those discussed in this paper (Feigl et al., 2013). The maximum vertical velocity of related surface uplift is 280 mm yr^{-1}. During the period of observation from 2004 to 2012 Feigl et al. (2013) estimate the sill inflated by a volume of 0.15 km^3. El Hierro Island (Canary Islands) showed >20 cm uplift, associated with 0.32–0.38 km^3 of magma intruded into sills beneath the volcano from 2012 to 2014 (Benito-Saz et al., 2017). The Taupo Volcanic Zone (New Zealand) provides a proximal example to the Kora Volcano of sill-related subsidence, with rates of around 20 mm yr^{-1}, from a sill-like body at 6 km depth (Hamling et al., 2015). Subsidence is attributed to cooling and contraction of the sill.

Folding by sills typically produces low-relief, broad anticlines (e.g., Hansen and Cartwright, 2006; Jackson et al., 2013; Magee et al., 2013b, 2017), and such anticlines are observed associated with some, but not all, sills around the Kora Volcano (Figs. 20, A1.10–A1.12, and A1.14; Bischoff et al., 2017; Infante-Paez and Marfurt, 2017). Some of the folds are domal, while others are elongate in either N-S or NE-SW directions (Fig. 8).
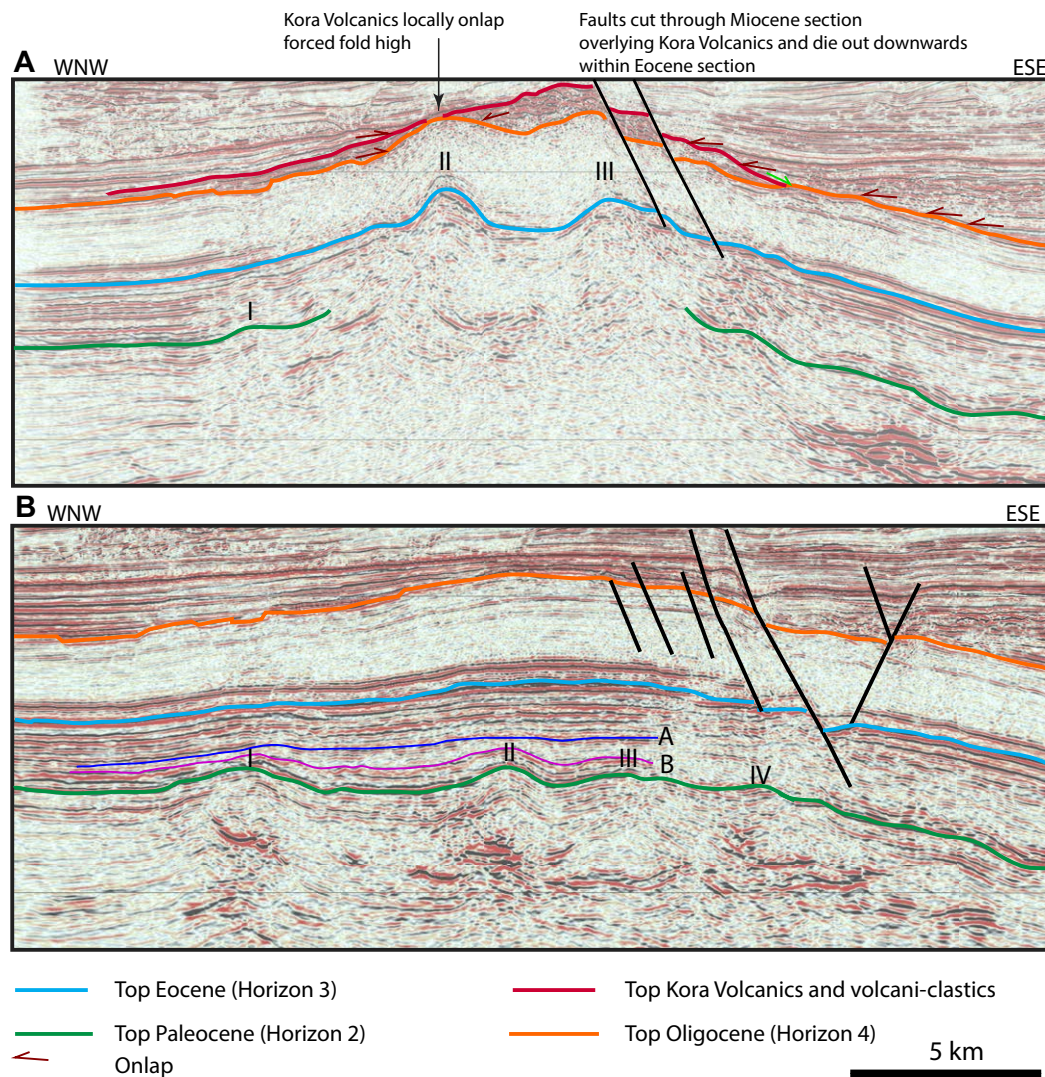
Figure 20. Examples of forced folds by growth of intrusions; see Figure 8 for location. (A) Inline illustrating steep forced folds II and III affecting horizons 3 and 4. (B) Inline illustrating forced folds (I, II, III, IV) that affect Horizon 1, but not Horizon 2. The folds die out between local horizons B and A.

Kora Volcanics locally onlap forced fold high

Faults cut through Miocene section overlying Kora Volcanics and die out downwards within Eocene section

— Top Eocene (Horizon 3)

— Top Paleocene (Horizon 2)

← Onlap

— Top Kora Volcanics and volcani-clastics

— Top Oligocene (Horizon 4)

5 km

In addition to the short wavelength forced folds around the outer regions of the volcano, there is significant uplift and folding directly under the volcano (Figs. 4 and 21) where seismic reflection data shows the Lower Manganui–Tikorangi formations have been steeply rotated in a short wavelength dome-like fold (Fig. 21). It can be argued that near the transition to chaotic data beneath the volcano the steepening of the reflections is at least in part a seismic artifact, for example due to over migration. However, the Kora-1A

Well lies on the edge of the poor data quality zone and has dip meter data in the Paleogene section. The dip meter log for the interval 2950–3250 m shows scattered dip values between 30° and 50° E, with a few short intervals showing fairly consistent values around 45°. Hence the dips from the well appear to approximate those on the seismic data, which point to significant steepening of strata related to forced folding close to the volcano. On smaller satellite vents there are also clear indications of steepening of strata (Fig. 20A).
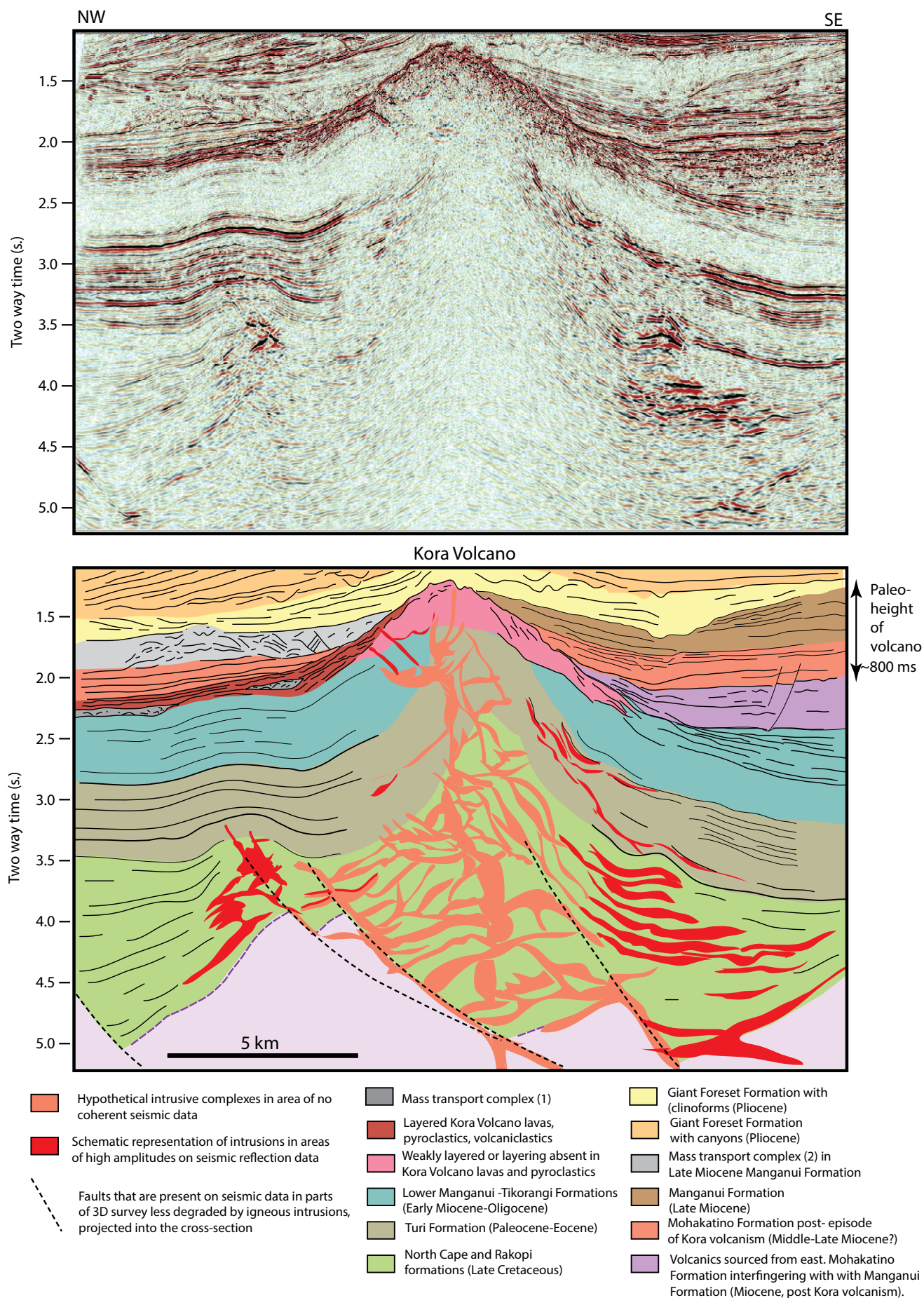
NW   SE

Kora Volcano

Paleo-
height
of
volcano
~800 ms

Hypothetical intrusive complexes in area of no coherent seismic data

Schematic representation of intrusions in areas of high amplitudes on seismic reflection data

Faults that are present on seismic data in parts of 3D survey less degraded by igneous intrusions, projected into the cross-section

Mass transport complex (1)

Layered Kora Volcano lavas, pyroclastics, volcaniclastics

Weakly layered or layering absent in Kora Volcano lavas and pyroclastics

Lower Manganui -Tikorangi Formations (Early Miocene-Oligocene)

Turi Formation (Paleocene-Eocene)

North Cape and Rakopi formations (Late Cretaceous)

Giant Foreset Formation with (clinoforms (Pliocene)

Giant Foreset Formation with canyons (Pliocene)

Mass transport complex (2) in Late Miocene Manganui Formation

Manganui Formation (Late Miocene)

Mohakatino Formation post- episode of Kora volcanism (Middle-Late Miocene?)

Volcanics sourced from east. Mohakatino Formation interfingering with with Manganui Formation (Miocene, post Kora volcanism).

Figure 21. Interpretation of seismic inline 1350 suggesting the style of the poorly imaged region under the Kora Volcano in the Taranaki Basin, offshore New Zealand, is one dominated by sills, that are possibly linked by transgressive sills, short dikes, and possibly a pipe system that is offset a sills (see Fig. A1.12 for uninterpreted line and location).

The short wavelength folds lie on a much broader domal uplift associated with the volcano. Horizon 4 is an intra-Early Miocene horizon that directly underlies the lavas and volcani-clastics of the Kora Volcano. This horizon is deformed in a broad dome ~24 km wide in a NW-SE direction and 19 km wide, and covers an area of ~345 km². The volume of the domal uplift was determined by extrapolating a phantom regional trend to the horizon under the uplift (Fig. 22A), and then subtracting Horizon 4 (Fig. 22B) from the regional trend (Fig. 22C). Toward the SE side of the map the effects of another volcanic trend east of the Kora Volcano impinge on the map (Fig. 22C). The maximum height of the domal uplift is ~1 s TWT, however with depth conversion this uplift becomes complicated by the presence of a relatively thick, high-velocity Kora Volcano section in the middle of the uplift trend, that tapers away from the center. The lateral difference in velocity between the Miocene sedimentary section (~3000 m/s TWT), and the volcanic section (~5000 m/s TWT) is taken into account in calculating the volume of the uplift in Figure 22C, which is ~124 km³.

There is little coherent reflectivity in about a 2.5 km radius of the volcano center, hence the detailed geometry of the volcanic feeder system responsible for the folding is unknown. The relief on the uplifted area of Horizon 4 is ~1125 m. The uplift could, in part, be explained as the consequence of a central feeder pipe shouldering aside the adjacent formations, but it does not seem plausible that a feeder pipe, that typically tend to be tens of meters in diameter (e.g., Bonaccorso and Davis, 1999), would cause such large uplift.

3-D seismic data shows that extensive stacks of sills are present immediately adjacent to the volcano (Bischoff et al., 2017; Figs. 10 and 11). The zone over which the sills occur thickens passing toward the volcano (Fig. 12). It seems clear that the sills preferentially intruded the thick, predominantly fine-grained, probably organic-rich syn-rift section in the hangingwall of Fault 2 in a trend running from north of the Kora Volcano imaged on seismic reflection data (Figs. A1.8–A1.11) and that a similar, but more intense intrusion pattern continues beneath the Kora Volcano as schematically illustrated in Figure 21. The syn-rift section is expected to be mechanically very favorable for sills and laccoliths to develop in (see Section 6.1). Mapping of the syn-rift section adjacent to the volcano and projection of the extensional fault-controlled section beneath the volcano indicates there is a thick syn-rift section beneath the volcano (Figs. A1.8–A1.15). Hence from both the evidence of the syn-rift morphology, and the thickness trends of the sill-affected intervals, permits the proposition that stacks of sills/laccoliths connected by short dikes, transgressive sills, and probably pipes dominate the intrusions style beneath the volcano as schematically illustrated in Figure 21. It is suggested that the syn-rift section stratigraphy favored the development of sills, and inclined transgressive intrusions, over the development of a simple pipe with dikes type of feeder system, as schematically illustrated in Figure 7A.

The volume of erupted material can be estimated from maps made using the 3-D seismic reflection data of the top and base of the Kora volcanic sequence. These indicate an extruded volume of lavas and pyroclastics of ~40 km³. It is much more difficult to estimate the volume of intruded magma imaged on seismic data. The area of mapped sills is 660 km² (Fig. 12), but at least 50% of the sills have not been mapped for a variety of reasons that are mostly related to degradation of seismic data quality, and regions of closely spaced intrusions. Hence the area number is a significant under-estimate. Estimating sill thickness accurately is not possible since there are no well penetrations. The peak to trough distance for many of the intrusions is around 25 ms two way travel time, or around 62.5 m thick. This is a reasonable thickness for seismically imaged sills (e.g., Magee et al., 2015) and in a rift basin setting in Thailand sills seismically imaged, as high-amplitude peak-trough reflections and penetrated by wells, ranged between thicknesses of 20–100 m (Naviset et al., 2017). Only some very broad scoping numbers for the volume of intrusions can be made: The low-side number used for the average thickness of seismically imaged sills is 20 m, while the high-side number is 62.5 m. The low-side number for the area of seismically imaged sills is 660 km², while double that number (1320 km²) is a conservative high-side estimate. The estimates indicate the volume of intruded igneous rocks in the area where intrusions have been mapped is at least 13 km³ and may approach or even exceed 82.5 km³. This estimate range does not take into account the volume of material intruded in the zone of no coherent seismic data below the Kora Volcano and intrusions that are too thin or steeply dipping to be imaged on seismic data.

Another way to estimate the volume of intruded material is from the volume of the domal uplift under the volcano of 124 km³. This is a minimum estimate of the magma volume required to cause the uplift. The estimated volume of intrusions, that are seismically visible, range between 13 km³ and 82.5 km³. While the volume of intrusion versus uplift cannot be precisely accounted and matched, it is at least possible to see from the estimates above that the majority of the uplift volume (124 km³) could be accounted for by intrusions (predominantly sills and laccoliths) within the syn-rift section. However, the presence of a large, probably laccolith-like, magma chamber underlying the syn-rift region can also be suspected in order to provide an additional mechanism for domal uplift, and to store and distribute the magma which fed the overlying intrusions.

While it seems clear that sills and other intrusions cause uplift at a range of scales (Figs. 20 and 22) seismic data shows that for short-wavelength sill-fold relationships uplift is not necessarily directly proportional to sill volume. In Figure A1.14 for example, there is folding seen in layers A–D that decreases in amplitude upwards. Thinning and onlap of the sediments onto the anticlines can be used to determine the timing of intrusion (Hansen and Cartwright, 2006). One interpretation of the decreasing fold amplitude upwards in Figure A1.14 is that it marks a period of fold growth associated with intrusions, with horizon A marking the cessation of folding. This relationship is shown in more detail in Figure 20B. However, the folds terminate within the Paleogene section, while volcanic activity is thought to be associated with the onset of subduction during the Miocene (King and Thrasher, 1996; Giba et al., 2009, 2010; Bischoff et al., 2017). Consequently, either the timing of volcanism in the basin needs to be revised to include a Paleogene phase of igneous activity, or the data is providing evidence that folding dies out upwards because strain is progressively accommodated by mechanisms other than folding visible on 3-D seismic data.
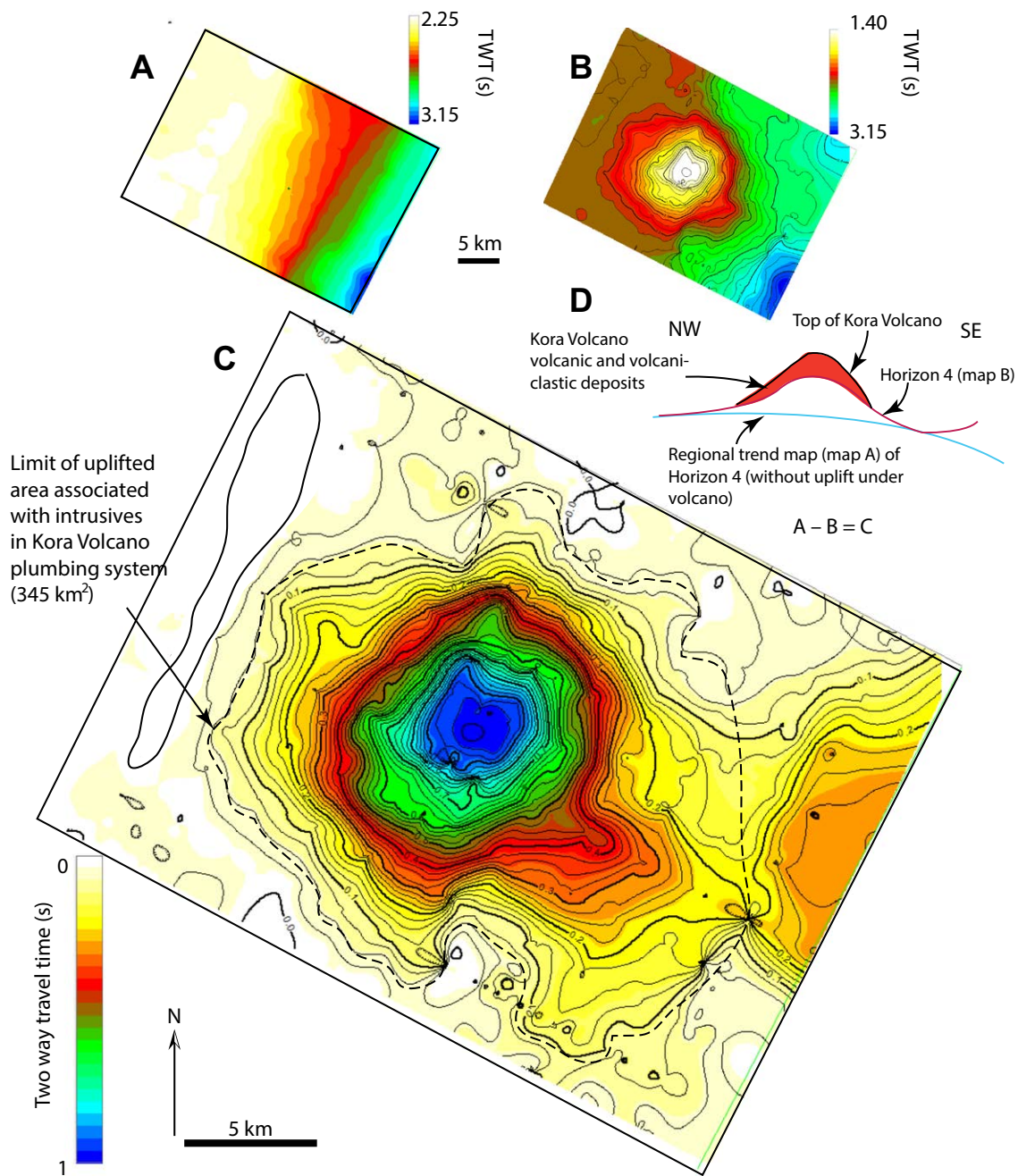
Figure 22. (A) Time-structure regional trend map of Horizon 4 (without uplift related to the Kora Volcano). (B) Time-structure map on Horizon 4. (C) Map of the domal uplift associated with intrusions below the Kora Volcano in the Taranaki Basin, offshore New Zealand (map A minus map B). (D) Schematic illustration of the relationships between the Kora Volcano and the horizons mapped in A and B used to produce map C. TWT—two way travel time.

Figure A1.12 provides an example (forced fold 1) where the amplitude of the fold dies out upwards, with the highest level of folding (4 in Fig. A1.12) occurring at the base of the Kora Volcano extrusive unit. The decrease in amplitude of the fold is shown in the graph in Figure 23, which plots decreasing uplift of the different horizons (1–4) in Figure A1.12, with height. Over a vertical distance of ~2200 m the uplift magnitude decreases from 325 m to 120 m. For forced fold 1 the most likely mechanism to explain the decreasing fold amplitude is differential compaction within the sequence containing layers 1–4. Whether the same mechanism can be applied to layers A–D in Figure 20B, which occurs over a thinner interval is uncertain. There are numerous examples of intrusions where there is no folding, or little folding over intrusions (Fig. A1.14, layers E, F, and G), indicating that not all the volume increase associated with sill emplacement is manifest as short-wavelength folding.

In active volcanic regions large-scale domal uplift beneath a volcano can be related to growth of a magma chamber. For example, investigation of surface uplift in the Central Andes concluded that a long-wavelength surface dome (~1.2 km uplift, 460 km wavelength) associated with the Altiplano-Puna Magma Body has developed as a consequence of buildup of a giant mid-crustal level magma chamber over the last 11 m.y. (Perkins et al., 2016). Similarly, the uplift of Horizon 4 around the Kora Volcano could be related to emplacement of a magma chamber below the sills investigated in this study. The map of thickness changes of the sill affected interval suggests where shallow sill-related uplifts are likely to be the most important, and although the sill interval thickness map generally follows contours of the uplift map in Figure 22B, there are high-frequency differences that suggest the contribution of shallow sills to the uplift is insufficient to impose certain trends (e.g., a NE uplift trend in the north of the volcano, and an uplift trend to the west of the volcano) on the uplift map. Hence it is considered that the surface uplift is partially related to a broad, domed magma chamber that lies at an unknown depth below the Late Cretaceous syn-rift section, and partially related to intrusions within the Late Cretaceous–Paleogene section. Magma rising from this magma chamber has probably used the syn-rift normal faults as well as vertical intrusions as conduits to the shallower section.

The scoping estimates above indicate that a large volume of the magma was intruded (~124 km^3) rather than extruded (~40 km^3). The result was folding and uplift of the sedimentary section at various scales to accommodate the large volume of intrusions present within the syn-rift section (Fig. 21).

Volcanic activity can progress in various ways. For example, emptying of a large magma chamber results in explosive destruction of much of the edifice and extensional collapse of the underlying section and edifice (see review in Tibaldi, 2015). Eruption of the volcano beneath a body of water can result in the development of shallow, broad explosive diatremes, as can the interaction of the volcano with an extensive supply of ground water (phreatomagmatic eruptions, e.g., Lorenz, 1975; Sheridan and Wohletz, 1981; Wohletz, 1986). The early growth of the Kora volcano must have been submarine, given the paleo-water depths of the adjacent formations. In the Kora-1 Well report, paleo-water depths estimated for the Paleogene from microfossils have error bars ranging between 650 m and 2000 m with the preferred depth being ~1200 m, simi-
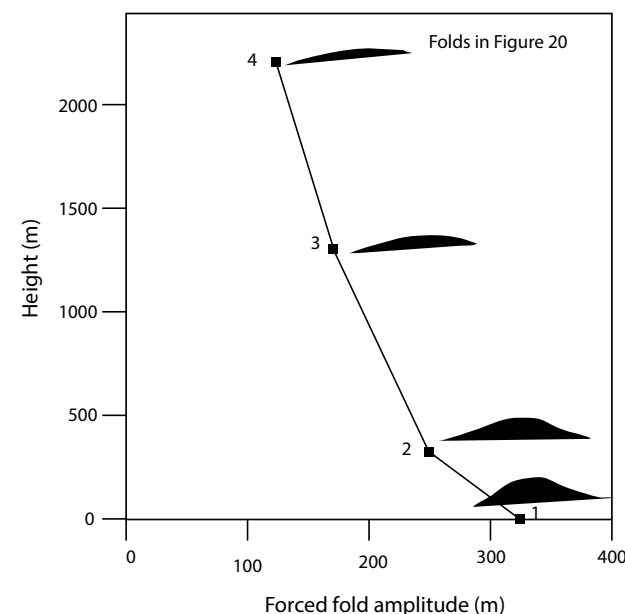

Figure 23. Graph of height in the section versus forced fold amplitude associated with forced fold I in Figure A1.12. 1, 2, 3, and 4 are horizon numbers (see Fig. 4), in the Kora area in the Taranaki Basin, offshore New Zealand.

lar water depths are estimated for Kora-4 (Petroleum Report Series, 1985, 1988). However, growth of the edifice probably resulted in the summit of the volcano becoming subaerial during some of its history, although deposition on the flanks was submarine, as evidenced by the presence of foraminifera within volcani-clastic deposits in Kora-1 (Petroleum Report Series, 1988). The subaerial summit could have developed as a consequence both of the broad domal uplift beneath the volcano, and the construction of the volcanic edifice. Overall the preserved shape of the volcano, the absence of circumferential faults consistent with caldera collapse, and the possible subaerial setting of the summit suggest that there was no highly destructive end to the volcano. The absence of a planar erosive surface to the top of the volcano (indicative of subaerial erosion) is possibly explained by later modification of the volcano by the short eruptive phase at 12 Ma, and the effects of fault offset, and slope instability caused by the late radial faulting.

6.3. Importance of Sills versus Dikes in Volcanic Plumbing Systems

While the proposal that the shallow (upper 6 km) section beneath Kora Volcano is dominated by a network of sills and laccoliths departs from the most common models involving some combinations of magma chambers, dikes and pipes (see Section 3), the proposal is not without precedent. For

example, Marsh (2004) proposed that magmatic mush columns in sill complexes can make important volcanic feeder systems (Fig. 7E). The large sill systems described by Marsh et al. (1997), Marsh (2004), and Muirhead et al. (2012) are in a different tectonic setting from the Kora Volcano, and the sills fed flood basalts not a stratovolcano. However, the presence of extensive layered sill complexes is the most important aspect stressed here, and they occur to greater or lesser degrees in a variety of igneous provinces. Perhaps a closer example is the possible association of classic areas of cone sheets with large laccolith or sill-like intrusions (Burchardt et al., 2013). Numerical modeling of such features suggests the presence of a sill-like magma chamber (Pollard and Johnson, 1973; Galerne et al., 2011). About 12 km of vertical sill to sill ascent was documented by Cartwright and Hansen (2006) from 3-D seismic data, demonstrating that interconnected sill complexes could be the dominant process in vertical magma transport, including feeding extrusive vents.

The dominance of intrusive dike models for igneous systems in active rifts, as described in Section 3, can be argued from a range of perspectives including: (1) the sheeted dike complexes associated with ophiolites; (2) the extensive occurrence of dikes in outcrop in regions like the East African Rift, (3) monitoring of seismicity associated dike intrusion in areas of active rifting, and (4) that dikes best fit the orientation of intrusions expected for an extensional stress field (i.e., where the maximum principal stress is vertical; e.g., Rubin, 1995; Le Corvec et al., 2013). However, most of these observations are made from areas of very advanced crustal thinning in continental rifts, or from areas of seafloor spreading. In the Kenya rift for example, there is a clear switch in structural style from early fault-controlled extension involving half grabens, to a later style involving swarms of relatively low-displacement normal faults, dikes, and extensive volcanism (Mohr, 1987; Morley, 1994). It could be argued that volcanism during the half graben stage of rifting might be more amenable to the development of extensive sill/laccolith complexes as seen in the Kora Volcano, then as these intrusions become more closely spaced the original structural/stratigraphic anisotropy is destroyed, and hence later intrusions start to be dominated by dikes. In this regard it can be noted that the Cenozoic Phitsanulok and Phetchabun rift basins in Thailand, and the Cretaceous–Cenozoic Anza graben in Kenya, are low-extension (beta factor ~1.3–1.5) rifts, where the igneous intrusions exhibit extensive development of sills (Morley et al., 1999; Barr and Cooper, 2013; Naviset et al., 2017).

Perhaps the most unusual aspect of the plumbing system is the combination of doming of the strata beneath the volcano and the intrusion of sills within that dome, which produces a ring of intrusions in plan view (Figs. 21B and 23). Opposite to ring dikes, which tend to dip toward the volcano feeder pipe, the sills predominantly dip away from the core of the volcano, following the general dip of the domed strata (Fig. 23). The term "ring sills" is suggested for these structures.

The Kora Volcano demonstrates how syn-rift structure, and the related thickness variations of the syn-rift section play a role in the geometry and distribution of sills. However, the subduction-related volcano was active during the post-rift stage, and prior to a second phase of extension in the Middle Mio-

cene (Giba et al., 2009). Hence it was not intruded under the same tectonic and stress regime that formed the syn-rift structure. This marks a departure for using the Kora Volcano as an exact analogue for volcanism in a syn-rift setting.

■ 7. CONCLUSIONS

The shallow (>8 km) architecture of intrusions associated with the Kora Volcano are dominated by stacked sill, transgressive sill, and laccolith complexes. Syn-rift structure profoundly affected upper crust intrusion distribution, their stacking patterns, and volcano-feeder intrusive network geometry. Intrusive complexes form an oval shape indicating a point source for the volcano, and a central feeder system at depth (i.e., within the pre-rift section). There is also a strong syn-rift structural/stratigraphic control on the sill distribution, with the thickest sill complexes occurring in the thickest (fault-controlled) syn-rift depocenters, and local N-S elongation of sill complexes following structural trends, particularly north of the volcano. Seismic data shows numerous examples of sills locally following segments of large normal faults, or sill complexes terminating at the normal faults (Figs. A1.9–A1.11). Secondary volcanic (flank) cones have stacked sill complexes beneath them that are focused on faults (Fig. A1.11). Up to 15 km north of the Kora Volcano are found the most laterally extensive sill complexes, which lie close to the base of the syn-rift/top of pre-rift contact. The combination of structural geometry (half graben dip direction) and lithology variations may have been ideal in promoting sill development, but alternatively a deep feeder system may be present in the area. However, the sills do follow the general pattern that the lowest-level sills are the most laterally extensive, and the shallower sills lie closer to the volcano. In Figure 24 it is suggested that the sills are predominantly fed by intrusions following faults that intersect a broad upper crustal magma chamber located within the pre-rift section. The extent of this magma chamber is suggested by the uplift geometry of the Miocene section below the Kora Volcano (Fig. 22).

Individual mapped sills range in area from less than 1 km² to ~27 km². Average dips within individual sills tend to range up to 35° (Fig. 19), although locally higher dips up to 58° are observed (e.g., Fig. A1.5). Some of the high dips are independent of structure at the upper segments of saucer-shaped sills, while others follow steeply inclined bedding or faults.

The strong preference for sill/laccolith stacking in the thick syn-rift section appears to have had four effects. (1) In the upper 7–8 km the volcano is inferred to have been fed by a network of sills linked by short dikes and pipes, not a simple single pipe (Fig. 21). (2) The extensive intrusions resulted in folding/doming of the Paleogene section in several places, most significantly under the central volcano (uplift ~1.1 km; Fig. 21). (3) In the absence of a simple volcano plumbing system (e.g., pipe connected to a magma chamber) it appears that much of the magma was stored in intrusive complexes within the syn-rift section, instead of being erupted. (4) The partial subaerial emergence of the Kora Volcano and the extensive accumulation of magma in relatively thin, sill complexes (that could cool relatively rapidly and solidify) avoided a cata-
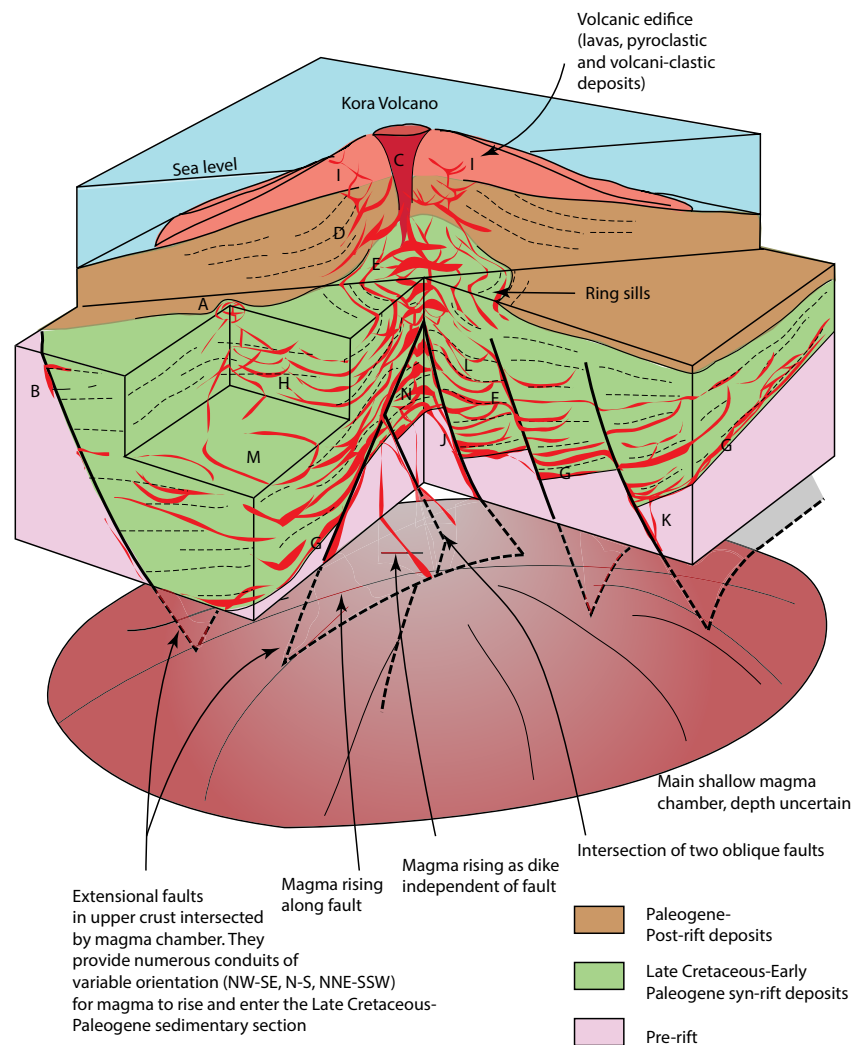
Figure 24. Schematic block diagram illustrating the key features of the Kora Volcano, in the Taranaki Basin, offshore New Zealand, plumbing system and the influence of the syn-rift stratigraphy and faults on intrusion geometry and distribution. A—intrusions causing forced fold; B—intrusions along boundary fault curving into sills in the basin. C—main volcanic pipe, possibly diatreme due to interaction with sea water. May pass into more diffuse sill and dike complexes at depth. D—ring sills intruding forced fold around core of the volcano; E—complex of sills at depth forming feeder system to the volcano; F—sills within syn-rift depocentre; G—sills tend to build up extensively along the syn-rift-pre-rift unconformity; H—sills stack up in particular localities, location H lies between two such stacks where the sills tend to curve upward; I—high level sill and feeder dike complexes that lead to secondary volcanic cones; J—intrusions along fault planes feeding magma from the magma chamber to sill complexes within the syn-rift section; K—feeder intrusions along fault planes to location G sills; L—sills curving upward following fault propagation fold-related dips in upper part of syn-rift section; M—saucer-shaped sill; N—laccolith-type intrusions in core of volcano feeder system.

strophic end to the volcanic edifice that typically is the result of interaction with large volumes of water or caldera collapse.

From this study it is suggested that sills in the upper crust can dominate the early-stage history of intrusions within the syn-rift section. However, as the increasing volume of intrusions destroys the syn-rift anisotropies related to faulting and stratigraphic mechanical contrasts, dikes are likely to become the dominant mode of intrusion later in the history of rifting. As documented, for example, in the East African Rift.

APPENDIX 1

Figure A1.1. Crossline 940. (A) Uninterpreted line. (B) Interpreted line. For Figures A1.1–A1.15 the legend is as follows: Purple horizon (1)—base Late Cretaceous syn-rift section, Green horizon (2)—top syn-rift (Late Cretaceous–Paleogene), and Blue horizon (3)—top Eocene. Red—intrusives. Light red—possible intrusive geometries in areas of low data quality. Dashed purple line—extrapolated trend of basement from areas of higher data quality into low data quality areas. For Figures A1.1–A1.15, the location is the Kora area in the Taranaki Basin, offshore New Zealand.
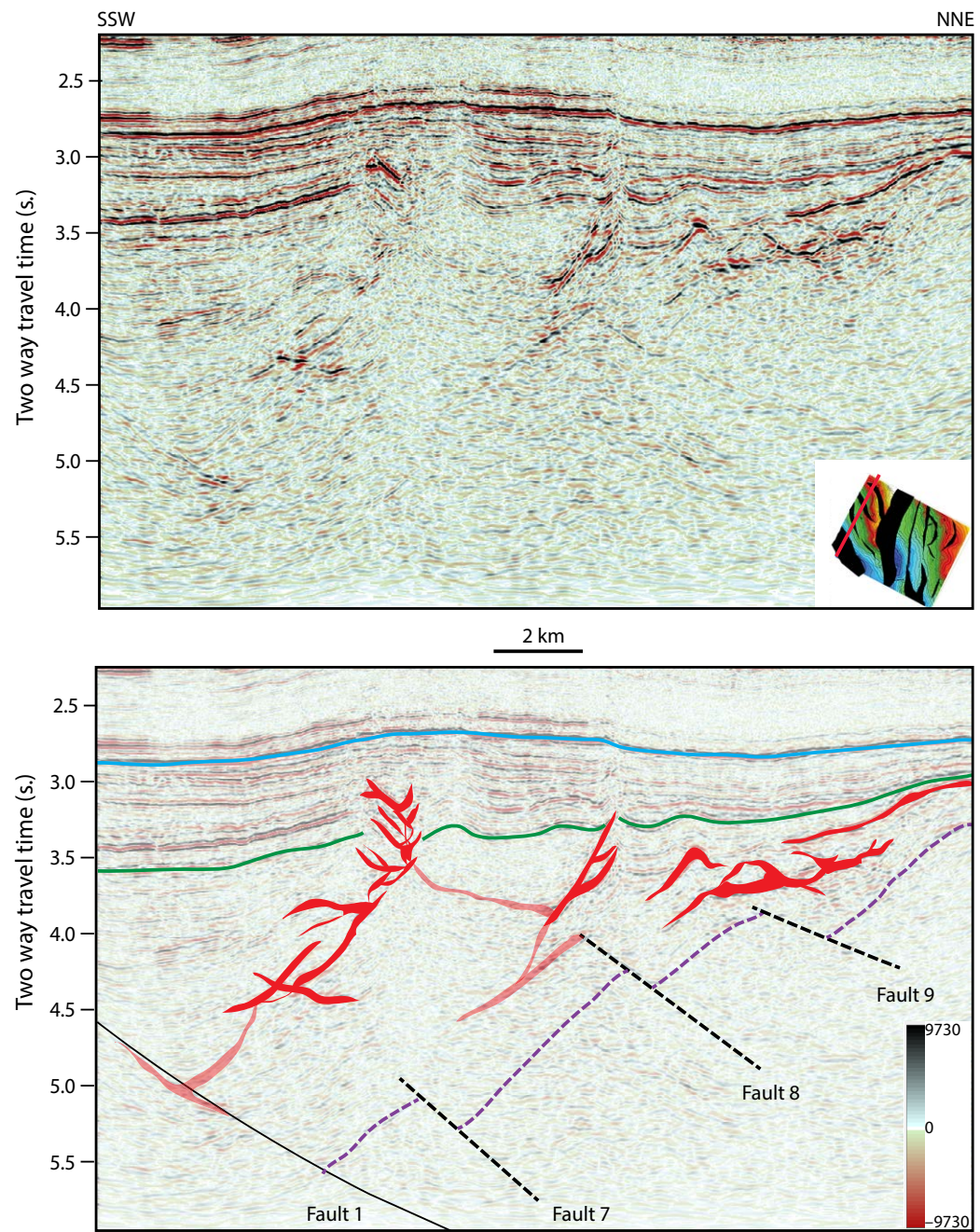
Figure A1.2. Crossline 1220. (A) Uninterpreted line. (B) Interpreted line. For legend and location, see Fig. A1.1.
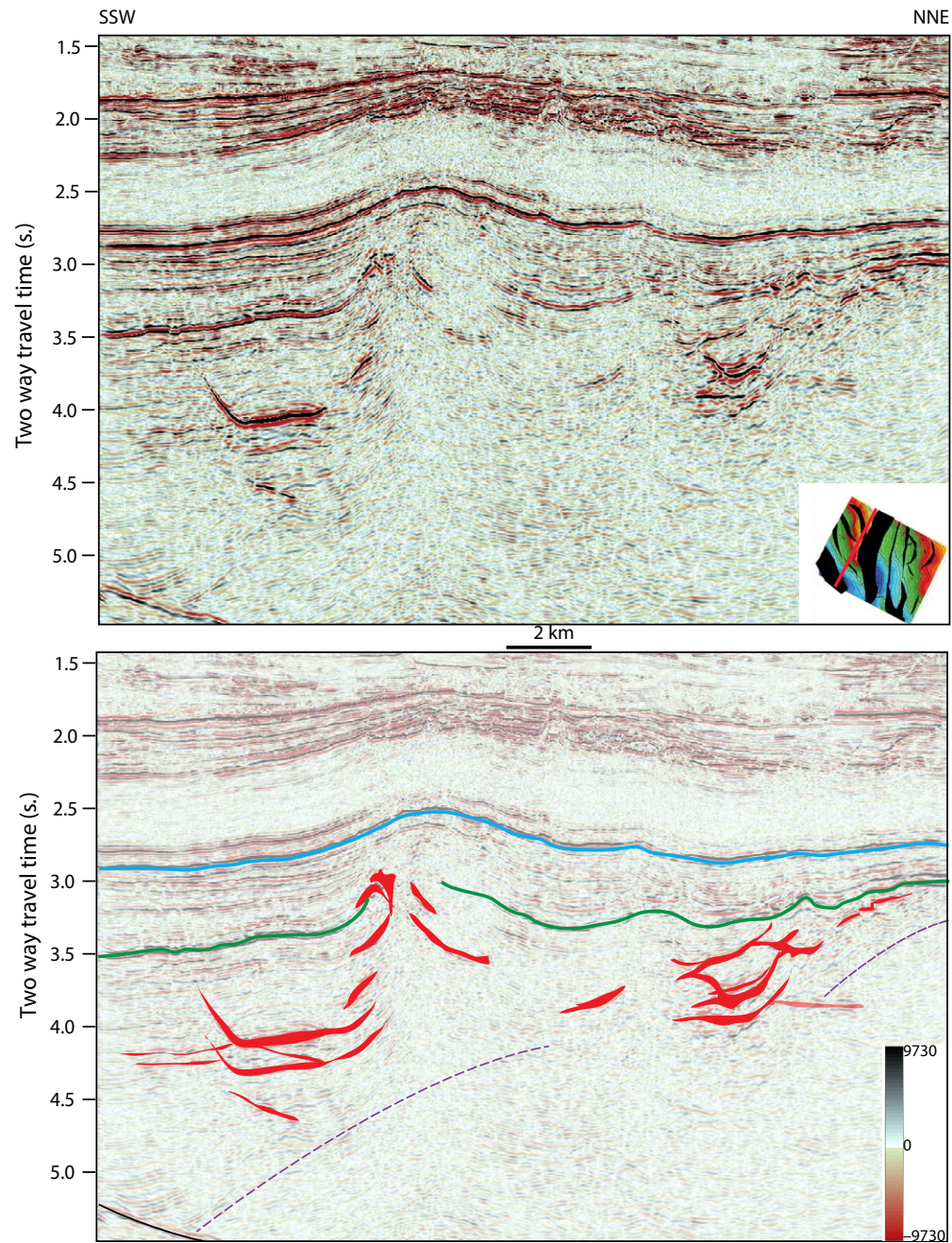
Figure A1.3. Crossline 1350. (A) Uninterpreted line. (B) Interpreted line. For legend and location, see Fig. A1.1.
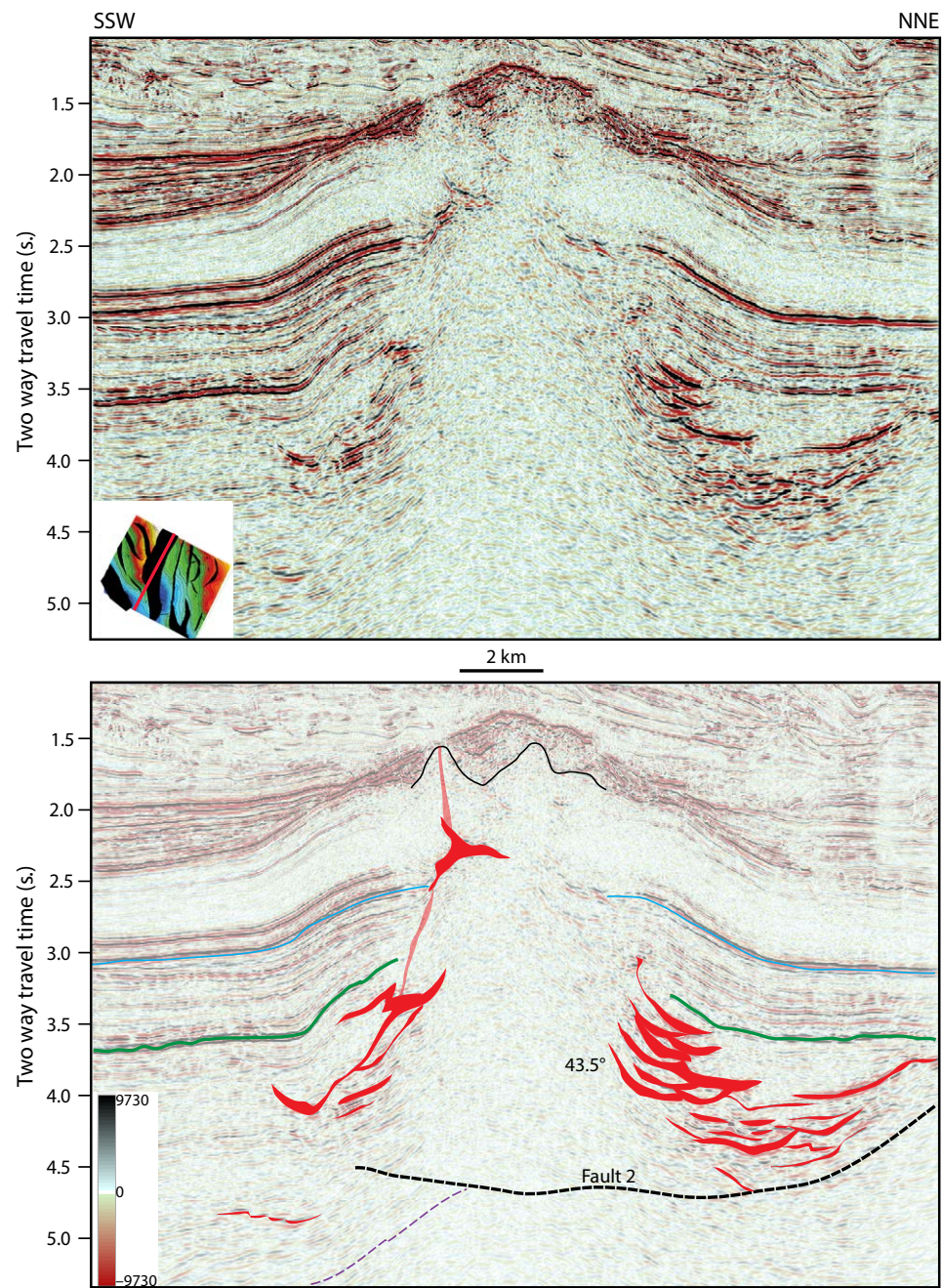
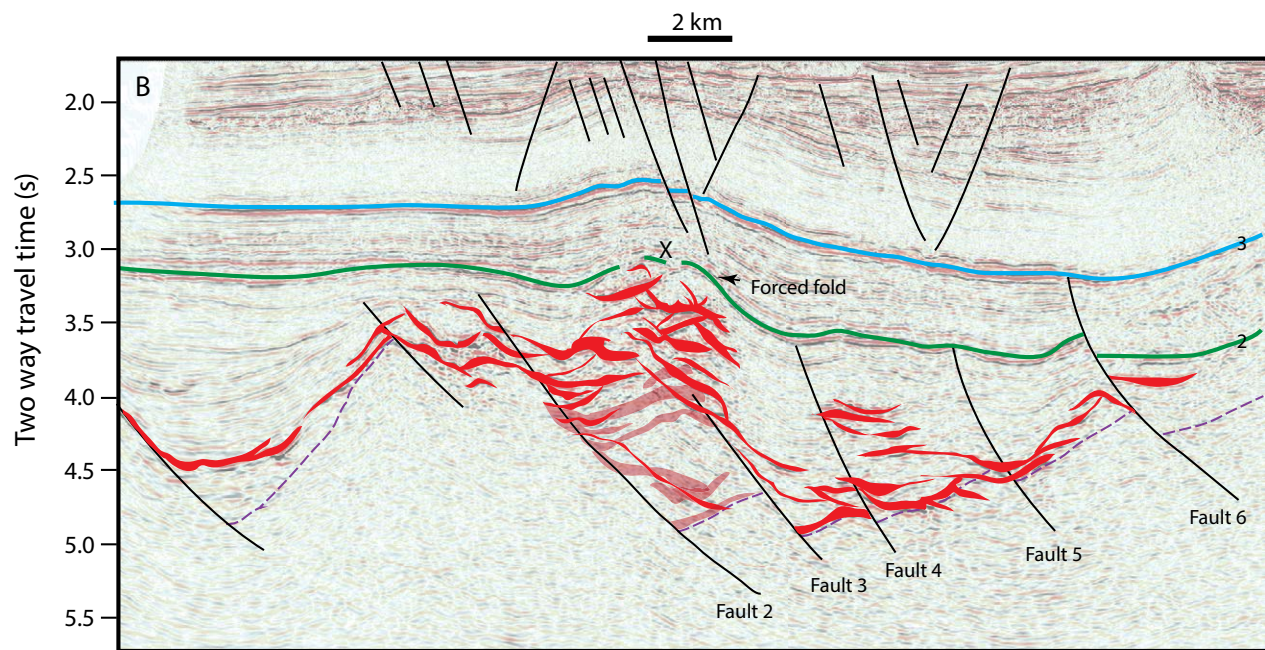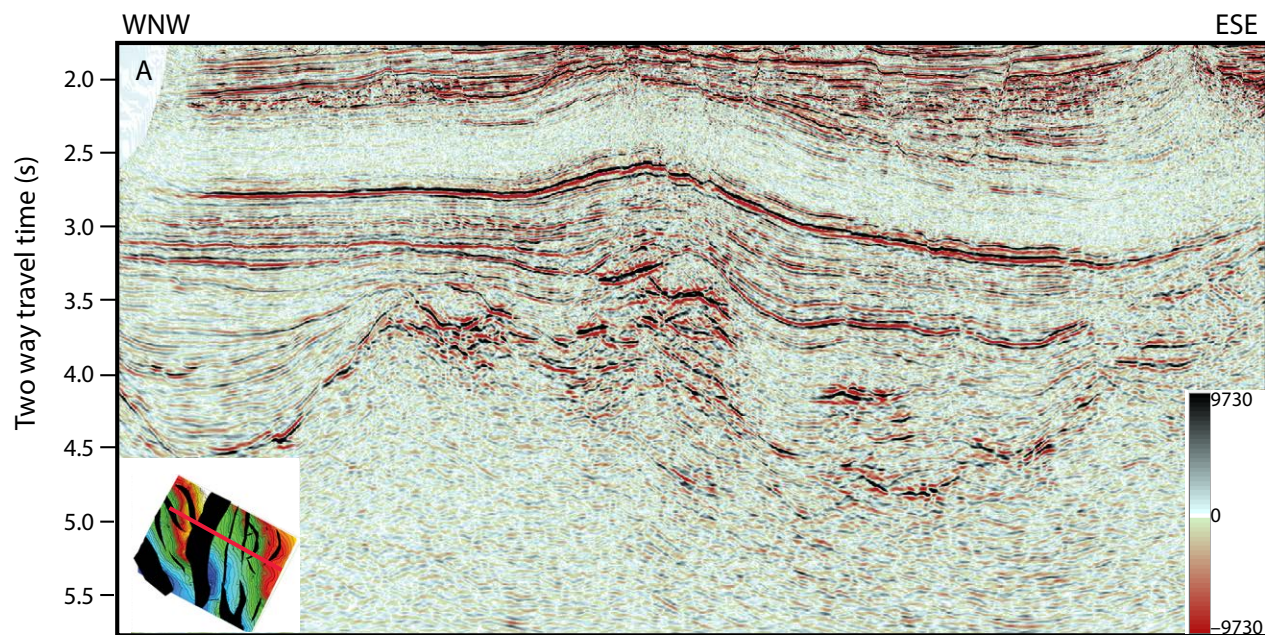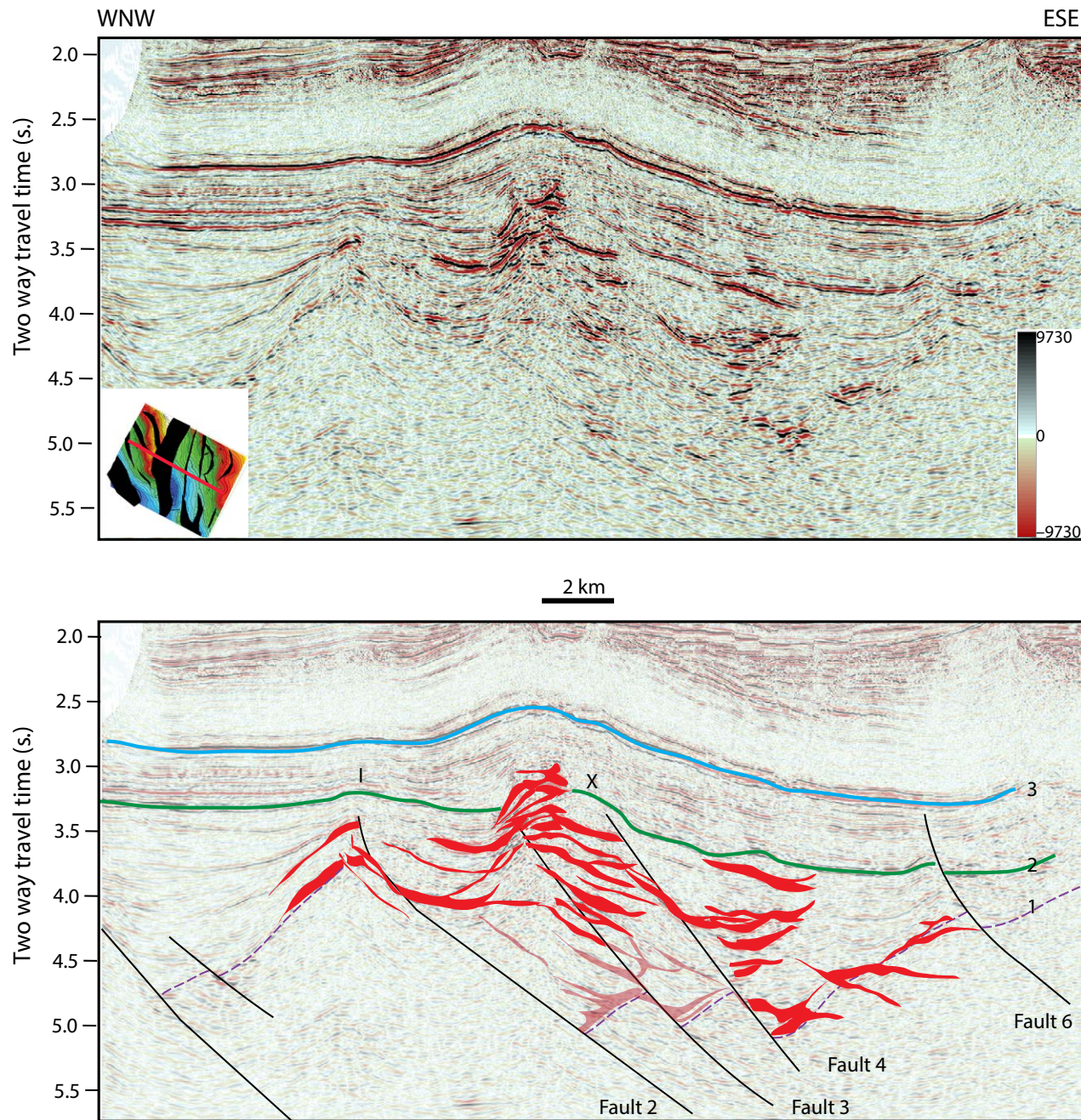Figure A1.4. Crossline 1620. (A) Uninterpreted line. (B) Interpreted line. For legend and location, see Fig. A1.1. 43.5°—dip of inclined sills.
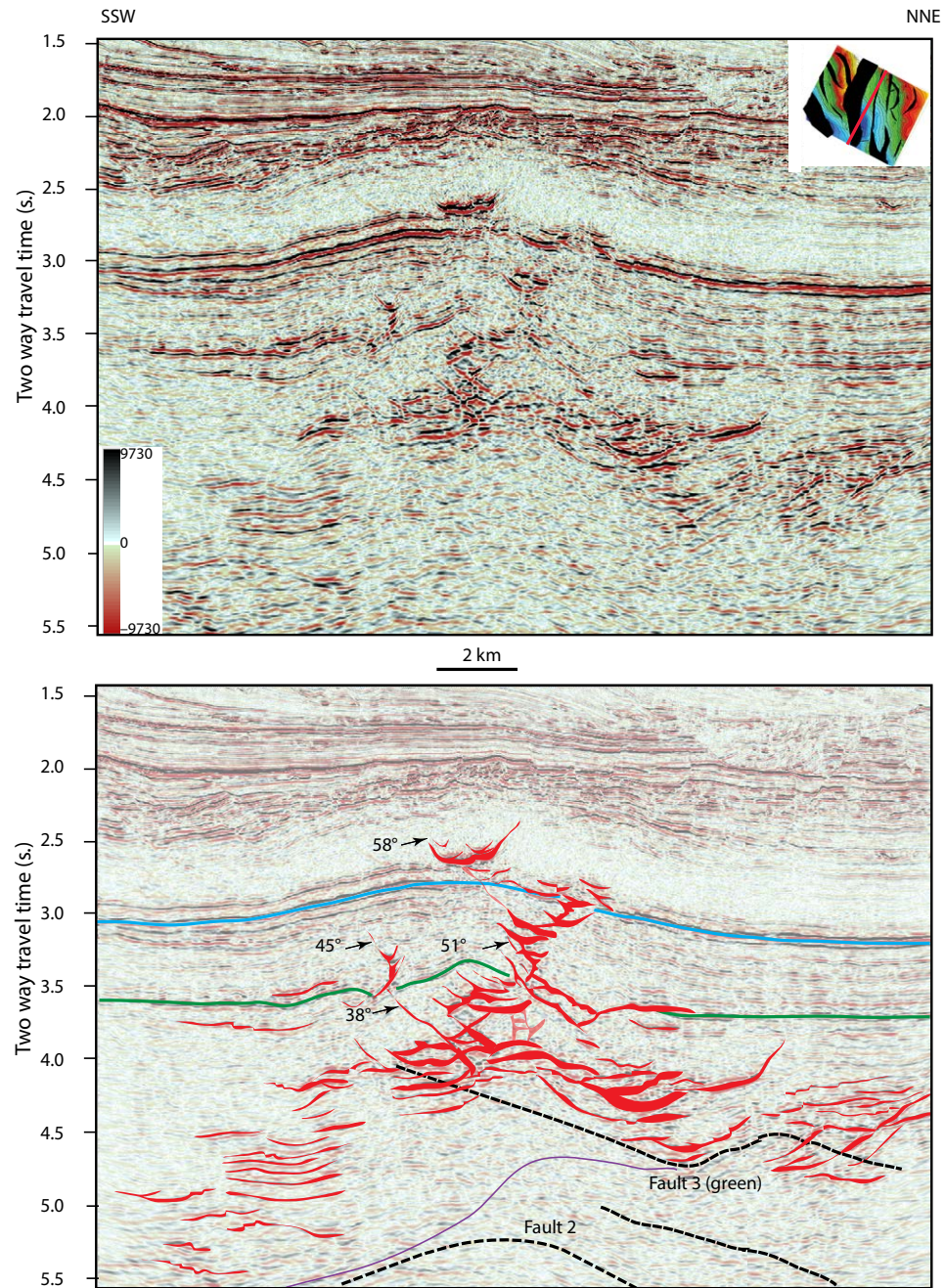
Figure A1.5. Crossline 2200. (A) Uninterpreted line. (B) Interpreted line. For legend and location, see Fig. A1.1. 38°, 45°, 51°, and 58°—dips of transgressive sill segments.
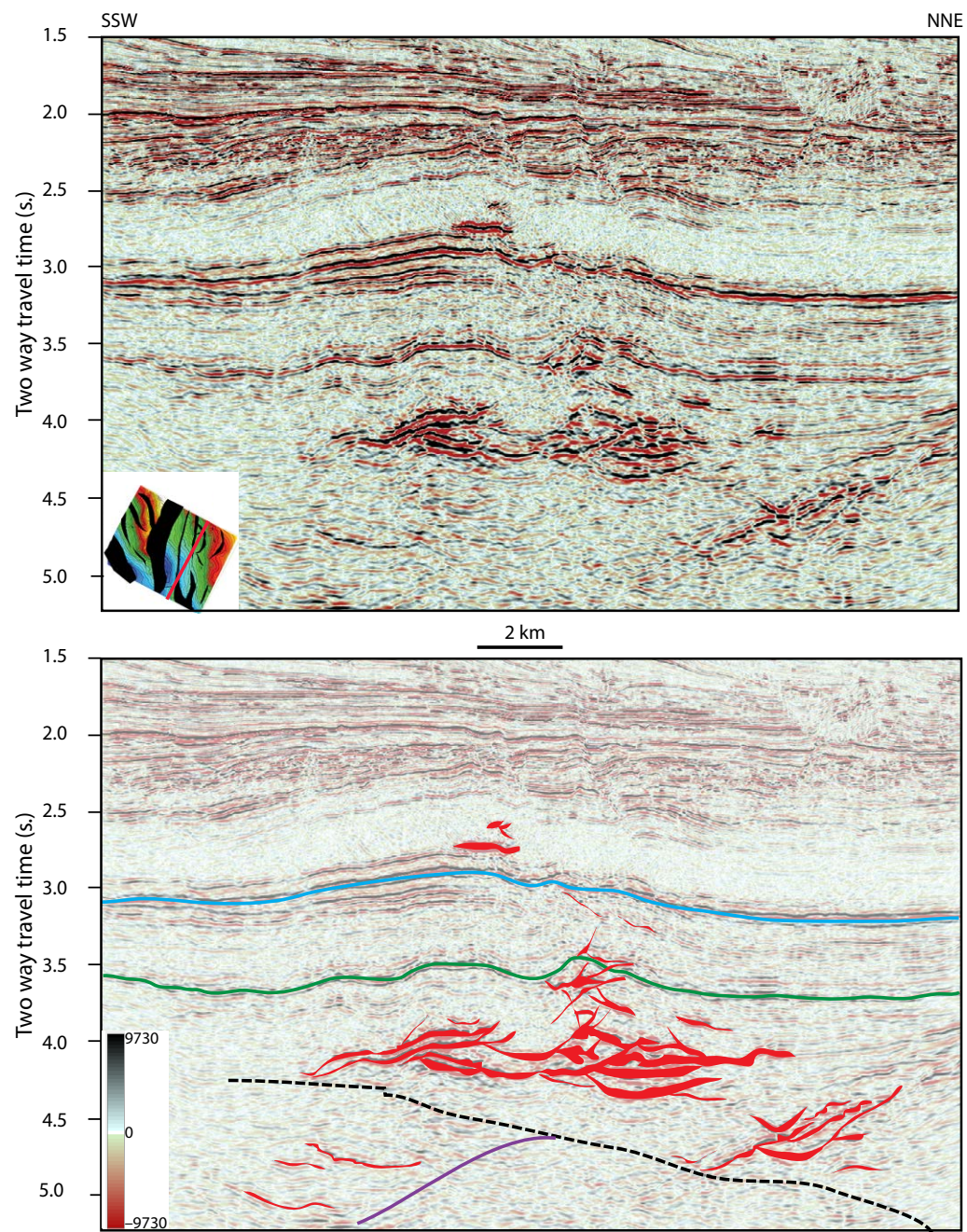
Figure A1.6. Crossline 2290. (A) Uninterpreted line. (B) Interpreted line. For legend and location, see Fig. A1.1.

A SSW   NNE
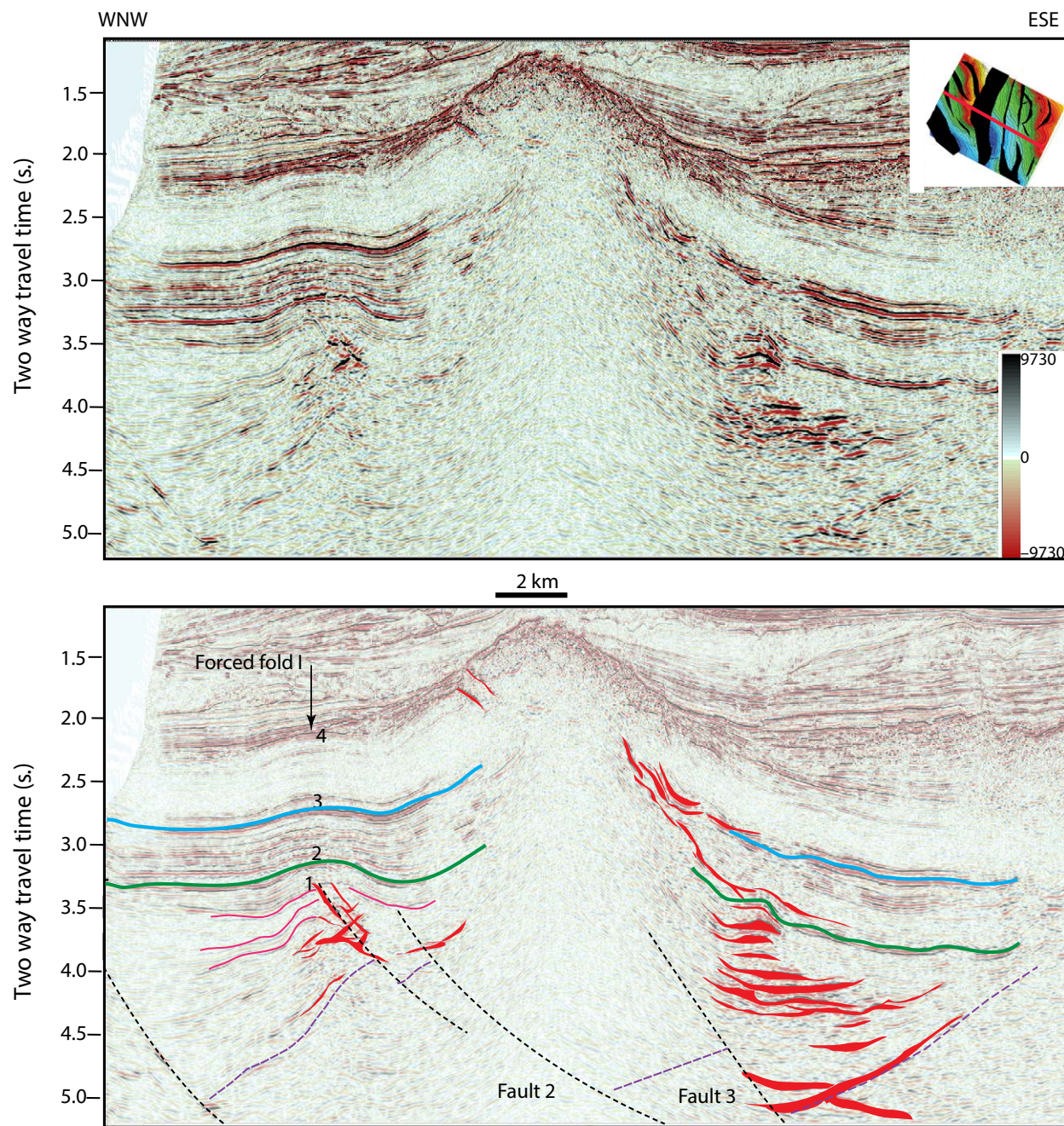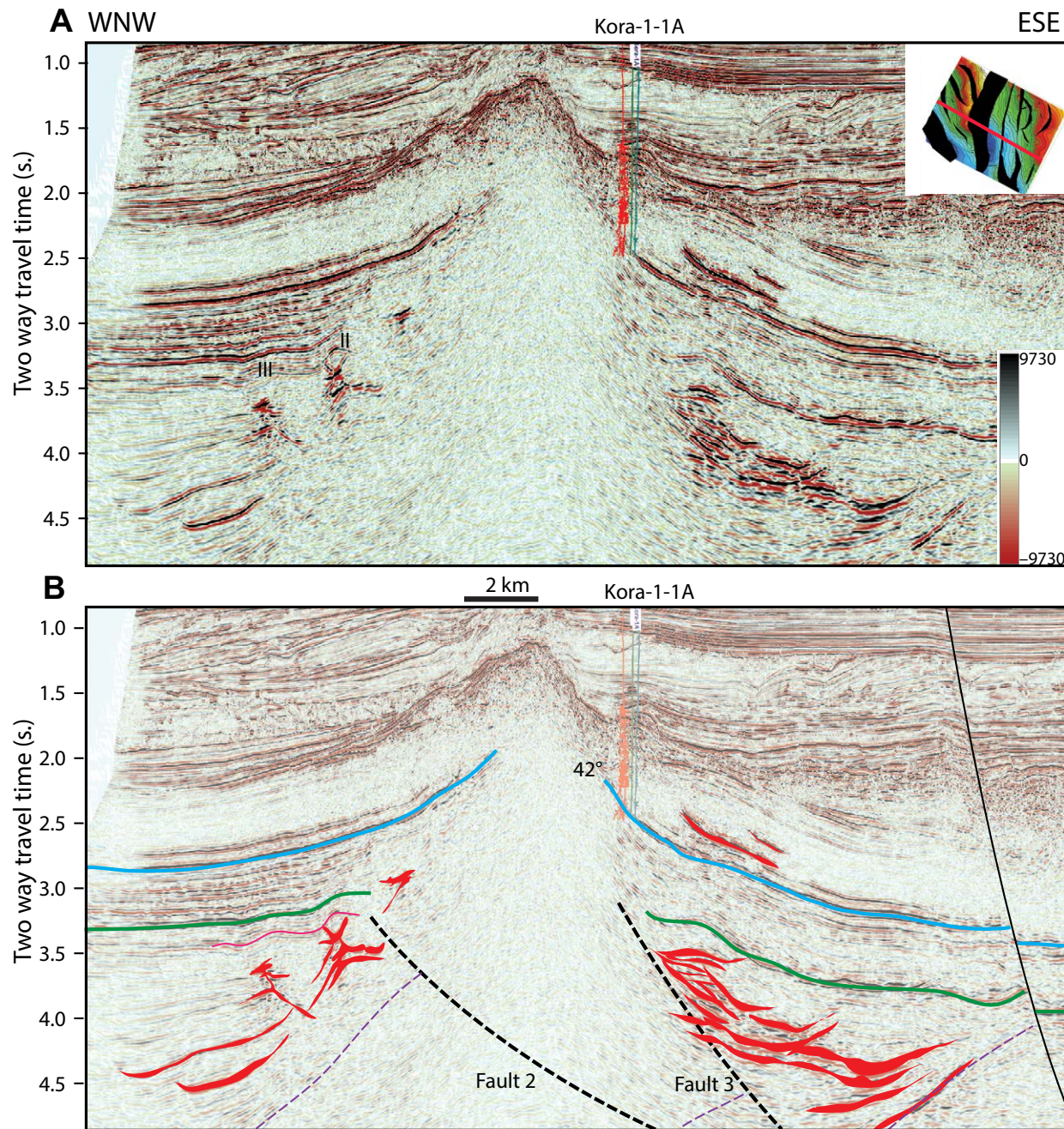
B

2 km
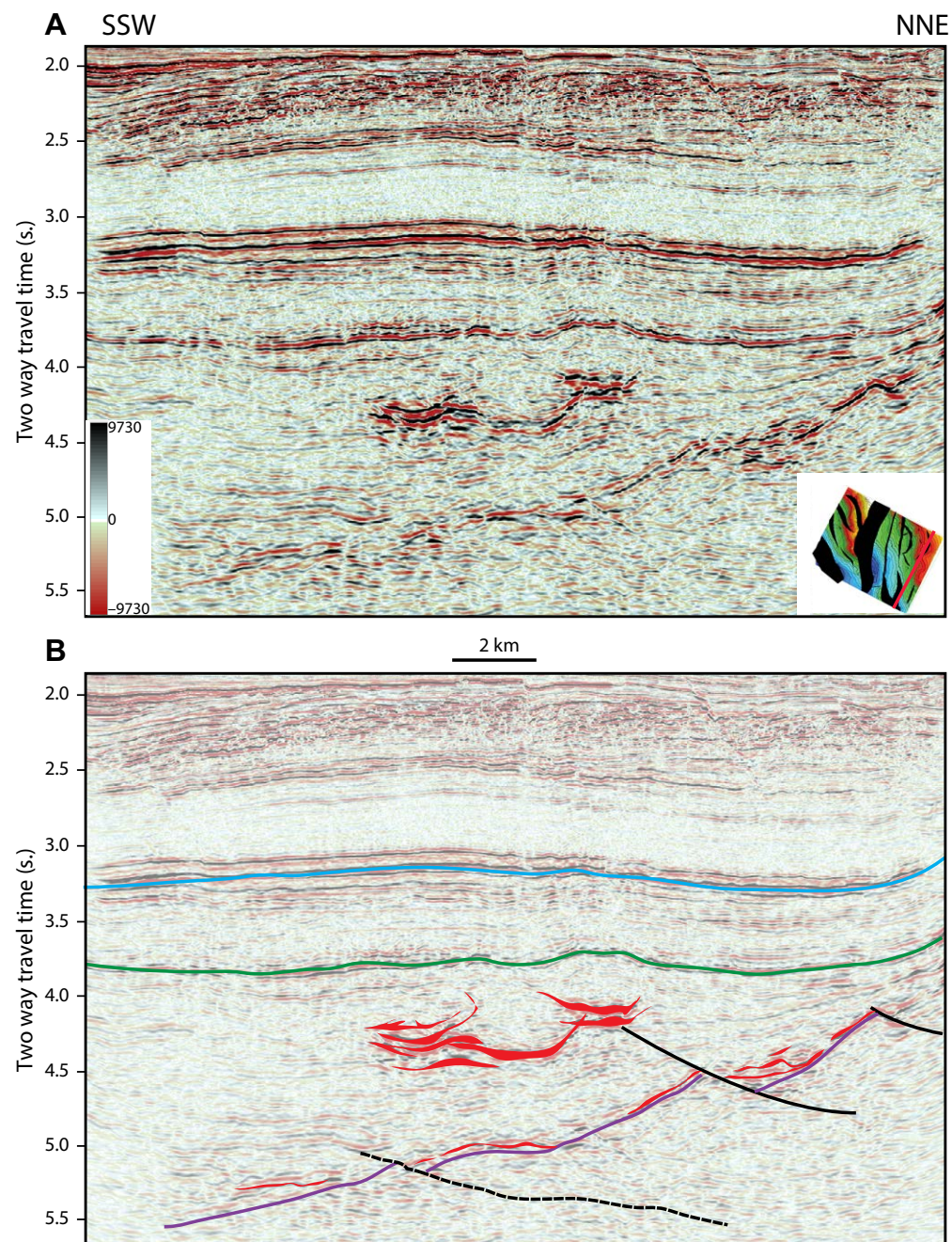
Figure A1.7. Crossline 2490. (A) Uninter-
preted line. (B) Interpreted line. For legend
and location, see Fig. A1.1.
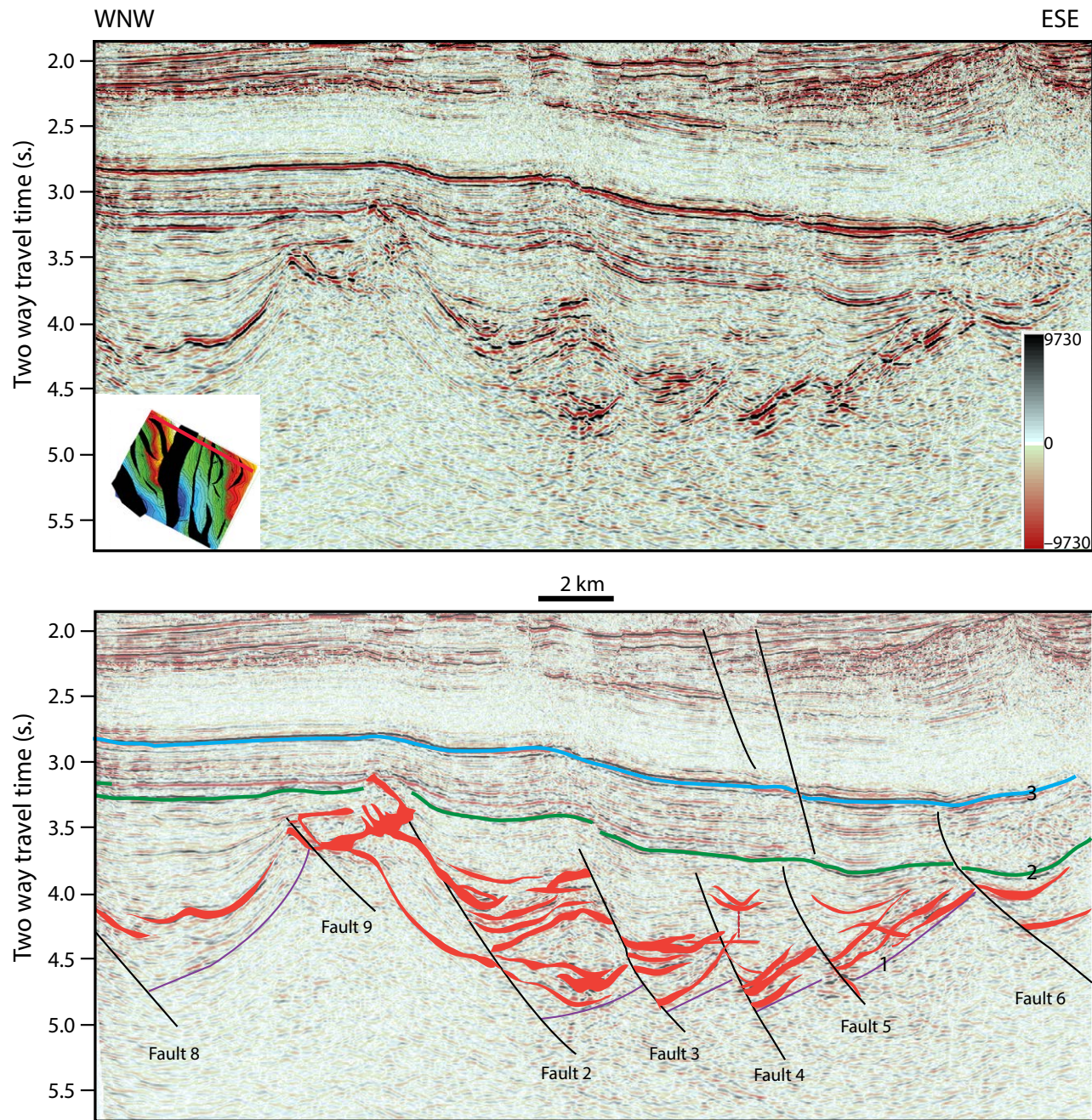
Figure A1.8. Line 1570. (A) Uninterpreted line. (B) Interpreted line. For legend and location, see Fig. A1.1.
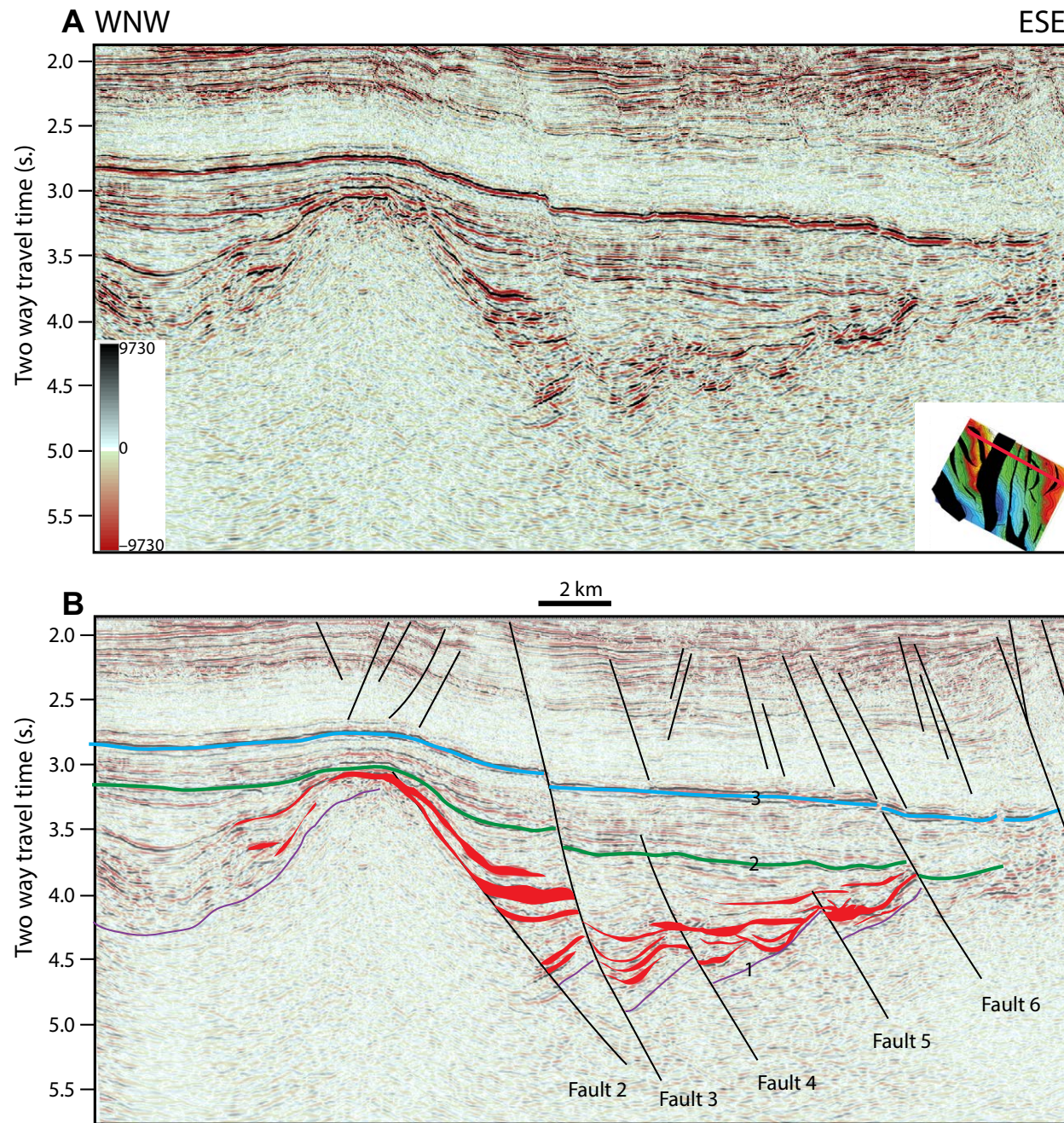
Figure A1.9. Line 1690. (A) Uninterpreted line. (B) Interpreted line. For legend and location, see Fig. A1.1.

Morley | Plumbing system of Kora Volcano
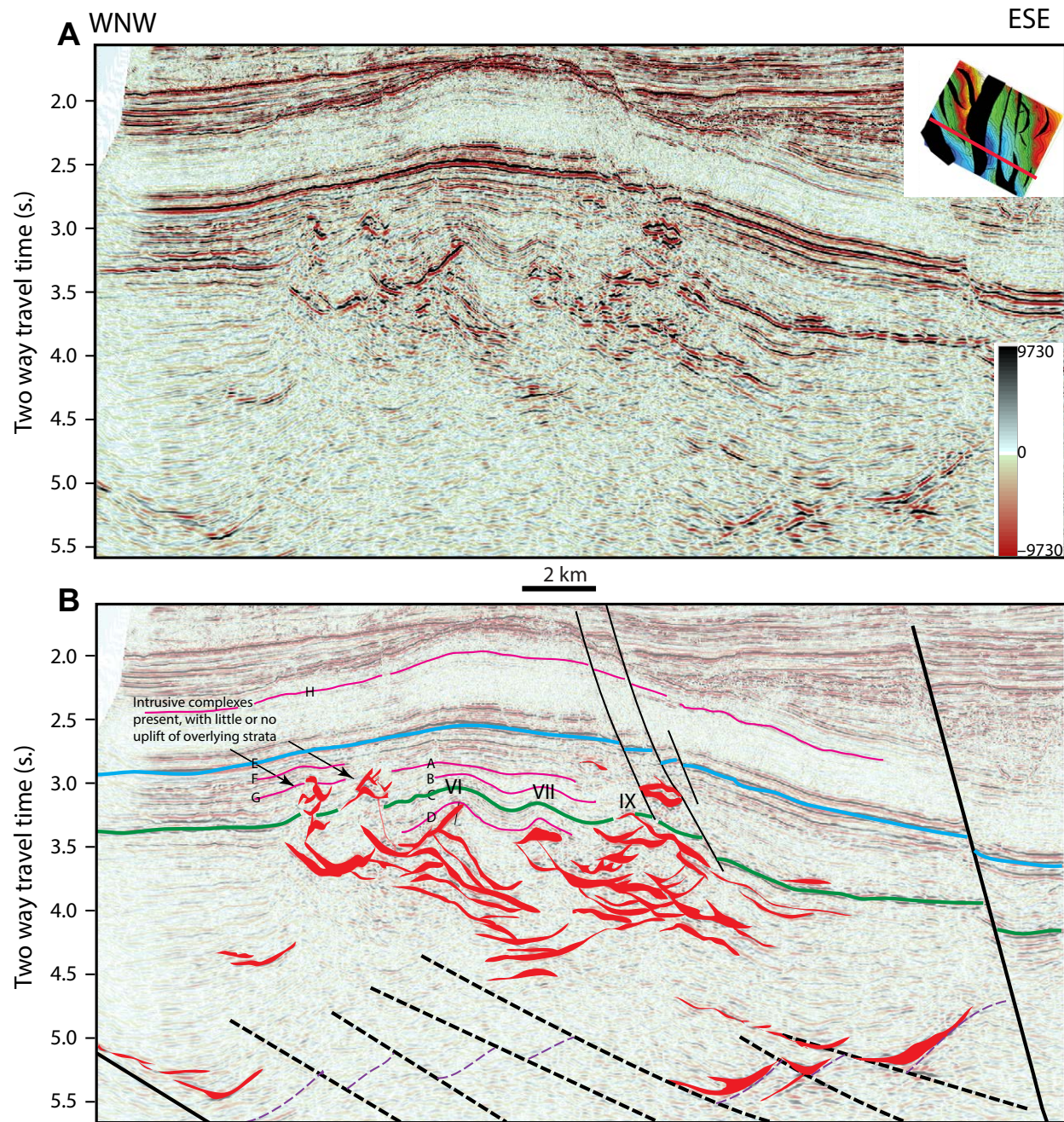
Figure A1.10. Line 1510. (A) Uninterpreted line. (B) Interpreted line. For legend and location, see Fig. A1.1. X—forced fold above intrusions.
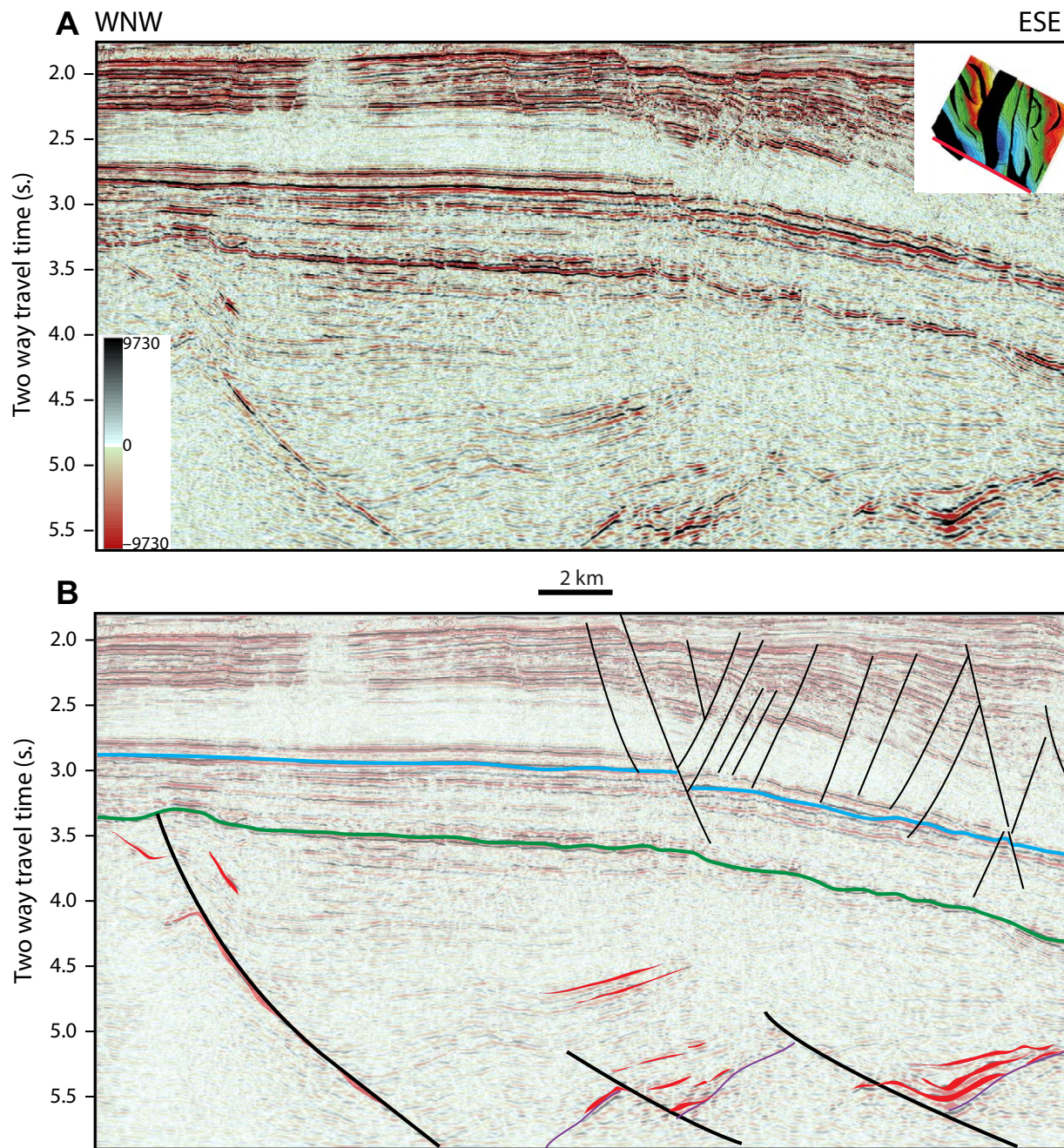
Figure A1.11. Line 1471. (A) Uninterpreted line. (B) Interpreted line. For legend and location, see Fig. A1.1. I and X are forced folds above intrusions.

Figure A1.12. Line 1350. (A) Uninterpreted line. (B) Interpreted line. For legend and location, see Fig. A1.1.

Morley | Plumbing system of Kora Volcano

Figure A1.13. Line 1250. (A) Uninterpreted line. (B) Interpreted line. For legend and location, see Fig. A1.1. 42°—dip of Eocene beds in Kora 1-1A Well.

Figure A1.14. Line 1130. (A) Uninterpreted line. (B) Interpreted line. For legend and location, see Fig. A1.1. A–H—local layers showing forced folds VI, VII, and IX.

Figure A1.15. Line 940. (A) Uninterpreted line. (B) Interpreted line. For legend and location, see Fig. A1.1.
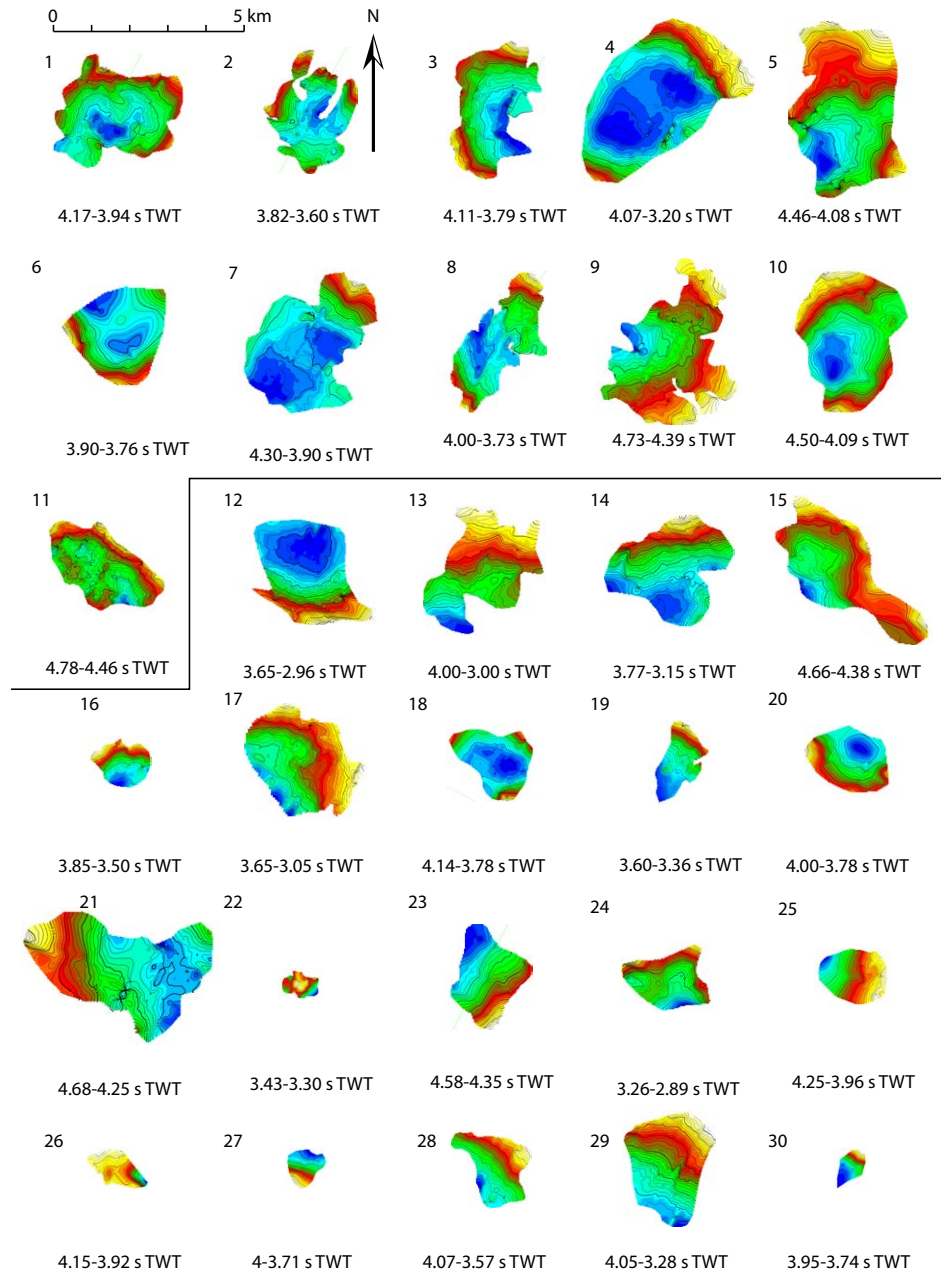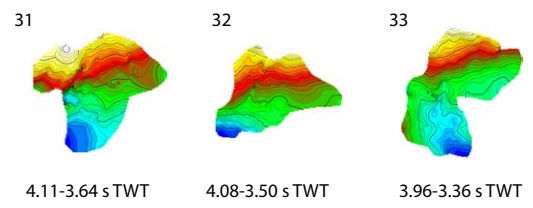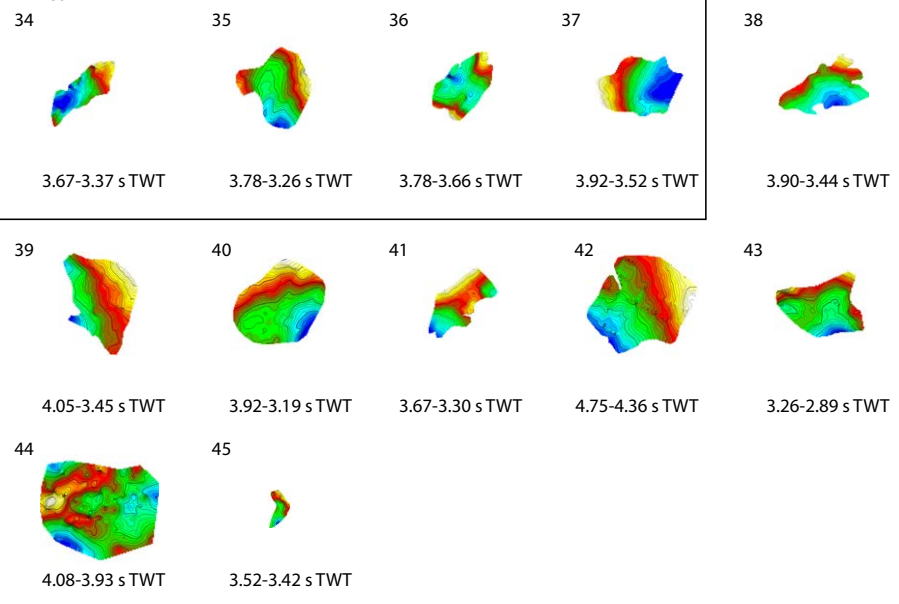
APPENDIX 2

Figure A2.1. Thumbnail maps of sills from Area 1 (see Fig. 10 for location of areas). Colors have different time-depth ranges in each map, blue—relatively deep, yellow—relatively shallow. Absolute time-depth ranges in seconds two way travel time (s TWT) are provided below each map. The line separates saucer-shaped sills (1–11) from other morphologies (12–30).
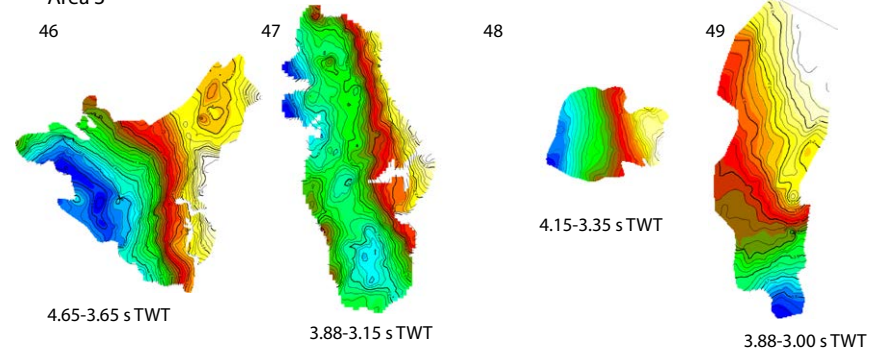
Area 1 continued

Figure A2.2. Thumbnail maps of sills from Area 1 (31–33), Area 2 (34–45), and Area 3 (46–49) (see Fig. 10 for location of areas). Colors have different time-depth ranges in each map, blue—relatively deep, yellow—relatively shallow. Absolute time-depth ranges in seconds two way travel time (s TWT) are provided below each map. The single line separates saucer-shaped sills (34–37) from other morphologies (38–45). Double lines separate sills from different areas.
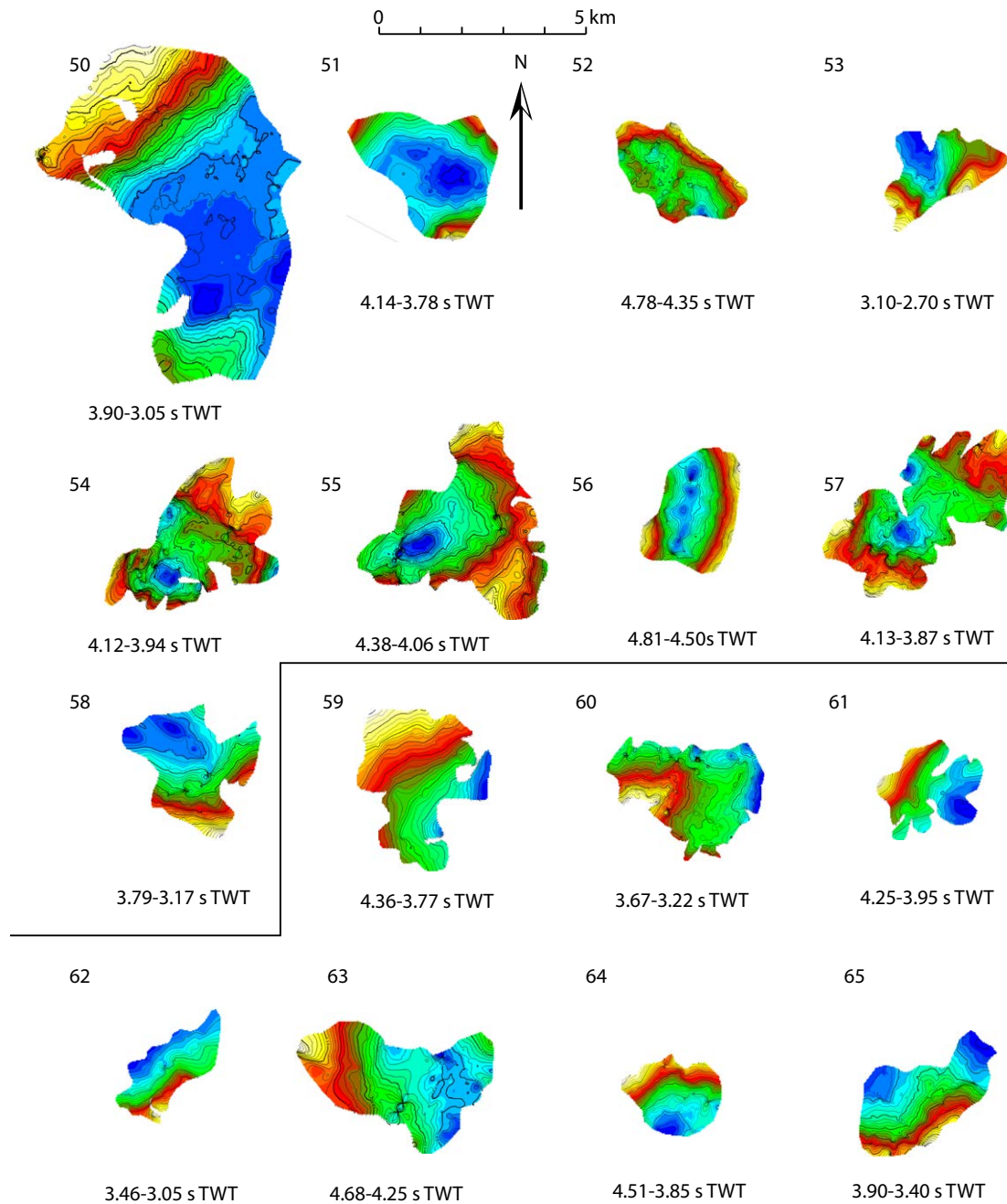
Figure A2.3. Thumbnail maps of sills from Area 4 (see Fig. 10 for location of areas). Colors have different time-depth ranges in each map, blue—relatively deep, yellow—relatively shallow. Absolute time-depth ranges in seconds two way travel time (s TWT) are provided below each map. The line separates saucer-shaped sills (50–58) from other morphologies (59–65).
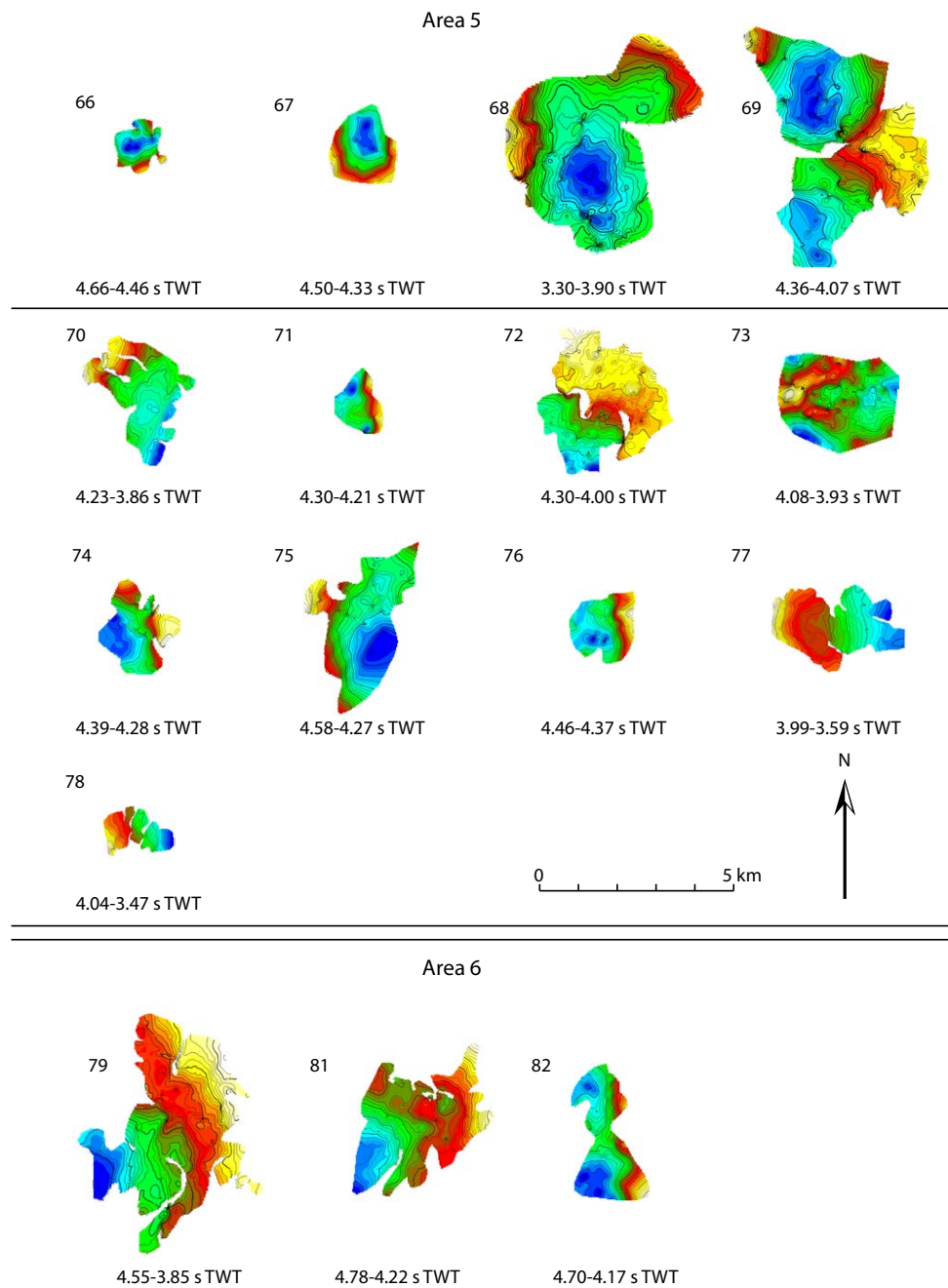
Area 5

Figure A2.4. Thumbnail maps of sills from Area 5 (66–78) and Area 6 (79–82) (see Fig. 10 for location of areas). Colors have different time-depth ranges in each map, blue—relatively deep, yellow—relatively shallow. Absolute time-depth ranges in seconds two way travel time (s TWT) are provided below each map. The single line separates saucer-shaped sills (66–69) from other morphologies (70–78). Double lines separate sills from different areas.
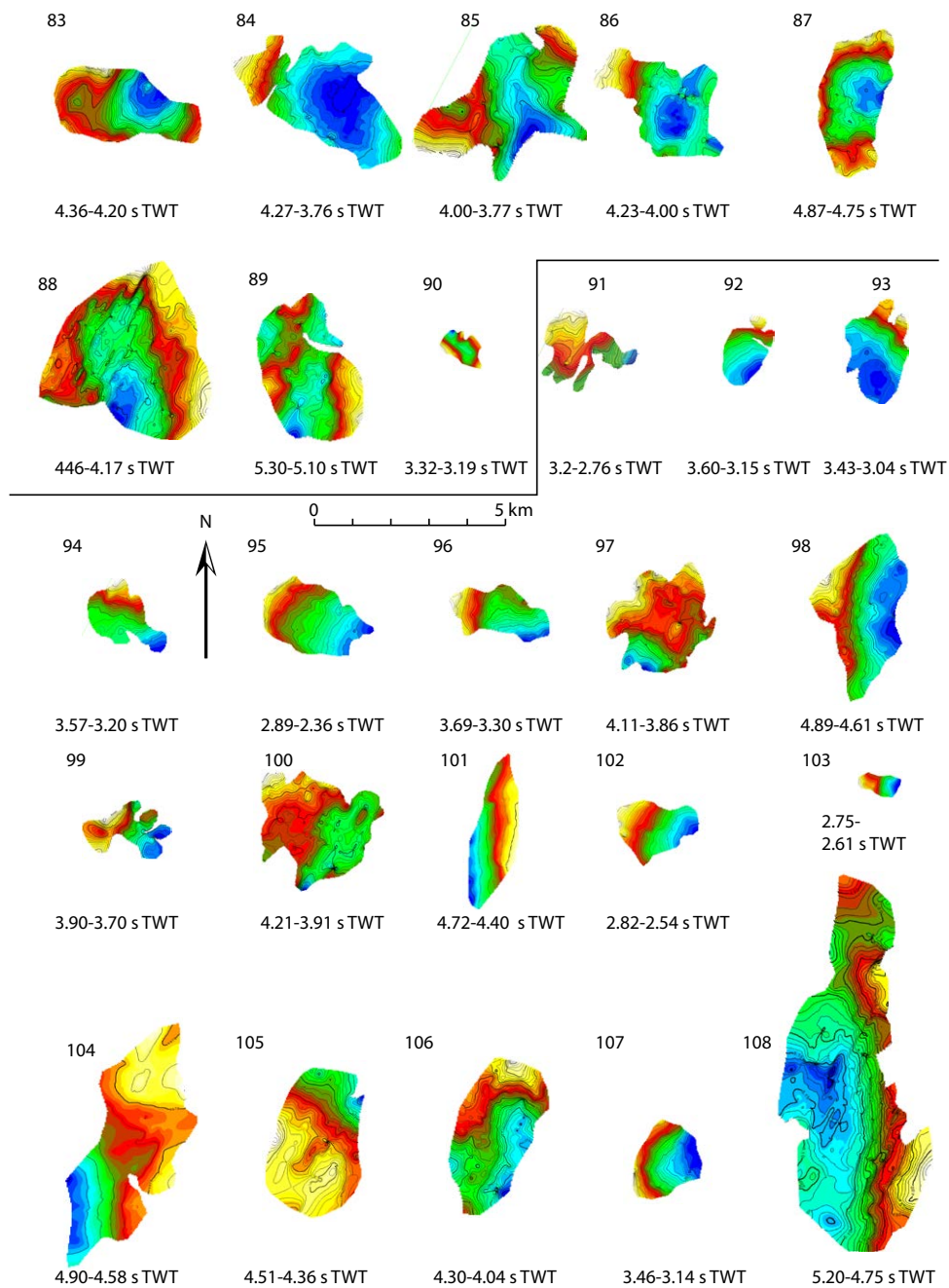
Area 6

Figure A2.5. Thumbnail maps of sills from Area 7 (83–108) (see Fig. 10 for location of areas). Colors have different time-depth ranges in each map, blue—relatively deep, yellow—relatively shallow. Absolute time-depth ranges in seconds two way travel time (s TWT) are provided below each map. The single line separates saucer-shaped sills (83–90) from other morphologies (91–108).

REFERENCES CITED

Acocella, V., Cifelli, F., and Funiciello, R., 2001, The control of overburden thickness on resurgent domes: Insights from analogue models: Journal of Volcanology and Geothermal Research, v. 111, p. 137–153, https://doi.org/10.1016/S0377-0273(01)00224-4.

Acocella, V., Korme, T., Salvini, F., and Funiciello, R., 2003, Elliptic calderas in the Ethiopian Rift: Control of preexisting structures: Journal of Volcanology and Geothermal Research, v. 119, p. 189–203, https://doi.org/10.1016/S0377-0273(02)00342-6.

Aizawa, K., Koyama, T., Hase, H., Uyeshima, M., Kanda, W., Utsugi, M., Ryokei, Y., Yusuke, Y., Takeshi, H., Kenichi, Y., Shintaro, K., Watanabe, A., Koji, M., and Yasuo, O., 2014, Three-dimensional resistivity structure and magma plumbing system of the Kirishima Volcanoes as inferred from broadband magnetotelluric data: Journal of Geophysical Research. Solid Earth, v. 119, p. 198–215, https://doi.org/10.1002/2013JB010682.

Amelung, F., and Day, S., 2002, InSAR observations of the 1995 Fogo, Cape Verde, eruption: Implications for the effects of collapse events upon island volcanoes: Geophysical Research Letters, v. 29, https://doi.org/10.1029/2001GL013760.

Andersen, T., Tronnes, R.G., Nilsen, O., and Larsen, A.O., 2008, Alkaline rocks of the Oslo Rift, SE Norway: A field trip with emphasis on felsic to intermediate intrusive rocks and their associated mineralizations: Oslo, Norway, University of Oslo, Department of Geosciences, August 1–5, Eurogranites 2008/IGCP 510 field trip 2008, 54 p.

Anderson, E.M., 1939, The dynamics of sheet intrusion: Proceedings of the Royal Society of Edinburgh, v. 58, p. 242–251, https://doi.org/10.1017/S0370164600011159.

Anderson, E.M., 1951, The Dynamics of Faulting and Dike Formation with Applications to Britain (second edition): Edinburgh, Scotland, Oliver and Boyd, 206 p.

Atherton, M.P., 1993, Granite magmatism: Journal of the Geological Society of London, v. 150, p. 1009–1023.

Bailey, E.B., Clough, C.T., Wright, W.B., Richey, J.E., and Wilson, G.V., 1924, Tertiary and post-Tertiary geology of Mull, Loch Aline, and Oban: Memoirs of the Geological Survey of Scotland, Sheet 44, 445 p.

Baker, S., and Amelung, F., 2012, Top-down inflation and deflation at the summit of Kilauea Volcano, Hawaii observed with InSAR: Journal of Geophysical Research. Solid Earth, v. 117, B10406, https://doi.org/10.1029/2011JB009123.

Barnett, Z., and Gudmunsson, A., 2014, Numerical modeling of dikes deflected into sills to form a magma chamber: Journal of Volcanology and Geothermal Research, v. 281, p. 1–11, https://doi.org/10.1016/j.jvolgeores.2014.05.018.

Barr, S.M., and Cooper, M.A., 2013, Late Cenozoic basalt and gabbro in the subsurface of the Phetchabun Basin, Thailand: Implications for the Southeast Asian Volcanic Province: Journal of Asian Earth Sciences, v. 76, p. 169–184, https://doi.org/10.1016/j.jseaes.2013.01.013.

Belachew, M., Ebinger, C., and Cote, D., 2013, Source mechanisms of dike-induced earthquakes in the Dabbahu-Manda Hararo rift segment in Afar, Ethiopia: Implications for faulting above dikes: Geophysical Journal International, v. 192, p. 907–917, https://doi.org/10.1093/gji/ggs076.

Bell, B., and Butcher, H., 2002, On the emplacement of sill complexes: Evidence from the Faroe-Shetland Basin, in Jolley, D.W., and Bell, B.R., eds., The North Atlantic Igneous Province: Stratigraphy, Tectonic, Volcanic and Magmatic Processes: Geological Society of London Special Publication 197, p. 307–329, https://doi.org/10.1144/GSL.SP.2002.197.01.12.

Benito-Saz, M.A., Parks, M.M., Sigmundsson, F., Hooper, A., and Garcia-Cañada, L., 2017, Repeated magmatic intrusions at El Hierro Island following the 2011–2012 submarine eruption: Journal of Volcanology and Geothermal Research, v. 344, p. 79–91, https://doi.org/10.1016/j.jvolgeores.2017.01.020.

Bergman, S.C., Talbot, J.P., and Thompson, P.R., 1992, The Kora Miocene submarine Andesite stratovolcano hydrocarbon reservoir, Northern Taranaki Basin, New Zealand, in Proceedings of the 1991 New Zealand Oil Exploration Conference: Wellington, New Zealand Ministry of Commerce, v. 1, p. 178–206.

Beutel, E., van Wijk, J., Ebinger, C., Keir, D., and Agostini, A., 2010, Formation and stability of magmatic segments in the Main Ethiopian and Afar rifts: Earth and Planetary Science Letters, v. 293, p. 225–235, https://doi.org/10.1016/j.epsl.2010.02.006.

Bischoff, A.P., Nicol, A., and Beggs, M., 2017, Stratigraphy of architectural elements in a buried volcanic system and implications for hydrocarbon exploration: Interpretation, v. 5, no. 3, p. 141–159, https://doi.org/10.1190/INT-2016-0201.1.

Bonaccorso, A., and Davis, P.M., 1999, Models of ground deformation from vertical volcanic conduits with application to eruptions of Mount St. Helens and Mount Etna: Journal of Geophysical Research, v. 104, p. 10531–10542, https://doi.org/10.1029/1999JB900054.

Brown, D.J., and Bell, B.R., 2006, Intrusion-induced uplift and mass wasting of the Paleogene volcanic landscape of Ardnamurchan, NW Scotland: Journal of the Geological Society, v. 163, p. 29–36, https://doi.org/10.1144/0016-764905-016.

Burchardt, S., Troll, V.R., Mathieu, L., Emeleus, H.C., and Donalds, C.H., 2013, Ardnamurchan 3D cone-sheet architecture explained by a single elongate magma chamber: Scientific Reports, v. 3, https://doi.org/10.1038/srep02891.

Cartwright, J., and Hansen, D.M., 2006, Magma transport through the crust via interconnected sill complexes: Geology, v. 34, p. 929–932, https://doi.org/10.1130/G22758A.1.

Cashman, K.V., and Giordano, G., 2014, Calderas and magma reservoirs: Journal of Volcanology and Geothermal Research, v. 288, p. 28–45, https://doi.org/10.1016/j.jvolgeores.2014.09.007.

Cassidy, J., and Locke, C.A., 2010, The Auckland volcanic field, New Zealand: Geophysical evidence for structural and spatio-temporal relationships: Journal of Volcanology and Geothermal Research, v. 195, p. 127–137, https://doi.org/10.1016/j.jvolgeores.2010.06.016.

Cervelli, P., and Miklius, A., 2003, The shallow magmatic system of Kilauea Volcano, in Heliker, C., Swanson, D.A., and Takahashi, T.J., eds., The Pu'u 'Ö'ö-Küpaianaha Eruption of Kilauea Volcano, Hawai'i: The First 20 Years: U.S. Geological Survey Professional Paper 1676, p. 149–163.

Chiarabba, C., De Gori, P., and Patanè, D., 2004, The Mt. Etna plumbing system: The contribution of seismic tomography, in Bonaccorso, A., Calvari, S., Coltelli, M., Del Negro, C., and Falsaperla, S., eds., Mount Etna: Volcano Laboratory: Washington, D.C., USA, American Geophysical Union, Geophysical Monograph Series 143, p. 191–204.

Delaney, J.R., Kelley, D.S., Lilley, M.D., Butterfield, D.A., Baross, J.A., Wilcock, W.S.D., Embley, R.W., and Summit, M., 1998, The quantum event of oceanic crustal accretion: Impacts of diking at mid-ocean ridges: Science, v. 281, p. 222–230, https://doi.org/10.1126/science.281.5374.222.

Dugda, M.T., Nyblade, A.A., Julia, J., Langston, C.A., Ammon, C.J., and Simiyu, S., 2005, Crustal structure in Ethiopia and Kenya from receiver function analysis: Implications for rift development in eastern Africa: Journal of Geophysical Research. Solid Earth, v. 110, https://doi.org/10.1029/2004JB003065.

Dumont, S., Klinger, Y., Socquet, A., Soubre, C., and Jacques, E., 2017, Magma influence on propagation of normal faults: Evidence from cumulative slip profiles along Dabbahu-Manda-Hararo rift segment (Afar, Ethiopia): Journal of Structural Geology, v. 95, p. 48–59, https://doi.org/10.1016/j.jsg.2016.12.008.

Ebinger, C., Ayele, A., Keir, D., Rowland, J., Yirgu, G., Wright, T., Belawchew, M., and Hamling, I., 2010, Length and Timescales of Rift Faulting and Magma Intrusion: The Afar Rifting Cycle from 2005 to Present: Annual Review of Earth and Planetary Sciences, v. 38, p. 439–466, https://doi.org/10.1146/annurev-earth-040809-152333.

Eichelberger, J.C., Izbekov, P.E. and Browne, B.L., 2006, Bulk chemical trends at arc volcanoes are not liquid lines of descent: Lithos, v. 87, p. 135–154.

Ellis, M., and King, G., 1991, Structural control of flank volcanism in continental rifts: Science, v. 254, p. 839–842, https://doi.org/10.1126/science.254.5033.839.

Feigl, K.L., Le Mevel, H., Tabrez Ali, S., Cordova, L., Andersen, N.L., DeMets, C., and Singer, B.S., 2013, Rapid uplift in Laguna del Maule volcanic field of the Andean southern volcanic zone (Chile), 2007–2012: Geophysical Journal International, v. 196, p. 885–901, https://doi.org/10.1093/gji/ggt438.

Fialko, Y.A., and Rubin, A.M., 1998, Thermodynamics of lateral dike propagation, implications for crustal accretion at slow spreading mid-ocean ridges: Journal of Geophysical Research, v. 103, p. 2501–2514, https://doi.org/10.1029/97JB03105.

Galerne, C.Y., Galland, O., Neumann, E.-R., and Planke, S., 2011, 3D relationships between sills and their feeders: Evidence from the Golden Valley Sill Complex (Karoo Basin) and experimental modeling: Journal of Volcanology and Geothermal Research, v. 202, p. 189–199, https://doi.org/10.1016/j.jvolgeores.2011.02.006.

Galland, O., 2012, Experimental modeling of ground deformation associated with shallow magma intrusions: Earth and Planetary Science Letters, v. 317, p. 145–156, https://doi.org/10.1016/j.epsl.2011.10.017.

Galland, O., and Scheibert, J., 2013, Analytical model of surface uplift about axisymmetric flat-lying magma intrusions: Implications for sill emplacement and geodesy: Journal of Volcanology and Geothermal Research, v. 253, p. 114–130, https://doi.org/10.1016/j.jvolgeores.2012.12.006.

Giba, M., Walsh, J.J., and Nicol, A., 2009, Relationship between normal faulting and tectonic activity in the Taranaki backarc basin, New Zealand: Vienna, Austria, 19–24 April, European Geosciences Union General Assembly.

Giba, M., Nicol, A., and Walsh, J.J., 2010, Evolution of faulting and volcanism in a back-arc basin and its implications for subduction processes: Tectonics, v. 29, https://doi.org/10.1029/2009TC002634.

Giba, M., Walsh, J.J., Nicol, A., Mouslopoulou, V., and Seebeck, H., 2013, Investigation of the spatio-temporal relationship between normal faulting and arc volcanism on million-year timescales: Journal of the Geological Society, v. 170, p. 951–962, https://doi.org/10.1144/jgs2012-121.

González, P.J., Samsonov, S.V., Pepe, S., Tiampo, K.F., Tizzani, P., Casu, F., Fernandez, J., Camacho, A.G., and Sansosti, E., 2013, Magma storage and migration associated with the 2011–2012 El Hierro eruption: Implications for crustal magmatic systems at oceanic island volcanoes: Journal of Geophysical Research. Solid Earth, v. 118, p. 4361–4377, https://doi.org/10.1002/jgrb.50289.

Hald, N., Noe-Nygaard, A., and Pedersen, A.K., 1971, The Króksfjördur central volcano in North-West Iceland: Acta Naturalia Islandica, v. 2, no. 10, 29 p.

Hamling, I.J., Hreinsdóttir, S., and Fournier, N., 2015, The ups and downs of the TVZ: Geodetic observations of deformation around the Taupo Volcanic Zone, New Zealand: Journal of Geophysical Research. Solid Earth, v. 120, p. 4667–4679, https://doi.org/10.1002/2015JB012125.

Hansen, D.M., and Cartwright, J., 2006, The three-dimensional geometry and growth of forced folds above saucer-shaped igneous sills: Journal of Structural Geology, v. 28, p. 1520–1535, https://doi.org/10.1016/j.jsg.2006.04.004.

Hansen, J., 2015, A numerical approach to sill emplacement in isotropic media: Do saucer-shaped sills represent 'natural' intrusive tendencies in the shallow crust?: Tectonophysics, v. 664, p. 125–138, https://doi.org/10.1016/j.tecto.2015.09.006.

Hjartardóttir, A.R., Einarsson, P., Bramham, E., and Wright, T.J., 2012, The Krafla fissure swarm, Iceland, and its formation by rifting events: Bulletin of Volcanology, v. 74, p. 2139–2153, https://doi.org/10.1007/s00445-012-0659-0.

Infante-Paez, L., and Marfurt, K.J., 2017, Seismic expression and geomorphology of igneous bodies: A Taranaki Basin, New Zealand, case study: Interpretation, v. 5, https://doi.org/10.1190/INT-2016-0244.1.

Ishizuka, O., Geshi, N., Itoh, J., Kawanabe, Y., and Tuzino, T., 2008, The magmatic plumbing of the submarine Hachijo NW volcanic chain, Hachijojima, Japan: Long-distance magma transport?: Journal of Geophysical Research. Solid Earth, v. 113, https://doi.org/10.1029/2007JB005325.

Jackson, C.A.-L., Schofield, N., and Golenkov, B., 2013, Geometry and controls on the development of igneous sill-related forced folds: A 2-D seismic reflection case study from offshore southern Australia: Geological Society of America Bulletin, v. 125, p. 1874–1890, https://doi.org/10.1130/B30833.1.

Jaxybulatov, K., Shapiro, N.M., Koulakov, I., Mordret, A., Landes, M., and Sens-Schonfelder, C., 2014, A large magmatic sill complex beneath the Toba caldera: Science, v. 346, p. 617–619, https://doi.org/10.1126/science.1258582.

Kavanagh, J.L., Menand, T., and Sparks, R.S.J., 2006, An experimental investigation of sill formation and propagation in layered elastic media: Earth and Planetary Science Letters, v. 245, p. 799–813, https://doi.org/10.1016/j.epsl.2006.03.025.

King, P.R., and Thrasher, G.P., 1996, Cretaceous-Cenozoic Geology and Petroleum Systems of the Taranaki Basin: Lower Hutt, New Zealand, Institute of Geological and Nuclear Sciences Monograph, v. 13, 244 p.

Korme, T., Acocella, V., and Abebe, B., 2003, The role of preexisting structures in the origin, propagation and architecture of faults in the Main Ethiopian Rift: Gondwana Research, v. 7, p. 467–479, https://doi.org/10.1016/S1342-937X(05)70798-X.

Koulakov, I., Kasatkina, E., Shapiro, N.M., Jaupart, C., Vasil, A., El Khrepy, S., Al-Arifi, N., and Smirnov, S., 2016, The feeder system of the Toba supervolcano from the slab to the shallow reservoir: Nature Communications, v. 7, https://doi.org/10.1038/ncomms12228.

Kroeger, K.F., Funnell, R.H., Nicol, A., Fohrmann, M., Bland, K.J., and King, P.R., 2013, 3D crustal-scale heat-flow regimes at a developing active margin (Taranaki Basin, New Zealand): Tectonophysics, v. 591, p. 175–193, https://doi.org/10.1016/j.tecto.2012.04.005.

Kühn, D., and Dahm, T., 2008, Numerical modeling of dike interaction and its influence on oceanic crust formation: Tectonophysics, v. 447, p. 53–65, https://doi.org/10.1016/j.tecto.2006.09.018.

Le Bas, M.J., 1971, Cone-sheets as a mechanism of uplift: Geological Magazine, v. 108, p. 373–376, https://doi.org/10.1017/S0016756800056399.

Le Corvec, N., Sporli, K.B., Rowland, J., and Lindsay, J., 2013, Spatial distribution and alignments of volcanic centers: Clues to the formation of monogenetic volcanic fields: Earth-Science Reviews, v. 124, p. 96–114, https://doi.org/10.1016/j.earscirev.2013.05.005.

Lorenz, V., 1975, Formation of phreatomagmatic maar-diatreme volcanoes and its relevance to kimberlite diatremes, in Ahrens, L.H., Dawson, J.B., Duncan, A.R., and Erlank, A.J., eds., Physics and Chemistry of the Earth: Oxford, UK, Pergamon Press, v. 9, p. 17–27, https://doi.org/10.1016/B978-0-08-018017-5.50006-7.

Magee, C., Hunt-Stewart, E., and Jackson, C.A.-L., 2013a, Volcano growth mechanisms and the role of sub-volcanic intrusions. Insights from 2D seismic reflection data: Earth and Planetary Science Letters, v. 373, p. 41–53, https://doi.org/10.1016/j.epsl.2013.04.041.

Magee, C., Briggs, F., and Jackson, C.A.-L., 2013b, Lithological controls on igneous intrusion-induced ground deformation: Journal of the Geological Society, v. 170, p. 853–856, https://doi.org/10.1144/jgs2013-029.

Magee, C., Maharaj, S.M., Wrona, T., and Jackson, C.A.-L., 2015, Controls on the expression of igneous intrusions in seismic reflection data: Geosphere, v. 11, p. 1024–1041, https://doi.org/10.1130/GES01150.1.

Magee, C., Muirhead, J.D., Karvelas, A., Holford, S.P., Jackson, C.A.L., Bastow, I.D., Schofield, N., Stevenson, C.T.E., McLean, C., McCarthy, W., and Shtukert, O., 2016, Lateral magma flow in mafic sill complexes: Geosphere, v. 12, p. 809–841, https://doi.org/10.1130/GES01256.1.

Magee, C., Bastow, I.D., van Wyk de Vries, B., Jackson, C.A.-L., Hetherington, R., Hagos, M., and Hoggett, M., 2017, Structure and dynamics of surface uplift induced by incremental sill emplacement: Geology, v. 45, p. 431–434, https://doi.org/10.1130/G38839.1.

Marsh, B., 2004, A Magmatic Mush Column Rosetta Stone: The McMurdo Dry Valleys of Antarctica: Eos (Transactions, American Geophysical Union), v. 85, p. 497–508.

Marsh, J.S., Hooper, P.R., Rehacek, J., and Duncan, A.R., 1997, Stratigraphy and age of Karoo basalts of Lesotho and implications for correlations within the Karoo Igneous Province, in Mahoney, J.J., and Coffin, M.F., eds., Large Igneous Provinces: Continental, Oceanic, and Planetary Flood Volcanism: Washington, D.C., USA, American Geophysical Union, Geophysical Monograph Series, v. 100, p. 247–272, https://doi.org/10.1029/GM100p0247.

Mazzarini, F., Keir, D., and Isola, I., 2013, Spatial relationship between earthquakes and volcanic vents in the central-northern Main Ethiopian Rift: Journal of Volcanology and Geothermal Research, v. 262, p. 123–133, https://doi.org/10.1016/j.jvolgeores.2013.05.007.

Medynski, S., Pik, R., Burnard, P., Dumont, S., Grandin, R., Williams, A., Plard, P.-H., Schimmelpfenning, I., Vye-Brown, C., France, L., Ayalew, D., Benedetti, L., Yirgu, G., Aster team, 2016, Magmatic cycles pace tectonic and morphological expression of rifting (Afar depression, Ethiopia): Earth and Planetary Science Letters, v. 446, p. 77–88, https://doi.org/10.1016/j.epsl.2016.04.014.

Mériaux, C., and Lister, J.R., 2002, Calculation of dike trajectories from volcanic centers: Journal of Geophysical Research, v. 107, https://doi.org/10.1029/2001JB000436.

Mohr, P., 1987, Structural style of continental rifting in Ethiopia: Reverse decollements: Eos (Transactions, American Geophysical Union), v. 68, p. 721–730.

Morley, C.K., 1994, Interaction of deep and shallow processes in the evolution of the Kenya rift: Tectonophysics, v. 236, p. 81–91, https://doi.org/10.1016/0040-1951(94)90170-8.

Morley, C.K., Bosworth, W., Day, R.A., Lauck, R., Bosher, R., Stone, D.M., Wigger, S.T., Wescott, W.A., Haun, D., and Bassett, N., 1999, Chapter 4: Geology and Geophysics of the Anza Graben, in Morley, C.K., ed., Geoscience of Rift Systems-Evolution of East Africa: Tulsa, Oklahoma, USA, The American Association of Petroleum Geologists Studies in Geology, v. 44, p. 67–90.

Morley, C.K., von Hagke, C., Hansberry, R., Collins, A., Kanitpanyacharoen, W., and King, R., 2018, Review of major shale-dominated detachment and thrust characteristics in the diagenetic zone: Part II, rock mechanics and microscopic scale: Earth-Science Reviews, v. 176, p. 19–50, https://doi.org/10.1016/j.earscirev.2017.09.015.

Muirhead, J.D., Airoldi, G., Rowland, J.V., and White, J.D., 2012, Interconnected sills and inclined sheet intrusions control shallow magma transport in the Ferrar large igneous province, Antarctica: Geological Society of America Bulletin, v. 124, p. 162–180, https://doi.org/10.1130/B30455.1.

Muirhead, J.D., Kattenhorn, S.A., Lee, H., Mana, S., Turrin, B.D., Fischer, T.P., Kinji, G., Dindi, F., and Stamps, D.S., 2016, Evolution of upper crustal faulting assisted by magmatic volatile release during early-stage continental rift development in the East African Rift: Geosphere, v. 12, p. 1670–1700, https://doi.org/10.1130/GES01375.1.

Muller, O.H., and Pollard, D.D., 1977, The stress state near Spanish Peaks, Colorado, determined from a dike pattern: Pure and Applied Geophysics, v. 115, p. 69–86, https://doi.org/10.1007/BF01637098.

Naviset, S., Morley, C.K., Naghadeh, D.H., and Ghosh, J., 2017, Sill emplacement during rifting and inversion from three dimensional seismic and well data, Phitsanulok Basin, Thailand: Geosphere, v. 13, p. 2017–2040, https://doi.org/10.1130/GES01466.1.

Odé, H., 1957, Mechanical analysis of the dike pattern of the Spanish Peaks area, Colorado: Geological Society of America Bulletin, v. 68, p. 567–576, https://doi.org/10.1130/0016-7606 (1957)68[567:MAOTDP]2.0.CO;2.

Perkins, J.P., Ward, K.M., de Silva, S.L., Zandt, G., Beck, S.L., and Finnegan, N.J., 2016, Surface uplift in the Central Andes driven by growth of the Altiplano Puna Magma Body: Nature Communications, v. 7, https://doi.org/10.1038/ncomms13185.

Petroleum Report Series, 1984, Completion Report, Ariki-1 well, PPL 38048: Wellington, New Zealand, Ministry of Economic Development, PR 1038, 179 p.

Petroleum Report Series, 1985, Final well report, Kora-4, PPL 38447: Wellington, New Zealand, Ministry of Economic Development, PR 1443, 268 p.

Petroleum Report Series, 1988, Final well report, Kora-1, Kora 1A, PPL 39448: Wellington, New Zealand, Ministry of Economic Development, PR 1374, 885 p.

Phillips, W.J., 1974, The dynamic emplacement of cone sheets: Tectonophysics, v. 24, p. 69–84, https://doi.org/10.1016/0040-1951(74)90130-9.

Planke, S., Ramussen, T., Rey, S.S., and Myklebust, R., 2005, Seismic characteristics and distribution of volcanic intrusions and hydrothermal vent complexes in the Voring and More basins, in Dore, A.G., ed., Petroleum Geology: North-West Europe and Global Perspectives: Geological Society of London Petroleum Geology Conference Series, v. 6, p. 833–844, https://doi.org/10.1144/0060833.

Pollard, D.D., and Johnson, A.M., 1973, Mechanics of growth of some laccolithic intrusions in the Henry Mountains, Utah, II: Bending and failure of overburden layers and sill formation: Tectonophysics, v. 18, p. 311–354, https://doi.org/10.1016/0040-1951(73)90051-6.

Pollard, D.D., Muller, O.H., and Dockstader, D.R., 1975, The form and growth of fingered sheet intrusions: Geological Society of America Bulletin, v. 86, p. 351–363, https://doi.org/10.1130/0016-7606(1975)86<351:TFAGOF>2.0.CO;2.

Rateau, R., Schofield, N., and Smith, M., 2014, The potential role of igneous intrusions on hydrocarbon migration West of Shetland: Petroleum Geoscience, v. 19, p. 259–272, https://doi.org/10.1144/petgeo2012-035.

Rubin, A.M., 1995, Propagation of magma-filled cracks: Annual Review of Earth and Planetary Sciences, v. 23, p. 287–336, https://doi.org/10.1146/annurev.ea.23.050195.001443.

Rubin, A.M., and Pollard, D.D., 1988, Dike-induced faulting in rift-zones in Iceland and Afar: Geology, v. 16, p. 413–417, https://doi.org/10.1130/0091-7613(1988)016<0413:DIFIRZ>2.3.CO;2.

Ryan, M.P., 1988, The mechanics and three-dimensional structure of active magmatic systems: Kilauea Volcano, Hawaii: Journal of Geophysical Research. Solid Earth, v. 93, p. 4213–4248, https://doi.org/10.1029/JB093iB05p04213.

Schofield, N., Brown, D.J., Magee, C., and Stevenson, C.T., 2012a, Sill morphology and comparison of brittle and non-brittle emplacement mechanisms: Journal of the Geological Society, v. 169, p. 127–141, https://doi.org/10.1144/0016-76492011-078.

Schofield, N., Heaton, L., Holford, S., Archer, S., Jackson, C., and Jolley, D.W., 2012b, Seismic imaging of 'Broken-Bridges': Linking seismic to outcrop-scale investigations of intrusive magma lobes: Journal of the Geological Society, v. 169, p. 421–426, https://doi.org/10.1144/0016-76492011-150.

Schofield, N., Holford, S., Millett, J., Brown, D., Jolley, D., Passey, S., Muirhead, D., Grove, C., Magee, C., Murray, J., Hole, M., Jackson, C., and Stevenson, C., 2016, Regional magma plumbing and emplacement mechanisms of the Faero-Shetland Sill Complex: Implications for magma transport and petroleum systems within sedimentary basins: Basin Research, v. 29, p. 41–63, https://doi.org/10.1111/bre.12164.

Seebeck, H.C., Nicol, A., Villamor, P., Ristau, J., and Pettinga, J., 2014, Structure and kinematics of the Taupo Rift, New Zealand: Tectonics, v. 33, p. 1178–1199, https://doi.org/10.1002/2014TC003569.

Sheridan, M.F., and Wohletz, K.H., 1981, Hydrovolcanic explosions, the systematics of water-pyroclast equilibration: Science, v. 212, no. 17, p. 433–469.

Sigmundsson, F., Hreinsdóttir, S., Hooper, A., Arnadottir, T., Pedersen, R., Roberts, M.J., Oskarsson, N., Auriac, A., Decriem, J., Einarsson, P., Geirsson, H., Hensch, M., Ofeigsson, B.G., Sturkell, E., Svienbjornsson, H., and Feigl, K.L., 2010, Intrusion triggering of the 2010 Eyjafjallajökull explosive eruption: Nature, v. 468, p. 426–430, https://doi.org/10.1038/nature09558.

Smallwood, J.R., and Maresh, J., 2002, The properties, morphology and distribution of igneous sills: Modeling, borehole data and 3D seismic from the Faroe-Shetland area, in Jolley, D.W., and Bell, B.R., eds., The North Atlantic Igneous Province: Stratigraphy, Tectonic, Volcanic and Magmatic Processes: Geological Society of London Special Publication 197, p. 271–306, https://doi.org/10.1144/GSL.SP.2002.197.01.11.

Smith, R.P., 1987, Dike emplacement at Spanish Peaks, Colorado, in Halls, H.C., and Fahrig, W.F., eds., Mafic Dike Swarms: Geological Association of Canada Special Publication, v. 34, p. 47–54.

Strogen, D.C., Seebeck, H., Nicol, A., and King, P.R., 2017, Two-phase Cretaceous-Paleocene rifting in the Taranaki Basin region, New Zealand; Implications for Gondwana break-up: Journal of the Geological Society, https://doi.org/10.1144/jgs2016-160.

Suggate, R.P., Stevens, G.R., and Te Punga, M.T., 1978, The Geology of New Zealand: Wellington, New Zealand, Government Printer, 2 vols., 820 p.

Thomson, K., 2005, Volcanic features of the North Rockall Trough: Application of visualization techniques on 3D seismic reflection data: Bulletin of Volcanology, v. 67, p. 116–128, https://doi.org/10.1007/s00445-004-0363-9.

Thomson, K., and Hutton, D., 2004, Geometry and growth of sill complexes: Insights using 3D seismic from the North Rockall Trough: Bulletin of Volcanology, v. 66, p. 364–375, https://doi.org/10.1007/s00445-003-0320-z.

Tibaldi, A., 2015, Structure of volcano plumbing systems: A review of multi-parametric effects: Journal of Volcanology and Geothermal Research, v. 298, p. 85–135, https://doi.org/10.1016/j.jvolgeores.2015.03.023.

Tibaldi, A., and Bonali, F.L., 2017, Intra-arc and back-arc volcano-tectonics: Magma pathways at Holocene Alaska-Aleutian volcanoes: Earth-Science Reviews, v. 167, p. 1–26, https://doi.org/10.1016/j.earscirev.2017.02.004.

Tibaldi, A., Pasquare, F.A., and Rust, D., 2011, New insights into the cone sheet structure of the Cuillin Complex, Isle of Skye, Scotland: Journal of the Geological Society, v. 168, p. 689–704, https://doi.org/10.1144/0016-76492009-175.

Tibaldi, A., Bonali, F.L., and Corazzato, C., 2017, Structural control on volcanoes and magma paths from local- to orogeny-scale: The central Andes case: Tectonophysics, v. 699, p. 16–41, https://doi.org/10.1016/j.tecto.2017.01.005.

Valentine, G.A., and Krogh, K.E.C., 2006, Emplacement of shallow dikes and sills beneath a small basaltic volcanic center–The role of preexisting structure (Paiute Ridge, southern Nevada, USA): Earth and Planetary Science Letters, v. 246, p. 217–230, https://doi.org/10.1016/j.epsl.2006.04.031.

van Wyk de Vries, B., Marquez, A., Herra, R., Bruna, J.G., Llanes, P., and Delcamp, A., 2014, Craters of elevation revisited: Forced-folds, bulging and uplift of volcanoes: Bulletin of Volcanology, v. 76, p. 1–20, https://doi.org/10.1007/s00445-014-0875-x.

Walker, G.P.L., 1958, Geology of the Reydarfjördur area, eastern Iceland: Quarterly Journal of the Geological Society, v. 114, p. 367–391, https://doi.org/10.1144/gsjgs.114.1.0367.

Wohletz, K.H., 1986, Explosive magma-water interactions: Thermodynamics, explosion mechanisms, and field studies: Bulletin Volcanologica, v. 48, p. 245–264, https://doi.org/10.1007/BF01081754.